A NON-RESONANT KINETIC ENERGY HARVESTER FOR BIO-IMPLANTABLE APPLICATIONS

by

Hacene CHIKH BAELHADJ

September 2018

a thesis submitted in conformity with the requirements for the degree of Master of Science

Graduate School of Sciences and Engineering

Antalya Bilim University

electrical and computer engineering

A Non-resonant Kinetic Energy Harvester for Bio-implantable Applications

by Hacene CHIKH BAELHADJ

September 2018

As members of the thesis examination committee, we certify that we have read this thesis and that in our opinion it is satisfactory in scope and in quality, as a thesis for the degree of Master of Science.

Asst. Prof. Dr. Mustafa İlker BEYAZ (Advisor)
Department of Electrical and Electronics Engineering, Antalya Bilim University

Asst. Prof. Dr. Yusuf Öztürk
Department of Electrical and Electronics Engineering, Antalya Bilim University

Asst. Prof. Dr. Deniz Kaya
Department of Physics, Akdeniz University

ABSTRACT

A NON-RESONANT KINETIC ENERGY HARVESTER FOR BIO-IMPLANTABLE APPLICATIONS

Hacene CHIKH BAELHADJ
M.S. in Electrical and Computer Engineering
Advisor: Asst. Prof. Dr. Mustafa İlker BEYAZ
September 2018

Bio-implantable devices are attracting much attention, as they provide effective solutions for monitoring and treatment of diverse health problems. Examples for already-developed devices include pressure sensors, pacemakers, muscle stimulators, and glucose sensors that can control and monitor diseases ranging from heart-related disorders to diabetes. Batteries that are currently used in bio-implants have limited energy storage capacities, requiring frequent battery replacements and thus limiting the functionality of such medical devices. In this respect, energy harvesting from human body movements offers a promising alternative as on-board power for implantable medical devices. The aim of this project is to develop an implantable power generator capable of converting the kinetic energy existing in body movements into electricity at any part of the body.

The generator is designed to be bio-compatible with a volume less than 1 cm^3 for implantability. Energy is generated from daily activities such as walking, running, and twisting through the utilization of electromagnetic induction principles. An important aspect of the design is the non-resonant device nature. Accordingly, it is possible to generate energy from a variety of body activities at different frequencies. Simulations were performed on COMSOL software for design optimization. The device was manufactured using a combination of micro-fabrication and CNC technologies. Initial testing on a linear shaker platform resulted in an open circuit voltage and output power of 6.25 mV and 0.33 µW, respectively. The device was integrated on a wristband to test real-life performance. The voltage and power during normal walking were measured to be 4.4 mV and 0.14 µW. These values increased to 6.85 mV

and 0.2 µW when running. Several improvements in the design and testing scheme were proposed to take these values at even higher levels. The findings and results reported here are important steps forward to develop electronic self-sufficient bio-implants that do not need battery replacements and can generate their own energy autonomously in the body.

Keywords: Micro-generator, non-resonant generator, in-vivo energy generation, energy harvesting, power MEMS.

ÖZET

BİYOİMPLANT UYGULAMALARI İÇİN REZONANT OLMAYAN VE ENERJİ HASADI YAPABİLİEN MİKROJENERATÖR

Hacene CHIKH BAELHADJ
Elektrik ve Bilgisayar Mühendisliği, Yüksek Lisans
Tez Danışmanı: Yrd. Doç. Dr. Mustafa İlker BEYAZ
Eylül 2018

Gün geçtikçe geliştirilmekte olan elektronik biyoimplantlar birçok sağlık sorununun izlenmesi ve tedavisinde etkin çözümler sunmaktadır. Örnek olarak basınç sensörleri, kalp pilleri, kas uyarıcıları ve glükoz sensörleri kalp rahatsızlıklarından diyabete kadar geniş bir yelpazedeki hastalıkların izlenmesi ve kontrolü için çare olabilecek niteliktedir. Bu aygıtları çalıştırmakta kullanılan piller, sınırlı enerji depolama yetenekleri nedeniyle sıklıkla değiştirilmeye ihtiyaç duymakta ve dolayısıyla bu aygıtların kullanımlarını sınırlandırmaktadırlar. Bu açıdan bakıldığında, vücut hareketlerinden enerji hasadı ile elektrik enerjisi üretmek, söz konusu aygıtların çalıştırılması noktasında alternatif bir çözüm sunmaktadır. Bu projenin amacı insanların normal aktiviteleri sırasındaki vücut hareketlerini vücut içerisindeki herhangi bir noktada elektrik enerjisine dönüştürebilen bir jeneratör geliştirmektir.

Jeneratör, vücut ortamına uyumlu olacak şekilde 1 cm^3'ten küçük ve biyouyumlu olarak tasarlanmıştır. Yürüme, koşma ve dönme gibi hareketlerin elektrik enerjisine dönüştürülmesi için elektromanyetik indüskiyon prensibi kullanılmıştır. Tasarımın önemli bir unsuru, rezonant olmayan bir yapının kullanılmasıdır. Bu nedenle farklı frekanstaki birçok hareketin elektriğe dönüştürülmesi mümkün olmuştur. Tasarım optimizasyonu için COMSOL programında simülasyonlar yapılmıştır. Jeneratör mikrofabrikasyon ve CNC teknolojileri ile üretilmiştir. Hareketli bir platform kullanılarak yapılan öncü testlerde 6.25 mV açık devre gerilimi ile 0.33 µW güce ulaşılmıştır. Aygıt, gerçek koşullardaki performansını ölçmek için bir bilekliğe entegre edilmiştir. Yürüme sırasında 4.4 mV açık devre voltajı ile 0.14 µW güç

değerleri ölçülmüştür. Bu değerlerin koşma aktivitesi sırasında 6.85 mV ile 0.2 µW'a çıktığı görülmüştür. Elde edilen değerlerin artırılması için aygıtın iyileştirilebilir yönleri tartışılmıştır. Bu çalışmada elde edilen sonuçlar, kendi kendine yetebilen ve pil değişimine ihtiyaç duymayan biyoimplantların geliştirilmesi için önayak niteliğindedir.

Anahtar sözcükler: Mikro-jeneratör, rezonant olmayan jeneratör, vücut içi enerji üretimi, enerji madenciliği, power MEMS.

Dedication

To my admired mother and father, without whom, I would not be in this place.

To my great brothers Kacem, Mohamed, Salah and Elhadj, for their encouragement.

To my beloved fiancée, for her inspiration.

To all of them, I would like to express my sincere thanks for their patience during the years I stayed far from them, without their assistance, this work would not have been realized.

Acknowledgements

I firstly thank my advisor Dr. Mustafa İlker BEYAZ for his guidance throughout my master studies. I would like to thank the jury members: Dr. Yusuf Öztürk and Dr. Deniz Kaya.

Special thanks to Dr. Vlad Badilita from the Institute of Micro-structures Technology (IMT), Karlsruhe Institute of Technology (KIT), Germany, for his collaboration in the project. I express my thanks to Shyamsundar Adhikari and Hossein Davoodi for their invaluable help they provided during fabrication at the IMT cleanroom. I thank Sahar Habibiabad for her assistance in fabrication at Bilkent University National Nanotechnology Research Center (UNAM), Ankara.

This work was supported by the Scientific and Technological Research Council of Turkey (TÜBİTAK) under grant number 114E435.

This work was carried out at UNAM and IMT cleanrooms.

Contents

List of Figures

List of Tables

Chapter 1

Introduction

1.1 Definition

Energy harvesting (EH), also referred to as energy scavenging, is defined as the process of collecting ambient energy from surrounding energy sources such as thermal gradients, RF radiation, solar energy, vibrations, and converting it into electrical energy. The collected energy is usually renewable as opposed to conventional sources including batteries, fossil and nuclear fuels.

1.2 History

The beginnings of energy harvesting date back to 1826, when Thomas Johann Seebeck noticed that a closed loop of two dissimilar metals with junctions at different temperatures gives an induced current, which is explained later and defined as Seebeck effect. As for electromagnetic induction, Faraday has

established and made his first generator in 1831. In 1839, Edmond Becquerel created the first photovoltaic cell then the concept was understood and defined later by quantum physics in the 1900s [1]. Pierre and Jacques Curie, two French brothers, were behind the discovery of piezoelectric phenomena in the early 1880, and then it was named after *piezein*, the Greek word for squeeze or press [2]. More details about these energy harvesting methods are in chapter 2.

1.3 Applications

Energy harvesting in the large scale is seen in wide range applications in the clean energy industry, waterwheels to produce hydroelectricity, wind energy in what is so-called wind farms, solar panels and geothermal power stations are common as well. Going down to smaller scale -to mention but not few- the regenerative braking in hybrid cars, where the lost energy in form of friction work is collected during braking and directed to charge the car battery [3].

Energy harvesting is known also in the scale of wearables and hand held electronics. One of the first patents in wearable device applications was filled in 1989 by Hayakawa, the patent was about an electrically operated self-winding watch that is indeed a small inertial energy harvester, and it is now a commercial product of Seiko Epson corporation. This pioneering Japanese company in self-powered watches has also proposed a thermally powered watch that collects thermal energy from the arm surface to fill up the watch battery, and a mechanically powered watch by the use of the moment of an unbalanced mass (see figure 1.1) [4–7].

There are many hybrid devices where photovoltaic cells are used to assist the battery available in markets such as Casio watches and calculators. Some other commercialized motion harvesters are described in [5]. Perpetuum and

Ferro Solutions offer devices with volume on the order of 13 cm^3 capable of generating up to 10.8 mW. Kinetron has a 28 mm^3 rotational micro-generator that generates an average power of 5 µW. As for piezoelectric devices, Advanced Ceramics produces micro-generators yielding 142 mW at a frequency of 35 Hz. MicroStrain Inc. has commercialized a piezoelectric harvester which produces about 200 µW at a resonant frequency of 60 Hz [6].

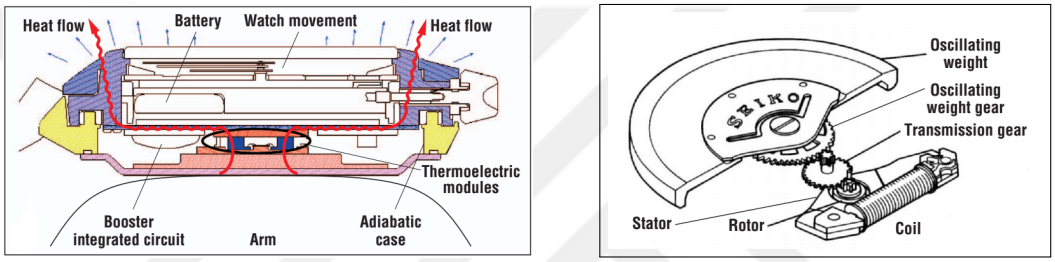

(a) (b)

Figure 1.1: Diagrams of Seiko self-powered watches by heat energy (a) and mechanical energy (b) [4].

The electronics industry generally follows Moore's law for decades, however, the only type of component that did not obey the law is power source. Although batteries are considered as critical elements in mobile electronics, they are the slowest trending in the field among other criteria such as CPU speed, RAM and hard drive capacity. For the last several years, there has been no significant improvement in the energy density of batteries. Even though new materials are revolutionizing the form factor of batteries, the inadequateness of battery density does not scale exponentially as seen in figure 1.2. Overcoming this problem requires investigating other solutions of energy sources [4]. Supplying power is a big challenge in devices like wireless sensors. For instance, marine electronics that are used remotely cannot be practically powered by batteries since they need a frequent replacement or replenishment [8]. The challenge becomes more complicated in case of some technologies

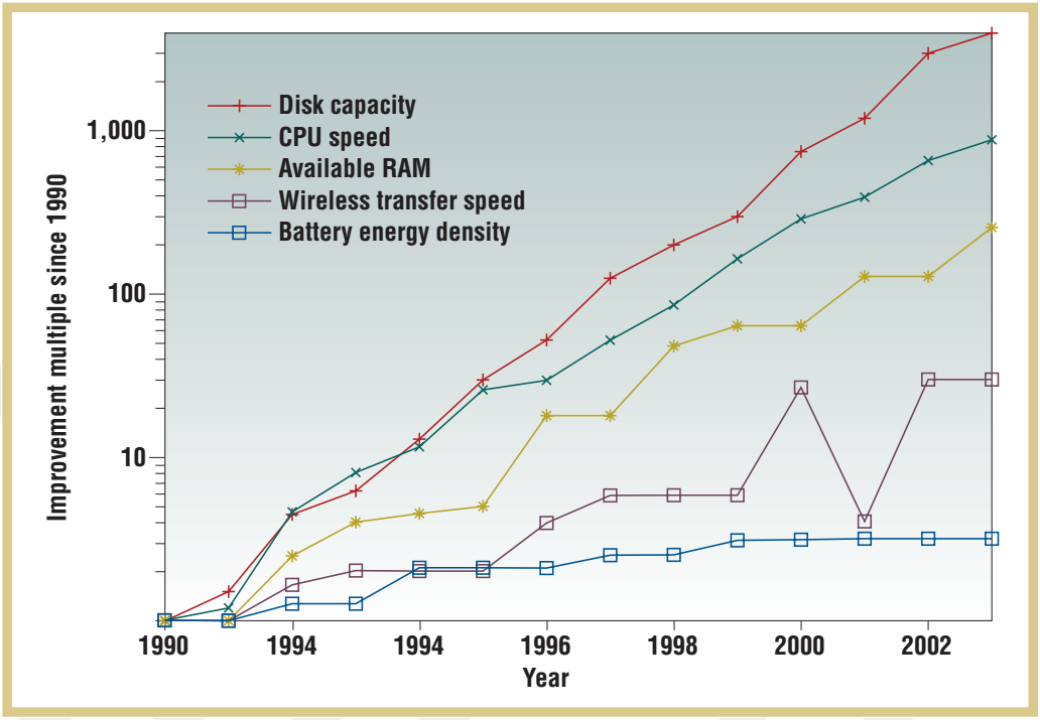

Figure 1.2: Improvement of computer industry elements [4]

such as internet of things (IoT), when controlling battery maintenance for a large-scale network consisting of plenty of sensor nodes is extremely difficult, if not impossible. This is the reason why energy harvesting is suggested to be an applicable alternative to be providing an independent long-term power for such devices [9, 10]. The area of energy harvesting is receiving a particular interest from researchers also because of its capability to exploit some amounts of lost energy that is wasted in the environment from its sources. Even though this harnessing happens for a small quantity, it definitely has a significant impact economically and environmentally [11, 12].

1.4 Motivation

Electronics industry worked in the past few years and still to reduce the power consumption of electronic components to sub-watts thanks to silicon-on-insulator (SOI) technology. this technology gave rise to the evolution of CMOS transistors, the very important component for advanced circuit designs such as Very Large Scale Integration (VLSI) [13]. Today's focus on low power consumption research and development is because battery-powered electronic devices have created a growing demand for energy-efficient circuit designs. Future progress will depend on the development of relatively cheap devices with complex functionality, high-performance and long lifespan batteries. The recent researches are dedicating efforts to reduce VLSI power consumption through several techniques as reported in [14].

Since the initial development of the bio-implantable cardiac pacemaker from the 1950s [15], the field of bioengineering has provided many different implantable medical devices (IMDs). They are directed to the medical profession in order to tackle various health problems such as bradycardia, fibrillation, diabetes, and disability [16]. These advances are the result of dedicated efforts of inventors and entrepreneurs who established an important new industry for IMDs. Some of these devices are listed in table 1.1.

The global bio-implants market has been estimated to be $ 94.1 billion in 2012 and is poised to grow at a compound annual growth rate of 7.3 % from 2012 to 2017. Rise in the aging population and increase in incidences of chronic diseases like osteoarthritis, old age-related trauma, cardiovascular diseases, neuropathic disorders (Alzheimers disease and Parkinsons), and congenital disorders and deformities is expected to trigger the growth of this market [17]. Today, implantable cardioverter defibrillators, drug delivery systems, neurological stimulators, bone growth stimulators, glucose sensors and other implantable devices make the treatment of a variety of these diseases

possible [16, 18]. They also give patients a lower-cost and hassle- free option for continuous monitoring of vital signs and in some cases treatment of their health conditions right from their homes with less need to have them travel to hospitals and medical clinics [19].

Pertinent deployment of an IMD is massively depending on the continuous supply of energy. In this sense, long- term powering and recharging of an IMD via a highly safe efficient and convenient way is, therefore, extremely important. Because of the battery issues and low power CMOS developments mentioned earlier, energy scavenging received a great attention in the submillimeter scale applications. Packaged high energy density batteries are capable of providing energy to the IMDs for a limited lifetime such as 8 years for some pacemakers (refer to figure B.4), based on functionality and usage, while surgical intervention is required eventually for battery replenishment. With an increase in longevity of patients, the need for long-term sustainable autonomous powering and overcoming the finite battery capacity has become imperative.

Table 1.1: Some electrical implantable devices [8, 18, 20, 21]

Orthopedic implants	**Cardiovascular implants**	**Other medical implants**
-Spinal stimulators	-Cardiac resynchronization therapy devices	-Cochlear implants
- Trauma stimulators	-Cardioverter defibrillators	-Artificial retinas
-Cerebral pacemakers	-Pacemakers	-Continuous glucose monitoring systems
-Hydrocephalic pumps	-Ventricular assist devices (VADs)	-Muscle stimulators
	-Implantable hemodynamic monitors	-Blood pressure sensors
	-Insertable loop recorders	-Drug delivery systems

1.5 Contribution

This thesis contributes to the area of energy harvesting by developing an implantable power generator capable of exploiting the kinetic energy available in the daily activities of the human body and converting it into electrical energy to power bio-implants directly or to charge their batteries. The objective of this approach is to contribute in solving IMDs power issues mentioned earlier. The harvester uses a 3D structure of micro-coils fully compatible with MEMS fabrication techniques for energy harvesting application for the first time. Their advantage of high aspect ratio offers production of higher induced voltages compared to planar coils that are commonly used in MEMS devices.

The device is designed to be capable of harvesting low frequency kinetic energy and to have a non-resonance property. The micro-generator has a total volume less than 1 cm^3, with this small footprint size, the device can be inserted safely without damaging biological tissues inside the body to provide continuous power for bio-implants from horizontal movements. These mechanical movements are available in many places in the body which makes the device suitable for implanting in several places without being dependent to a certain location that would be far from the bio-implant.

1.6 Thesis Overview

This thesis is organized as follows: In chapter two, previous works are reviewed, since the topic of the project is based on an electromagnetic induction to harvest energy, other methods reported in the literature are surveyed, and in each method we discuss issues, advantages and disadvantages, and the chapter is finished with a comparison and conclusion. The design of our harvester

is presented in chapter three, from the initial design passing through the improvements to reach the final design, in each phase, we present equations for theoretical analysis with the simulations performed on the design. Chapter four deals with prototypes micro-fabrication, here we present four fabrication phases to reach a successful and more stable micro-generator. The changes in plans are illustrated and discussed in details. In chapter five, we present and discuss the experimental results, the deice is first tested to study the platform displacement and find the friction force. After that, we present results of testing the device for open circuit voltage and power generation in two sets of tests: on a linear shaker and on wristband to mimic some daily body activities. Chapter six is the last chapter where the conclusion about the performance findings is drawn and suggestions are outlined as future work concerning the increase of coils turns to boost up the performance for battery charging paving the way to next path in research and development.

Chapter 2

Energy Harvesting Methods Background

2.1 RF Energy Harvesting

When mentioning radio frequency (RF) energy transfer or harvesting, two distinguishable types worth are listed:

a) **Nonradiative RF transfer:** Based on inductive coupling, an RF source is connected to a coil with R_c loss and self-inductance L_1 (see figure 2.1a). In the proximity of this coil, a receiving coil that has a self-inductance L_2 is placed, the signal that is present at the receiver due to mutual inductance M is used to power a load resistance R_L. A rectification and power management network can also be embedded in the receiver before the load to convert the voltage according to the load requirements. In order to insure efficiency of high power transfer, capacitors are connected in parallel to the coils as C_{p1} and C_{p2} or in series as C_{s1} and C_{s2}. The voltage that

is present at the load in the receiver is ideally directly proportional to the source voltage as detailed in the equations series by Olivo *et al.* in [7].

b) Radiative RF transfer: An antenna is connected to an RF source to make up the transmission network from which power is radiated in a form of electromagnetic (EM) waves. These waves travel in the medium to be captured by the receiver antenna in the other side [22, 23]. After the signal is rectified, its energy is stored in a battery or dissipated in a load. The receiver antenna with the rectification circuit is called also rectenna (dashed box in figure 2.1b). Assuming the maximum directivity of the two antennas, the relation between transmitted and received power is expressed with Friis equation [24].

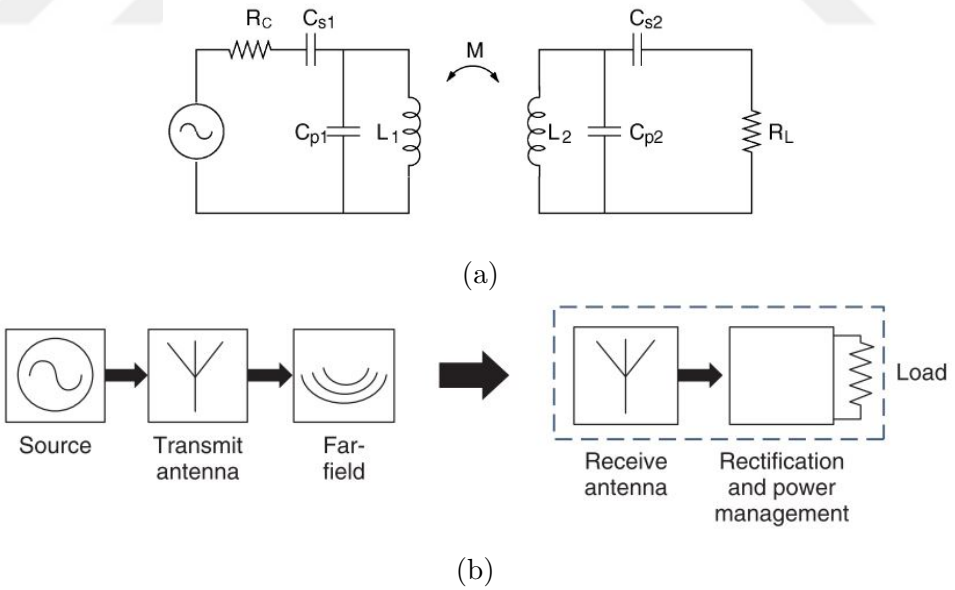

Figure 2.1: RF Energy harvesting types:(a) inductive coupling system and (b) radiative energy transmitter-receiver system [24, 25].

The RF energy harvesters used for bio-implantable applications are subject to extension in order to perform bi-directional transfer, downlink for power and control signals transfer, and uplink for data reading [23, 26–28]. Harvesting

or transferring energy through RF waves is the most popular way developed according to the literature. The use of inductive links to power implants has been deeply investigated, the designs use the transmitter outside the body to drive the RF signal through the skin tissue to the implanted receiver. It has been shown that inductive links used for implantable chips are capable of delivering noticeable amounts of milliwatts of power from 0.14 mW up to 150 mW at frequencies in the range of 0.7 MHz at 1.2 V to a maximum of 915 MHz [7], such power values are high enough to operate several subcutaneous electronic bio-implants (Figure 2.2). A lot of factors can affect the transmission efficiency as the tissue thickness and angular misallignment of the coils [26, 29]. In [23] three types of antennae designs simulations show an example of power dropping from 90 µW to 0.3 µW when the implant depth is increased from 1 cm to 8 cm, an angular misalignment of 45° in [26] causes the power at the load to drop by two thirds.

The efficiency of such harvesters is described to be low. For instance, a hybrid resonator for wireless power transfer is reported to have a maximum efficiency at the receiver load to be 9.41% with transmitter receiver distance set to be 5 cm [30]. Although the efficiency can be boosted up to a maximum of 23% in the GHz frequencies [1], it can also be compensated when the transmitter power is increased to insure receiving enough power at the receiver. Controllable transmitter source can be a drawback when the implant depends on huge hand-held charging source (figure B.1). On the other hand, high power values can lead to a remarkable heating effect in the tissue located near to the receiver during transfer. That is why, for safety reasons, the source has to be controlled not to exceed the maximum absorption rate level (SAR) which is related directly to tissue temperature and differs from tissue to another within the range 1.6-4 W/Kg according to IEEE regulations [7, 23, 25, 31].

(a) (b)

Figure 2.2: Examples of devices powered with RF waves: (a) an assembled receiver in bio-compatible package to be used as endoscope next to 1 eurocent coin, (b) cochlear implant, RX coil positioned beneath the skull behind the ear to be powered by the external coil TX [29, 31].

2.2 Thermal Energy Harvesting

Heat is another form of plentiful energy present in the environment, therefore it implies an urgent need for developing devices to recycle it. With advances in materials science, thermo-electric properties of some materials and alloys has been studied and utilized for applications as high temperature thermometers and thermo-electric generators (TEGs) that are built based on Seebeck effect. Seebeck effect is the direct conversion of temperature difference between two dissimilar doped materials such as n−poly−Si, n/p−$Bi_xSb_yT_z$ and poly−SiGe, connected thermally in parallel and electrically in series to form the thermo-couple unit [32]. Seebeck effect is atomically the diffusion of the majority charge carriers from the hot to the cold region. Several connected units build up the TEG as shown in Figure 2.3. The voltage V that is generated across a thermal generator is expressed as:

$$V = \int_{T_1}^{T_2} [S_B(T) - S_A(T)]dT \tag{2.1}$$

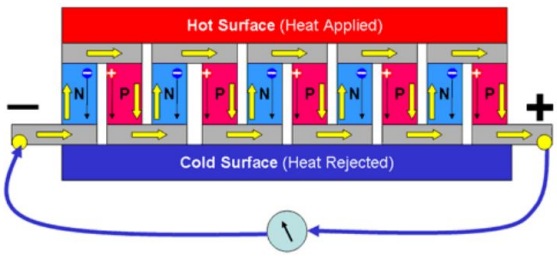

Figure 2.3: A diagram of a thermo-electric generator [33].

Where T_2 and T_1 are the temperatures present at the hot and cold surface, respectively, and S_B and S_A are the Seebeck coefficients (in V/K) of the two dissimilar materials [7].

The generator efficiency is defined as Carnot efficiency that is the ratio $\Delta T/T_H$ where ΔT is the temperature difference between T_H the hot surface temperature and the cold surface temperature across which the generator is operating [4].

A thermo-electric generator of $0.21\,\mathrm{cm}^2$ surface is capable of producing $2.5\,\mathrm{nW}$ at $\Delta T = 10\,^{\circ}\mathrm{C}$ with an open circuit voltage V_{OC} of $0.1\,\mathrm{V}$. Under the same temperature gradient, this power can be increased up to $18\,\mu\mathrm{W}$ with hundred folds of voltage increase by enlarging the thermo-generator surface to $1\,\mathrm{cm}^2$ [34, 35]. In fact, the temperature difference at the surface of human body is much lower, although areas as wrist and ankle can insure a considerable temperature differences due to blood vessels, a maximum ΔT of $4.75\,\mathrm{K}$ is achievable during running activity at $25\,^{\circ}\mathrm{C}$ room temperature [7, 32]. In addition to the generator location, the performance depends on the choice of fabrication material and generator design. For example, a TEG based on poly−SiGe provides a power density of $4.5\,\mu\mathrm{W/cm}^2$ compared to BiTe generator which offers a value as high as $30\,\mu\mathrm{W/cm}^2$ [36].

Although the efficiency of TEG is reported to be as small as 1% for $\Delta T = 20\,^{\circ}\mathrm{C}$ [32, 37], yet the thermal energy harvesting is largely engineered for wearable electronics [4, 5, 37, 38] and it is commercially available (see Figure 1.1a).

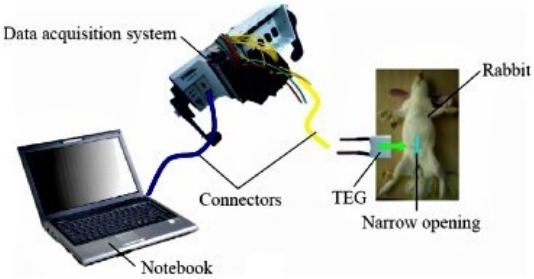

Figure 2.4: Experiment setup of an implanted TEG in rabbit abdomen [41].

As for bio-implantable applications, few works were dedicated to exploit thermal energy in the literature [39–41]. Yang *et al.* reported simulations of a TEG positioned in a depth of 7.1 cm, it is mentioned that the maximum temperature difference has been found to be 1.142 °C. *In vivo* experiments carried out on a rabbit abdomen (Figure 2.4) revealed an output V_{OC} to be 5 mV with an estimated power of 14.4 µW delivered at 100 kΩ [41].

2.3 Bio-fuel Cells

Bio-fuel cells (BFCs), one of many achievements of micro-fabrication, is a miniaturized electro-chemical cell that is made to convert the energy of biomass to electrical energy. It operates by extracting electrons from chemical compounds via oxidation/reduction reaction. The chemical reaction inside the cell occurs with the intervention of catalysts according to which the bio-fuel cells are usually classified: bacteria as *Shewanella* species, enzymes as laccase or abiotic as platinium [8, 24, 42]. As shown in Figure 2.5, in the anode compartment, organic fuel (vinegar) is supplied into the system, and the bio-catalyst (bacteria) converts vinegar into glucose during the metabolism process. The generated electrons move from the anode electrode through the load to the cathode. The fuel and the oxidant streams are separated by a membrane that allows only protons to pass to cathode compartment to reduce the oxidant and

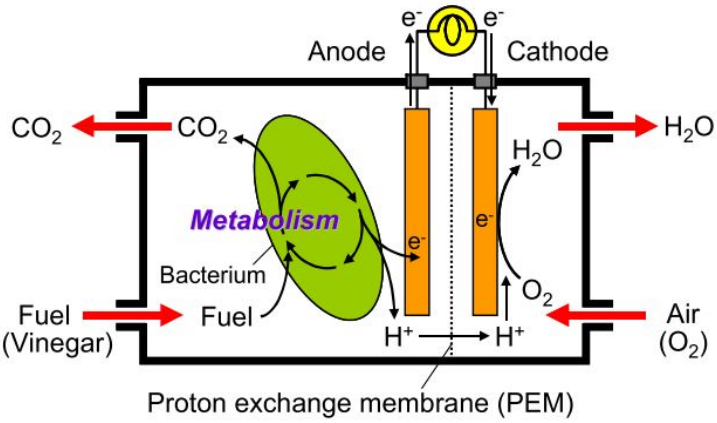

Figure 2.5: Schematic diagram of a bacterial fuel cell extracting electrons from vinegar fuel during metabolism [43].

the overall reaction is described as,

$$C_6H_{12}O_6 + 6\,O_2 \longrightarrow 6\,CO_2 + 18\,H_2O \tag{2.2}$$

A microbial fuel cell (MFC) is capable of generating out of glucose fuel a potential of 21 mV [44] to 265 mV at 1 kΩ [45]. The power density harvested by an MFC at the transverse colon from intestinal fluid can reach only 7.33 µW/cm^2 [46]. These experimental values are shown to be stable only for short periods of time then decay in less than a month. Enzymatically catalyzed cells can provide a higher power density as 440 µW/cm^2 [47] yet their duration of stable power generation is reported to be capable of only meeting the demands of bio-implantable devices for short-term application as a month in favorable cases [8,48]. Abiotically catalyzed fuel cells exhibit a lower performance in the order of 50 µW/cm^2, nevertheless, it can successfully last for longer period as 150 days [49]. In addition to catalyst choice, a couple of different operation conditions that affect the performance are taken into consideration including temperature, pH of the medium, reactants flow rate and electrodes surface-area-to-volume ratio (SAV) [43,44,47,50–53].

The major attraction for the glucose BFCs since few decades is due to the fact that the fuel and the reaction products are highly bio-compatible and

available in the bloodstream. That is the reason why it can be deployed for *in vivo* MEMS-based applications [53]. A pacemaker has been successfully operated in [52] after its battery was replaced by an enzymatic fuel cell working on glucose fuel (figure 2.6a). In order to enhence power density, other improved designs are suggested such as membrane-less fuel cells to decrease cell volume and lower ohmic losses [42], and carbon nanotube (CNT) electrodes to improve their SAV (figure 2.6b) [43].

(a) (b)

Figure 2.6: (a) bio-fuel cell charging pacemaker setup: (A) from right to left, bio-fuel cell, charge pump interface, pacemaker, implantable loop recorder, sensor, (B) battery powered pacemaker pulses, (C) BFC powered pacemaker pulses, (b) an assembled MFC with high SAV using CNTs compared with a one-cent US coin [43, 52].

2.4 Electrostatic Energy Harvesting

Electrostatic forces are both impractical and inefficient in the macro-scale transduction applications. Because these forces depend on the surface, then according to scaling laws they become much more significant. They become practical at small size scales and are well suited for MEMS electrical power generators implementation [5]. The electrostatic generator (ESG) is simply a

capacitor with two parallel plates of area A separated by a distance d by a medium with permittivity ε. The relation between the capacitor plate charge Q and its potential V is,

$$Q = \frac{\varepsilon.A}{d}.V \tag{2.3}$$

As for the stored energy, it is $E = 1/2.QV$. Two different methods of operation in which the electrostatic forces can be used to generate electrical energy [54]:

a) Constant charge: it is the case where a pre-charged capacitor with low voltage is subject to a mechanical force to increase the gap distance between its plates (figure 2.7), leading to an additional energy storage in a form of electric field that can be used to power a load.

b) Constant voltage: by applying a horizontal force that changes the active area of interdigitated plates of a pre-charged capacitor and forces the charge to circulate across a connected load (figure 2.7).

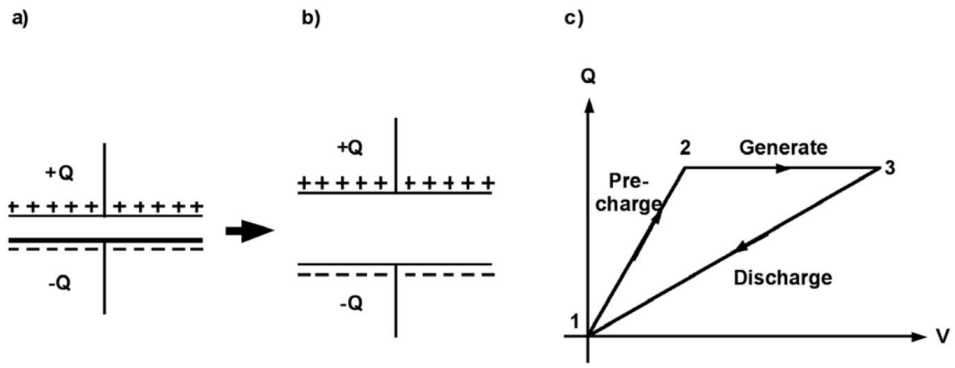

Figure 2.7: Electrostatic generator operation at constant charge: a) and b) before and after increasing the plates inter-distance, and c) the Q-V diagram of a complete cycle [54].

The potential generation for the ESGs has been shown to reach 58 µW of power with a constant voltage from 24 V at 4.76 Hz excitation frequency [55] to 80 µW with 120 V at 30 Hz [56]. Some issues should be prevented in designing ESGs such as air damping trouble due to packaging, and plats impact that damages

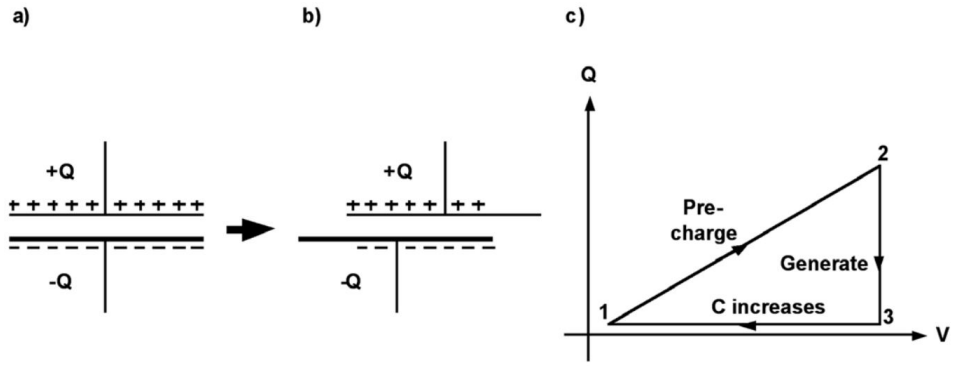

Figure 2.8: Electrostatic generator operation at constant voltage: a) and b) before and after increasing the plates active area, and c) the Q-V diagram of a complete cycle [54].

the structure under high excitation which is avoidable using mechanical stops [32].

ESGs need to be recharged to operate, although they show high voltages, they have low efficiency which limits their feasibility for some applications [7]. Electrets are suggested to be used as recharging sources (Figure 2.9), electrets are analogous to magnets, made of materials based on SiO_2 such as SiO_2/Si_3N_4 or polymers such as fluorinated parylene. They behave as charge traps that are reported to handle high potentials up to 300 V with a long lifetime as 50 years [54, 57]. A charge pump also can supply the charges to the capacitor by siphoning the required energy to maintain the cycle [32].

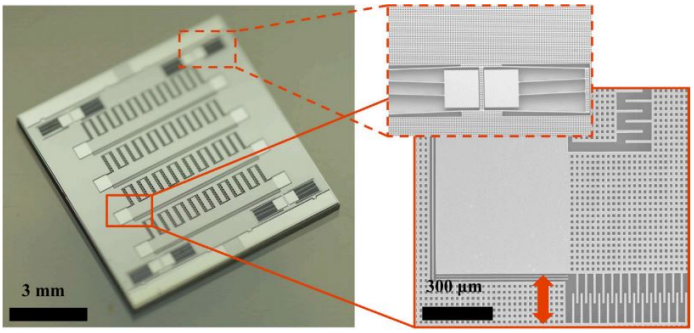

Figure 2.9: Comb drives ESG with a pre-charging electret [57].

2.5 Piezoelectric Energy Harvesting

Piezoelectricity phenomenon as mentioned in section 1.2 is discovered a long ago. The direct piezoelectric effect, as shown in figure 2.10a, is the conversion of mechanical energy to an electric field when the applied mechanical work of the force F is converted into electric energy. This happens by misshaping the symmetric crystal so that the central ion moves from the center creating polarization and energy is stored in a form of electric field [58], this is the reason why piezoelectric transduction is well suited to the reciprocating motions like vibrations. This phenomenon is seen in materials such as lead zirconate titanate ceramics (PZT), aluminium nitride (AlN), zinc oxide (ZnO) and some polymers [24]. The general constitutive relation between the applied stress vector σ and the resulting electric displacement vector $\mathbf{D}$ for direct piezoelectricity is described in [59] as,

$$\mathbf{D} = \mathbf{e}^{\sigma}\mathbf{E} + \mathbf{d}^{\mathbf{d}}\sigma \tag{2.4}$$

Where $\mathbf{e}^{\sigma}$, $\mathbf{E}$ and $\mathbf{d_d}$ are vectors for permittivity, electric field and piezoelectric coefficients, respectively. There are two commonly used coupling modes for direct piezoelectric effect, identified by the direction of the mechanical force and polarization. The direction of polarization is conventionally denoted as the '3' direction. As shown in figure 3.9b, d_{31} mode implies that charges are collected on the electrode surface perpendicular to the polarization direction when tensile or compressive force is applied perpendicular to the polarization axis, and d_{33} mode is for the case when the applied force is parallel to the polarization axis [60]. Piezoelectric generators are commonly suggested power sources for wearables and portable electronics mounted in shoes, near muscles or joints to exploit the present stress [5, 61]. For example, in a shoe mounted cantilever, a voltage of 50 V and a maximum power of 0.3 mW are achievable at 40 Hz [62].

For bio-implants powering applications, it is anticipated that piezoelectric

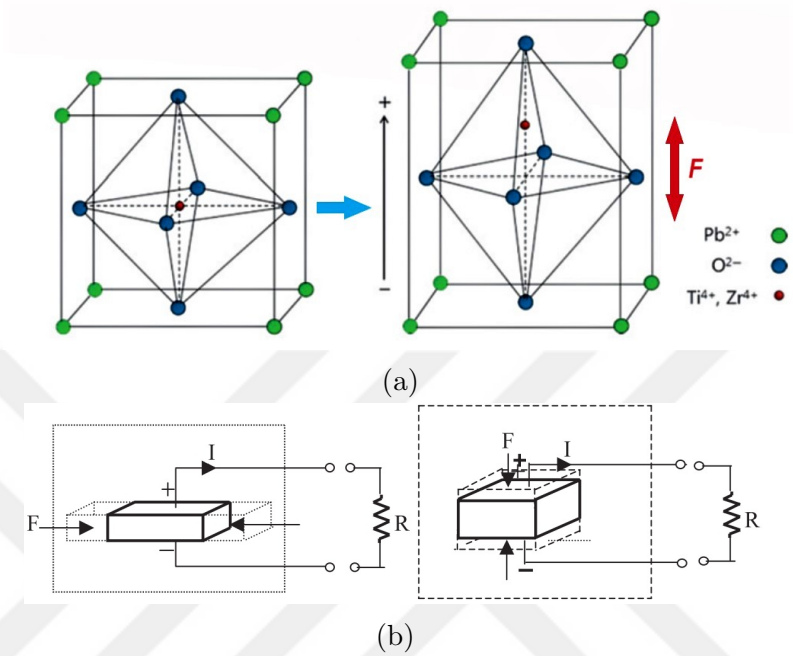

Figure 2.10: Piezoelectric principles:(a) symmetric crystal (left) and when a vertical force F is applied to move the central ion up creating polarization in the crystal, and (b) the conventional coupling modes for current generation d_{31} (left) and d_{33} (right) [58, 60].

scavengers are feasible [63]. In [64], a piezoelectric harvester connected to rabbit quadriceps produced 1 µW that is enough to power a muscle stimulator. Flexible PZT generators reported by Dağdaviren *et al.* (Figure 2.11) were *in vivo* tested in bovine heart and lung, and were able to power a pacemaker [65].

Piezoelectric generators pose some particular issues, although they produce high voltages, achieving high power requires hitting resonance frequencies higher than the ambient vibrations ranging from 50 Hz to hundreds of Hertz because of their small size as microstructures [5, 64]. Also, high dielectric constants for some materials (1000 for PZT) lead to high impidence demanding big matching loads for maximum power generation. Some high power values reached with small footprints are obtained with unpackaged devices and could significantly be damped once harvesters are packaged [7, 24].

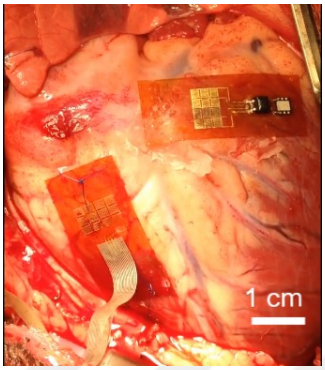

Figure 2.11: PZT generators implanted in bovine heart [65].

2.6 Electromagnetic Induction Energy Harvesting

Electromagnetic harvesters employ mechanisms that use vibrations to make relative motion between magnets and coils. Energy conversion is based on the magnetic flux that changes in a coil, this leads to an induced electric potential across the coil, called an electromotive force (emf). This phenomenon is known as induction law of Faraday. The equation describing Faraday's law in case of a coil of N turns is,

$$V_{emf} = -N\frac{d\varphi}{dt} = -N\frac{d}{dt}\left(\int_S \mathbf{B}\,.\,d\mathbf{S}\right) \tag{2.5}$$

Where V_{emf} is the induced voltage and φ is the magnetic flux, that is also the surface integral of the flux density $\mathbf{B}$ and the coil surface $\mathbf{S}$ vector product. A schematic diagram shown in figure 2.12 of a generic inertial generator, $y(t)$ is the frame displacement when it experiences an external force. The proof mass m, which can be a magnet, attached to a spring undergoes a relative displacement $z(t)$. Energy is converted when work is done against the damping force $f(\dot{z})$ and the damper represents coils that oppose the magnetic flux change by generating an electric potential. The most reported magnets to be used are NdFeB rare earth magnets for their strong flux density [66–68].

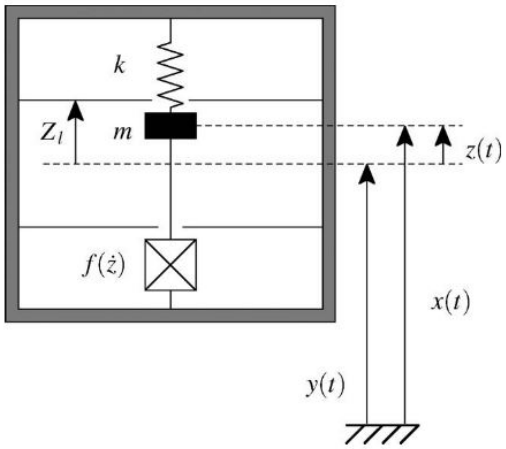

Figure 2.12: A general mechanical model of an inertial generator [5].

Electromagnetic generators are commonly mounted in wearable devices (Figure 1.1b), shoes, backpacks or moving body parts as knees [11, 69, 70]. A micro-generator of 0.25 cm^3 volume is reported to produce power of 2 - 25 µW from different body locations [71]. In [72], a generator with resonating diaphragm configuration at 50 Hz, a voltage of 7.5 mV and an output power of 190 nW was delivered to 300 Ω load. Higher performance as 680 µW and 4.4 V_{pp} at frequencies 60-110 Hz could easily drive an IR remote control [73]. Rotational electromagnetic harvesters are capable of generating fair amount of power, however, they are not convenient for harvesting from the ambient and impractical for implantable devices [32, 74, 75]. Inertial micro-harvester design for bio-medical devices was developed in [20] with a footprint of 0.5 mm^3 to produce 1.1 V_{RMS} with an estimated 0.4 mW output power. Non-resonant or wide-band low frequency harvesters are more practical to respond to wide range of ambient vibrations, an example of this is a 1.5 cm^3 generator reported in [76] to produce up to 35 µW in the range of 2 - 10 Hz (figure 2.13). Some important factors are mentioned to decrease performance of electromagnetic harvesters such as losses caused by eddy currents or damping due to friction. Temperature during fabrication or operation also has to be much below the

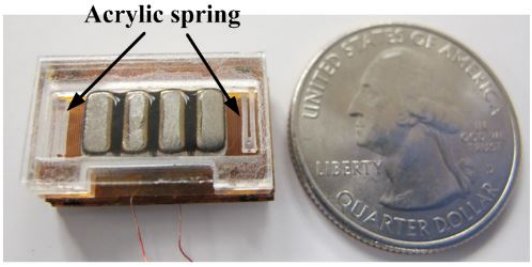

Figure 2.13: A prototype of a non-resonant electromagnetic energy harvester with quarter dollar [76].

Curie temperature to prevent magnetization loss of magnets [24].

2.7 Conclusion and Summary

A general overview of several methods are covered to be useful for exploiting energy from the environment and be a source of power for implantable devices. So far, lithium batteries still remain dominant in this area because of their high energy density, however, their lifetime is not satisfactory. One possible way to overcome such limitation is to develop devices that are capable of extracting ambient energy in order to charge batteries or to directly feed the electronic devices.

RF harvesters are already commercially available. They can provide high power to bio-implants by controlling the source, which may be seen as a drawback from the perspective of external source dependence. The transmission distance can make them practical for subcutaneous implantation but not for invasive devices. Thermal generators are an alternative that has low efficiency and can provide high power in high temperature gradients or when stuck in arrays. They depend on location which limits their application for some implants. Enzymatically catalyzed bio-fuel cells provide power density better than the bacterial cells, however, both have short lifetime. Abiotic ones are

more stable and can operate for longer time. In areas where motion and vibration is available, vibration based methods i.e. electrostatic, piezoelectric and electromagnetic, are the best choice. Power density is important to be considered for bio-implantable devices to insure less volume producing adequate power, and this would be in favor of piezoelectric and electromagnetic generators. For motion based implantable generators, packaging in vacuum is necessary to overcome damping losses.

Hybrid harvesters are also suggested to exploit more energy by means of coupling two methods as piezoelectric and electrostatic transduction [5, 77]. A few other methods were not covered in this review, which are less reported in the literature and have not been proven to be useful for implantable devices such as photo-voltaic micro-generators that cannot be implanted since they need exposure to light. Also, hydrocarbon and nuclear based micro-fuel cells have high power density but are impossible to be implanted because of fuel and heat control difficulty for the former and potential radioactivity danger for the latter [20, 41, 46, 48].

Generators developed for bio-implantable devices have to be well encapsulated in bio-compatible materials as platinium or some polymers which should not elicit an adverse response from the body and vice-versa [78].

Chapter 3

Harvester Theory, Design & Simulations

This chapter contains detailed design of the energy harvester followed by theoretical calculations and simulations. A design is initially proposed to start with, then updates are made following the simulation and calculation findings. Some improvements in the design and materials are also made later to address issues that arose during fabrication phase as explained in chapter 4.

3.1 Initial Design

The initially proposed harvester consists of two movable platforms, a pair of stators, permanent magnets, micro-coils, and ball bearings. One single platform contains two trenches on the sides to house the micro-balls, and has in the middle two cuboid openings where permanent magnets are placed with alternating polarity (figure 3.1a). A stator has also two micro-balls trenches on

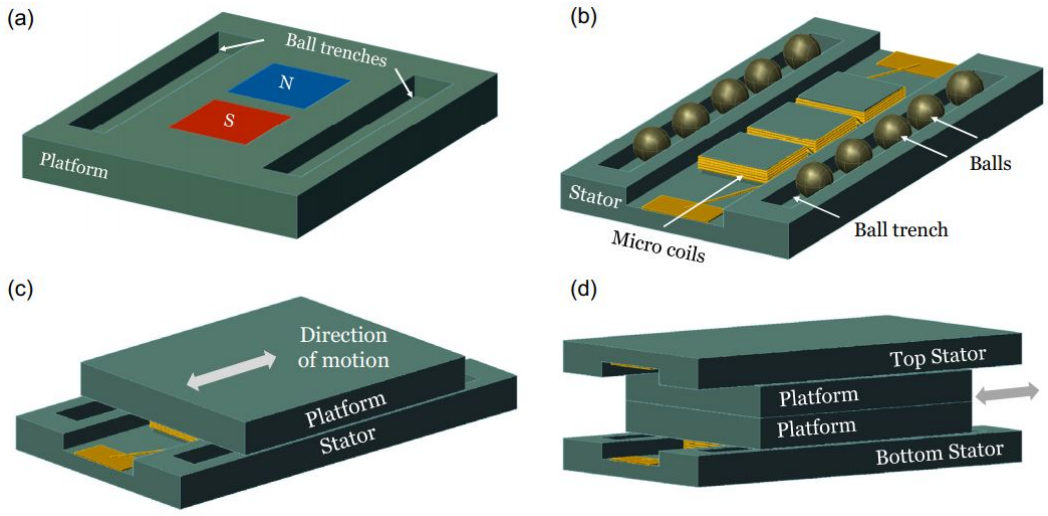

Figure 3.1: Proposed micro-generator design:(a) platform with embedded magnets and balls trenches, (b) stator with serially connected wound micro-coils and balls on side trenches, (c) platform placed on stator showing motion direction and (d) a compact view of the assembled micro-generator.

the sides; it contains three aligned micro-coils serially connected (figure 3.1b). When the platform is flipped over the stator, the trenches fit on the micro-balls allowing the platform to move in the direction shown in figure 3.1c. Stacking another platform and a stator on the top makes up a complete micro-generator unit (figure 3.1d).

The material chosen for building the platform and stator is initially poly-dimethilsiloxane (PDMS), that is $(C_2H_6OSi)n$, a bio-compatible and flexible polymer, that is widely used in bio-implantation applications [79]. The magnets chosen for the platform are NdFeB for their strongest remnant flux density of 1.4 T, micro-balls initially were chosen to be plastic, the number of balls per trench is chosen to be four to insure a stable motion of the platform with maximum possible travel distance that is 2.5 mm. Trench depth is chosen so that platform-to-stator gap is 50 µm when the platforms are sandwiched by the stators. Both micro-balls and magnets are available off-the-shelf.

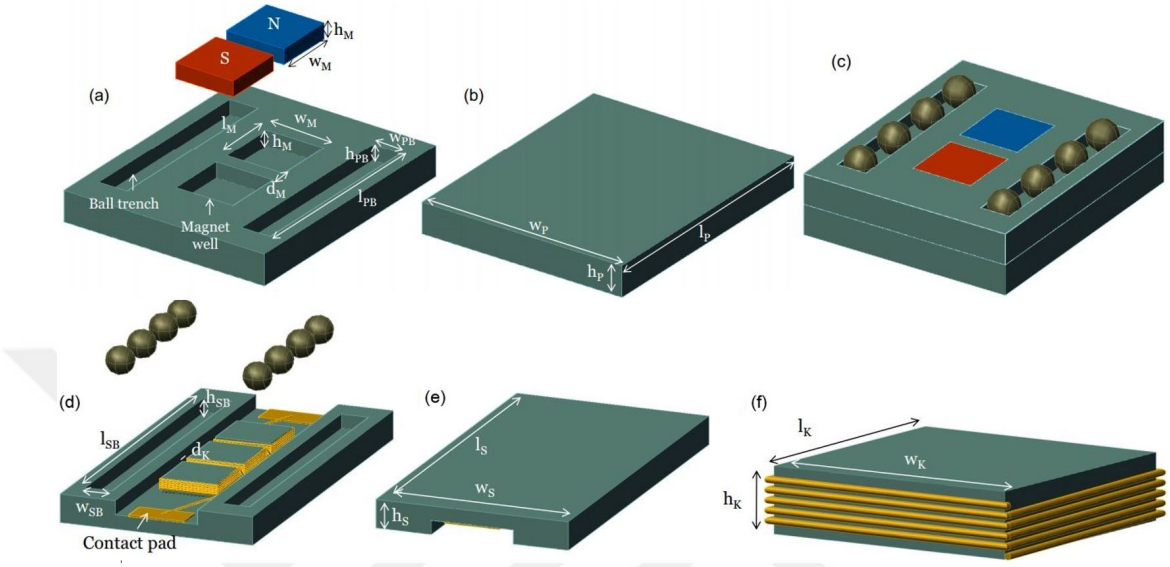

Figure 3.2: (a) platform with magnets detached, (b) platform from the back, (c) two assembled platforms with micro-balls on trenches, (d) stator with 3D micro-coils and micro-balls, (e) back view of the stator and (f) a post with wound micro-coil (few turns are represented for simplicity, dimensions are not to scale).

The 3D solenoidal micro-coils of the stator are advantageous over the planar coils which have microfabrication complexity and number of turns limitations [80], the 3D micro-coils are electrically insulated, and can be wound multiple times around columns to improve output power, this process is fully MEMS compatible made by a wire bonder developed by Kratt *et al.* [80–83], the wire is 25 µm diameter made of Au with 2 µm insulation coated by Polysol 155 [81]. The platform parts and their parameters are shown in figure 3.2a-c. The same for the stator in figure 3.2d,e, and a 3D helical micro-coil is shown in figure 3.2a-f. All these parameters are summarized in table 3.1.

Table 3.1: Initial micro-generator parameters

Platform and stator material	PDMS
Platform size $l_P \times w_P \times h_P$	$7 \times 7 \times 1$ mm
Magnets material	NdFeB
Magnets size $l_M \times w_M \times h_M$	$2 \times 2 \times 0.5$ mm
Inter magnets distance d_M	0.5 mm
Micro-balls material	Plastic
Micro-ball diameter	1 mm
Micro-balls number	4
Platform trench size $l_{PB} \times w_{PB} \times h_{PB}$	$5 \times 1.05 \times 0.5$ mm
Stator size $l_S \times w_S \times h_S$	$11.5 \times 7 \times 1$ mm
Column size $l_K \times w_K \times h_K$	$2 \times 2 \times 0.45$ mm
Inter columns distance d_K	500 µm
Micro-coil material	Au
Micro-coil wire diameter $2r$	25 µm
Number of Coil turns N	100
Stator trench size $l_{SB} \times w_{SB} \times h_{SB}$	$5.5 \times 1.05 \times 0.45$ mm
Platform-stator air gap d_{PS}	50 µm
Platform total travel distance	2.5 mm

3.2 Operation Principle and Analysis

The two stators are fixed to the package (not shown in figure 3.1d for simplicity), so they move together when the device is subject to a horizontal displacement due to body motion. The rolling micro-balls from top and bottom make the platform to slide relatively to the opposite direction with velocity v (figure 3.3a) and the micro-magnets horizontal magnetic flux changes in the micro-coils of area A inducing a voltage V according to Faraday's law as defined in section 2.6. To simplify analysis, curves in figure 3.3b are approximated to straight lines. For three serially connected coils, equation 2.5 becomes,

$$\begin{aligned} V &= NA\left[\left|\frac{dB_{zl}(t)}{dt}\right| + \left|\frac{dB_{zm}(t)}{dt}\right| + \left|\frac{dB_{zr}(t)}{dt}\right|\right] \\ &= NA\left(\frac{B_{zmax}}{T} + \frac{2B_{zmax}}{T} + \frac{B_{zmax}}{T}\right) = 4NA\frac{B_{zmax}}{T} \end{aligned} \tag{3.1}$$

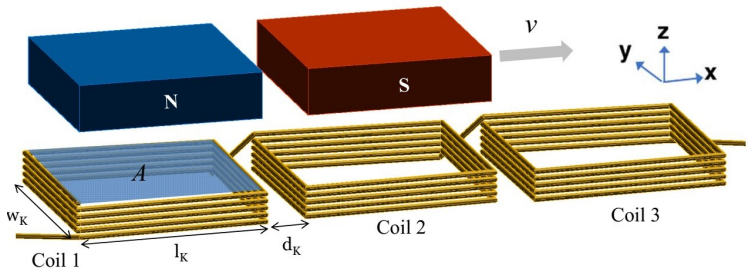

(a)

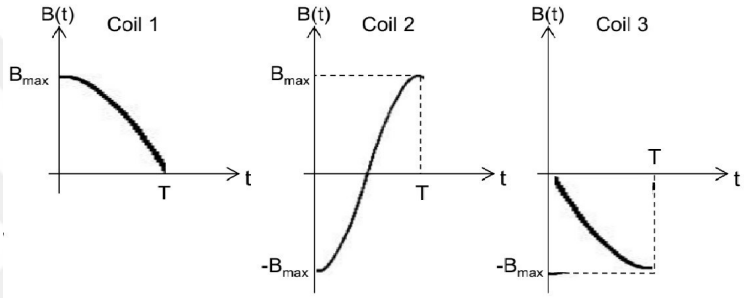

(b)

Figure 3.3: (a) magnets displacement relative to micro-coils and (b) sketch of the corresponding flux density in each coil.

The voltages in the equation are taken in absolute values because the coil winding direction is taken into account to make sure to have additive voltages. Subscripts l, c and m are for left, middle and right coil, respectively. z subscript denotes the component of magnetic flux density, the two other components along x-axis B_x and y-axis B_y are parallel to the coil surface, thus, they do not contribute in voltage induction. T is the time required for the magnet to move $l_k + d_k$ total distance, then $V(t)$ can be rewritten

$$V(t) = 4Nl_k w_k \frac{B_{zmax}}{l_k + d_k} v(t) \tag{3.2}$$

the induced voltage will have the same shape as velocity v i.e sinusoidal with frequency f. The load impedance Z is expressed as,

$$Z = \sqrt{R^2 + 4\pi^2 f^2 L^2} \tag{3.3}$$

Where R and L are coils resistance and inductance, respectively. The output RMS power is related to Z and V as follows:

$$P_{rms} = \frac{1}{Z}\left(\frac{V_{rms}}{2}\right)^2 = \frac{V^2(t)}{8Z} \tag{3.4}$$

The inductance for such square-shaped coil ($l_k = w_k$) can be approximated as mentioned in [84] and rewritten for a single stator as,

$$L \approx 3N\frac{2\mu_0 l_k}{\pi}\left[\ln\left(\frac{l_k}{r}\right) - 0.52401\right] \tag{3.5}$$

here $\mu_0 = 4\pi \times 10^{-7}$H/m is the free space permeability. As for the resistance

$$R \approx 3N\frac{2(l_k + w_k)\rho}{A_w} \tag{3.6}$$

here ρ is the wire resistivity, and A_w is the wire cross section area. For typical walking activity, the body moves at average speed of 1 m/s, with platform total traveled distance 2.5 mm, T in equation 3.1 becomes 2.5 ms and the voltage frequency then will be f =200 Hz, in fact, plugging the micro-coil parameters in equation 3.5 gives $L = 1.2173 \times 10^{-6}$H which is very small and negligible compared to the resistance for f below MHz level in equation 3.3, hence it is safe to consider the micro-coils to be purely resistive in low frequencies ($Z = R$). When the device is assembled, the two stators will be conected in series and the total open circuit voltage V_t, resistance R_t of Au wire and RMS power P_{trms} will be,

$$V_t(t) = 8Nl_k\, w_k\, \frac{B_{zmax}}{l_k + d_k}\, v(t) \tag{3.7}$$

$$R_t = 600N(l_k + w_k) \tag{3.8}$$

$$P_{trms}(t) = \frac{Nl_k^2\, w_k^2\, B_{zmax}^2}{75(l_k + w_k)(l_k + d_k)^2} v^2(t) \tag{3.9}$$

A magnetic flux density B_z at distance z above a cuboid magnet has a remnant flux density B_r according to [85] is,

$$B_z = \frac{B_r}{\pi}\left[\arctan\left(\frac{l_M.w_M}{2z\sqrt{4z^2+l_M^2+w_M^2}}\right) - \arctan\left(\frac{l_M.w_M}{2(z+h_M)\sqrt{4z+h_M)^2+l_M^2+w_M^2}}\right)\right] \tag{3.10}$$

This equation is valid only for a point above the center of the magnet, finding the volume flux density passing through the coil is difficult by calculation due to nonlinear effects including magnetic flux leakages and the varying curvature of flux lines, instead, results are found by finite element analysis using AC/DC model in COMSOL Multiphysics®. Figure 3.4 shows the dashed line along which B_z distribution data is collected. The simulation is performed by setting the platform position to magnet-to-column perfect alignment for maximum horizontal magnetic flux in figure 3.4a along the top surface of columns, and figure 3.4b along the bottom surface. A 2D graph of the same B_z distribution, for top columns surface in figure 3.4c in which the maximum value for B_z is 0.42 T and bottom surface in figure 3.4d with a maximum of 0.22 T indicating a noticeable difference of flux density across the coil height.

To calculate maximum voltage, resistance and power, the maximum volumetric flux density B_{max} has to be found. This can be expressed as,

$$B_{max} = \frac{1}{V_k}\int_{V_k} B_z.dV \tag{3.11}$$

Here V_k is the column volume, according to the simulation, B_{max} is found to be 0.234 T. Solving equation 3.7, 3.8 and 3.9 according to the simulation finding with initial device parameters in table 3.1, the total device voltage, resistance and power values are $V_t = \mathbf{0.3\,V}$, $R_t = \mathbf{240\,\Omega}$ and $P_{trms} = \mathbf{46.73\,\mu W}$.

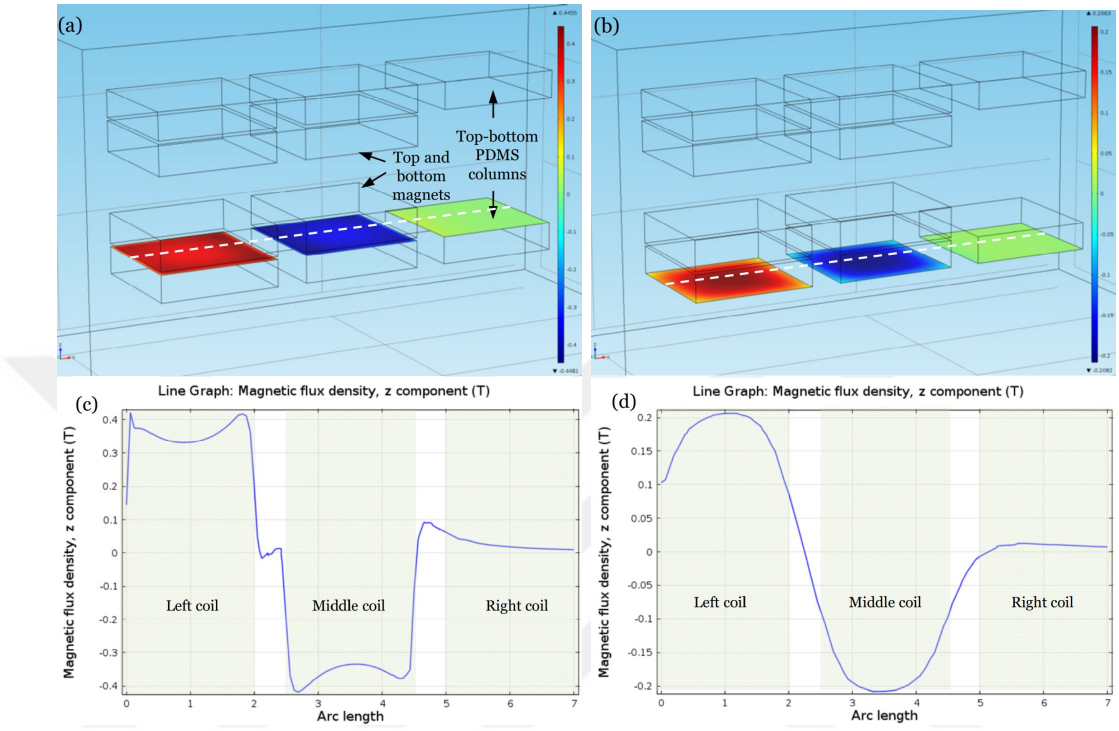

Figure 3.4: COMSOL simulations of B_z on the line on the top surface of columns (a) and bottom surface (b). B_z along the stator length on top columns surface (c) and bottom surface (d).

3.3 Updated Design

After the magnets are integrated in the upper and lower platforms, experiments showed that it is possible to combine the two platforms in a single 2 mm thick platform, also two magnets having dimensions $l_M \times w_M \times h_M = 2.5 \times 2.5 \times 2$ mm can be used instead of four small ones (updated dimensions are in table 3.2. Two magnets could be stood side by side as shown in figure 3.5, the torques generated by the magnetic force on the upper and lower sides cancel out, so that the two magnets are attracting each other without falling down by the friction of the side walls of the platform walls. Therefore, the desired structural stability is achieved.

Simulations for the updated design are done for platform set at the rightmost position in figure 3.6, At the top graph, the representation of magnetic flux density on the top surface of columns reaching a maximum of 0.65 T, and the bottom figure shows the magnetic flux density at the bottom surface of columns that reaches a maximum of 0.39 T. The volume average flux density is found to be 0.443 T. According to these updates, $V_t = \mathbf{0.47\,V}$ and $P_{trms} = \mathbf{167.47\,\mu W}$. The increase in magnet surface and using the free space in the previous platform design leads to a denser magnetic flux that yields to an increased voltage and a fourfold higher power.

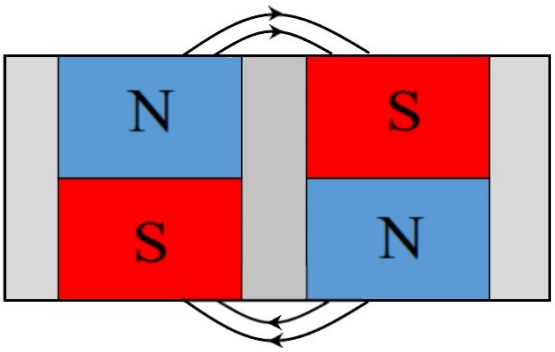

Figure 3.5: Side view of the updated design using single platform with two magnets, showing magnetic flux lines that stabilize them inside the platform (dimensions are not to scale).

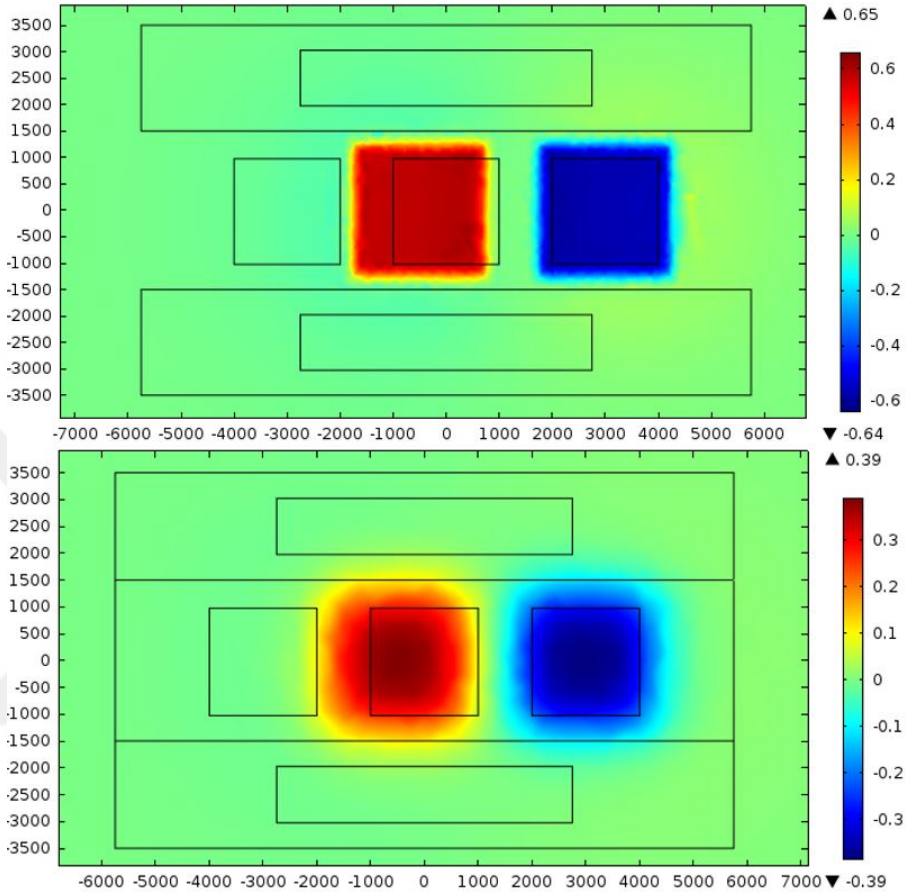

Figure 3.6: Surface z-component of magnetic flux density on the top surface of columns (top), and bottom surface (bottom).

3.4 Final Design

This final design of the stator is developed after prototype fabrication using square shaped columns design, also materials are updated, the platform is made of Aluminium, the stator is made out of silicon, the coil posts are chosen to be of SU-8 photoresist, copper is chosen for coils wire and number of turns is changed as well, and silicon nitride micro-balls are used instead of plastic ones. All of these changes are made after some limitations encountered during

micro-fabrication and wire bonding processes, every change is explained and justified in details in chapter 4. Here the geometry of the columns is changed to cylindrical with radius $r_K = 1\,\text{mm}$, and the final device structure is shown in figure 3.7. All the final parameters are summarized in table 3.2.

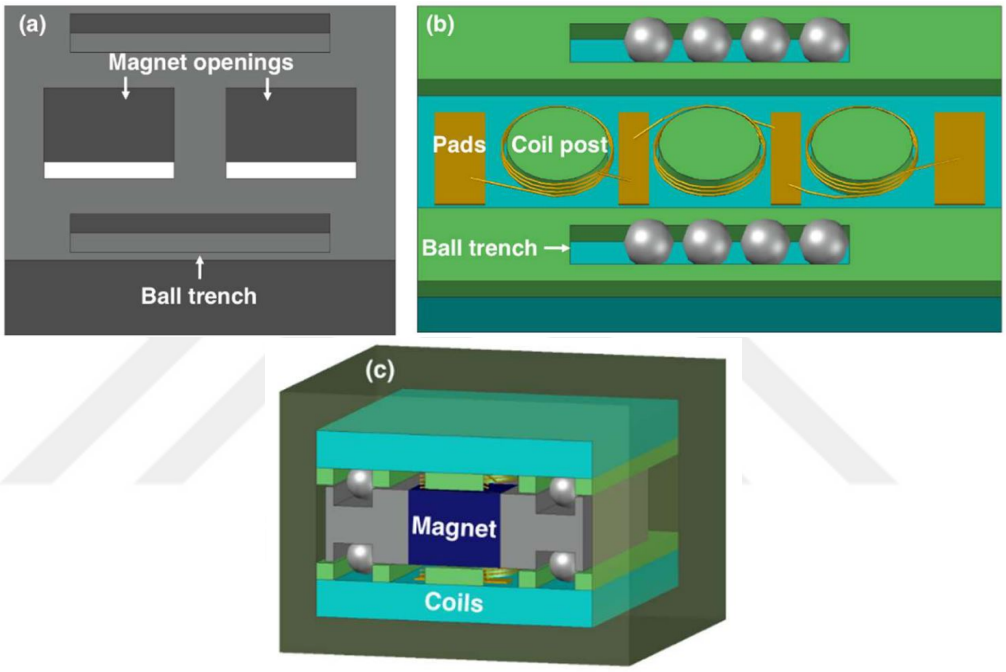

Figure 3.7: (a) Platform final design shown with openings without magnets, (b) a view of the final stator design with cylindrical coil posts, and (c) a cross-sectional view of full device with a package.

The geometry of coils is changed (figure 3.8), and the performance changes as a result. Therefore, the performance analysis of the device is performed again, equation 2.5 can be rewritten as:

$$\begin{aligned} V(t) &= V_l(t) - V_m(t) + V_r(t) \\ &= N.A.\left(\frac{dB_{zl}}{dt} - \frac{dB_{zm}}{dt} + \frac{dB_{zr}}{dt}\right) = N.A\frac{dB_{zt}}{dt} \end{aligned} \tag{3.12}$$

Table 3.2: Final parameters of the micro-generator*

Platform / stator / posts material	**Al / Si / SU-8**
Platform size $l_P \times w_P \times h_P$	$\mathbf{7.5 \times 7.5 \times 2\,mm}$
Magnets material	NdFeB
Magnets size $l_M \times w_M \times h_M$	$\mathbf{2.5 \times 2.5 \times 2\,mm}$
Inter magnets distance d_M	0.5 mm
Micro-balls material	$\mathbf{Si_3N_4}$
Micro-ball diameter	1 mm
Micro-balls number per trench	4
Platform trench size $l_{PB} \times w_{PB} \times h_{PB}$	$5 \times 1.05 \times 0.5$ mm
Stator size $l_S \times w_S \times h_S$	$\mathbf{11.5 \times 7.5 \times 1\,mm}$
Column size $h_K \times \pi \times r_K^2$	$\mathbf{0.45 \times \pi \times 1^2\,mm}$
Inter columns distance d_K	500 µm
Micro-coil material	**Cu**
Micro-coil wire diameter $2r_W$	**25, 50 µm**
Number of Coil turns N	**12, 13**
Stator trench size $l_{SB} \times w_{SB} \times h_{SB}$	$5.5 \times 1.05 \times 0.45$ mm
Platform-stator air gap d_{PS}	50 µm
Platform total travel distance	2.5 mm

* Bold indicates the changed parameters.

Here the middle coil voltage has a negative sign, indicating that the coil is wound in the opposite direction with respect to the other coils to maintain additive positive induced voltage. The relationship between velocity v and B_{zt} is expressed as

$$\frac{dB_{zt}}{dt} = \frac{dB_{zt}}{dx}.\frac{dx}{dt} = \frac{dB_{zt}}{dx}\,v(t) \tag{3.13}$$

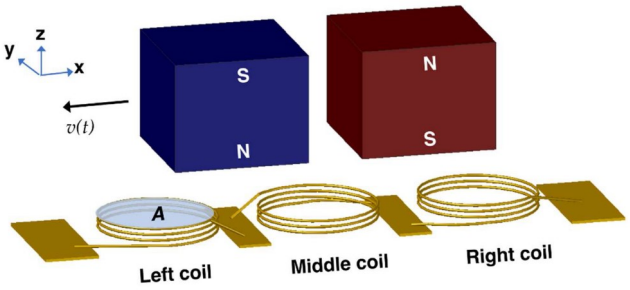

Figure 3.8: Schematic of the final design of coils showing the relative displacement of magnets along the x-axis.

The flux density at this stage can be estimated by finite elements analysis, when the platform is at the leftmost position, a maximum B_z on top surface is found to be 0.579 T and 0.342 T on bottom surface (figure 3.9). For such design, further simulations are performed by moving the platform with a step 100 µm and the total volume flux density for a single stator is calculated at every step, as shown in figure 3.10. It can be clearly seen that the total flux density is fit into a sinusoidal function with a 0.88 T peak. For two stators, equation 3.12 and equation 3.13 are combined to:

$$V_t(t) = 2.N.A\frac{dB_{zt}}{dx}v(t) = 2.N.A \times 0.88\frac{d\sin(400\pi x)}{dx}v(t) \tag{3.14}$$

The total resistance R_t and inductance L_t (according to [84]) for such coils

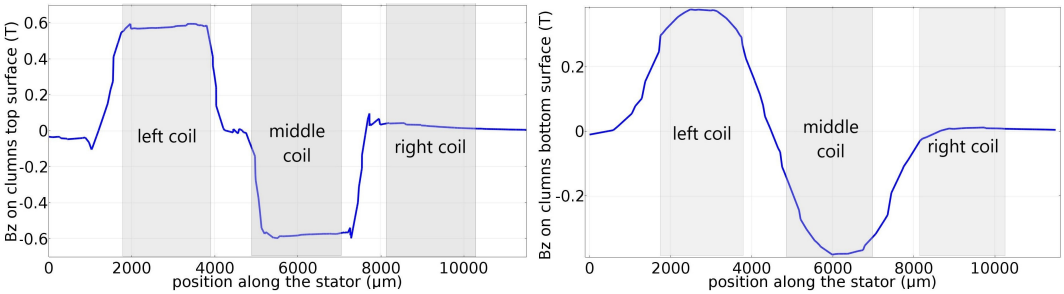

(a) (b)

Figure 3.9: Vertical magnetic flux density on a line passing on the top surface of columns (a), and bottom surface of columns (b).

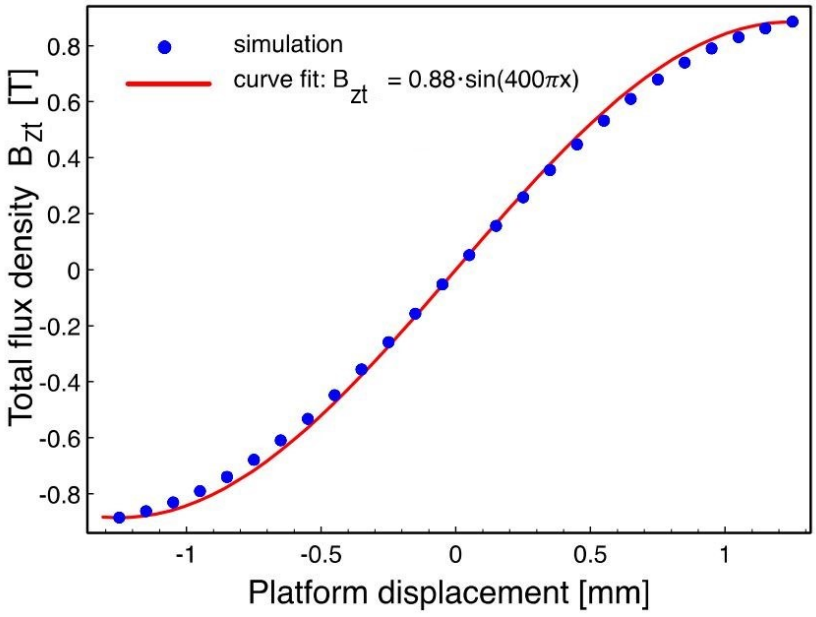

Figure 3.10: The variation of B_{zt} with respect to platform displacement. along the x-axis.

geometry will be:

$$R_t \approx 6\ \frac{\rho.N.(2\pi r)}{\pi r_W^2} \tag{3.15}$$

$$L_t \approx 6\ \frac{10.\pi.\mu_0.N^2.r_K^2}{9r_K + 10h_K} \tag{3.16}$$

Knowing that $x(t) = t.v(t)$, where v is the platform speed v, according to equation 3.14, the total induced voltage is:

$$V_t(t) = 2 \times N.\pi \times 10^{-6} \times 400\pi \times 0.88\cos(400\pi vt)v(t)\,\mathrm{V} \tag{3.17}$$

At speed of 1 m/s with $N = 13$ for example, $V_t = 0.0904\cos(400\pi t)$ V, this result shows that the generator can theoretically give a peak voltage of **90 mV** at a frequency of 200 Hz. According to equation 3.15, the total resistance for 25 µm and 50 µm wire thickness is **17 Ω** and **4 Ω**, respectively, and $L_t = 2.97 \times 10^{-6}$H from equation 3.16. Since the inductance here is negligible for low frequencies, the estimated RMS power is calculated using equation 3.4, that is **244 µW** for 50 µm thickness wire and **61 µW** for 25 µm.

Chapter 4

Harvester Fabrication and Initial Characterization

This chapter contains all details concerning the generator prototypes fabrication process including the used techniques and materials, from the first suggestion moving through the changes and improvements made at many levels to reach the final fabricated device, also the electrical characterization for the stator is presented.

4.1 Proposed Fabrication Flow

Because of its flexibility and bio-compatibility, PDMS is widely known in micro-fluidic channels fabrication and bio-implants [78,86,87]. Initially, a fabrication flow is suggested to produce the device prototype for the first design presented in section 3.1, as it is depicted in figure 4.1, two silicon wafers used as molds, one for the stator and another for the platform, are spin-coated with

photo-resist polymer, UV photo-lithography process than is performed to define the mask patterns on the wafers (figure 4.1a), after that deep reactive etching (DRIE) process is used to etch the Si wafer of the stator to a depth of 450 µm (figure 4.1b). The PDMS mixture is prepared and poured into the mold than hardened with heat as seen in (figure 4.1c) (details about making PDMS in section 4.2), after that, the PDMS stator is peeled off the mold (figure 4.1d) and Au is evaporated using a shadow mask to form the contact pads (figure 4.1e). Finally, 3D coils turns are made by wire bonder machine starting from a pad finishing in the other pad (figure 4.1f). The same steps in (figure 4.1a-d) with 500 µm DRIE are performed in order to produce the platforms. A hole device is assembled starting by adding a set of micro-balls to the bottom stator and magnets are embedded in the platform gaps. Then two platforms are put back-to-back and aligned with the micro-balls on the bottom stator. Another set of micro-balls is added on the top platform and a stator is flipped on the top of it. The two stators are then connected serially by soldering pad-to-pad short wire. The stators can be fixed to each other by gluing them to a PDMS thick package (figure 4.2a) and taking out two wires from the contact pads. The package is then cured with a thin PDMS layer to be fully sealed (figure 4.2b).

4.2 Pre-fabrication Experiments

The PDMS mixture is prepared from SYLGARD® 184 starting from two parts, the clear Si pre-polymer (part A) and the curing agent (part B) that is responsible for cross-linking and hardening. The ratio of A:B defines the flexibility of the final PDMS, the more curing agent the harder the PDMS will be. For our device structure, several Si pre-polymer samples are weighed and the curing agent is added to make 10:1, 3:1, 2:1, 1:1 and $^1/_2:1$ ratios (ordered from

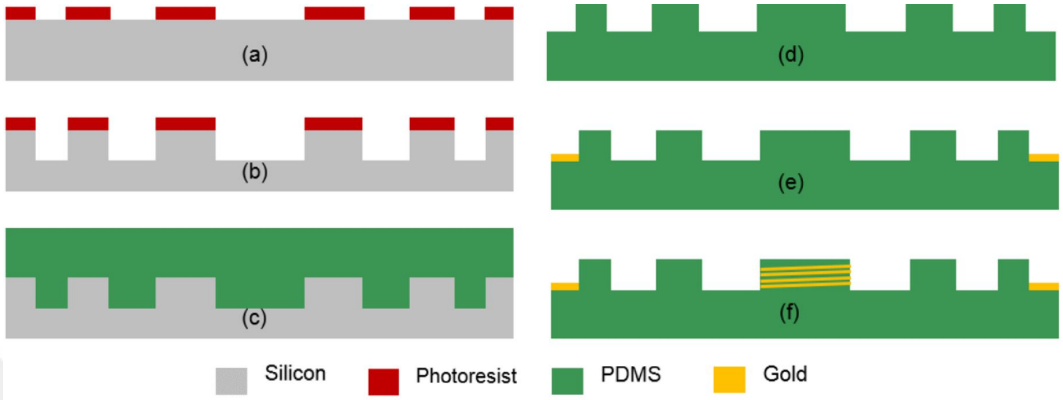

Figure 4.1: PDMS fabrication flow: spin coating of photo-resist on the Si wafer and UV exposure (a) than DRIE etching to form the patterns of the mold (b), PDMS mixture is poured on the mold than cured on hot plate (c), PDMS pattern is pealed from the mold and contact pads are defined (d-e), and the wire bonding of the micro-coils is performed (f).

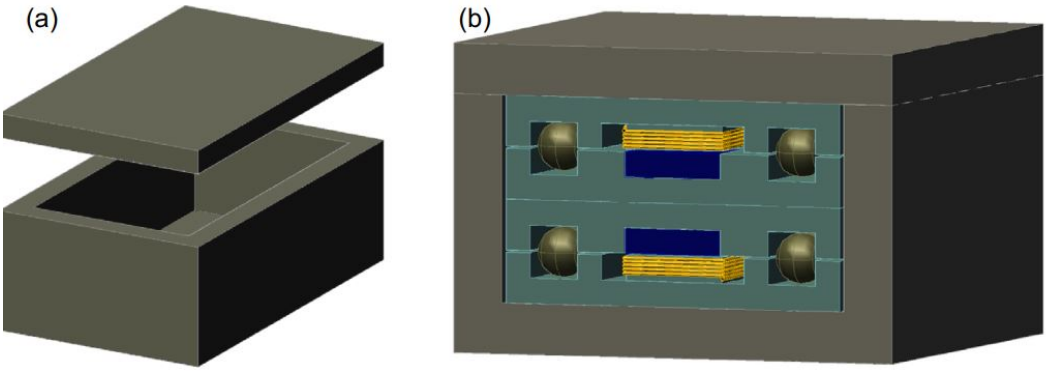

Figure 4.2: (a) PDMS packaging, (b) cut view of a packaged device.

the most to the least flexible). After mixing and degassing the solution, it is poured on molds and cured on hot plate at 70 °C for 2 h.

PDMS reviewed in the literature is mostly meant for microfluidic channels where PDMS flexibility of 10:1 ratio is enough. However, for patterns as in our case, a harder layer is needed. Even the hardest sample that is made from $^1/_2$:1 ratio (figure 4.3a) having the same 500 µm thickness as the stator shows a flexibility that is not suitable for making the stator and the structure is loose. This flexibility is inspected manually as seen in figure 4.3b because of lack of

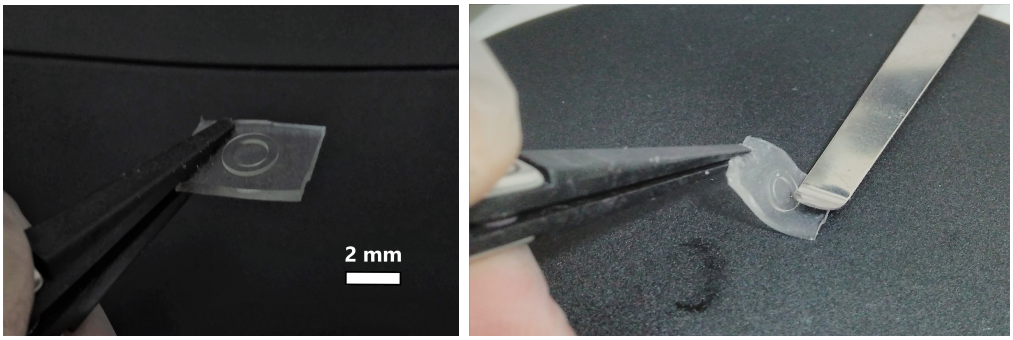

(a) (b)

Figure 4.3: PDMS experiments: (a) example of patterned ring shape on 0.5 mm thick base and (b) PDMS flexibility inspection.

mechanical characterization setup.

At this step, wire bonding trials by collaborators in KIT started in parallel, all the steps concerning wire bonding process can be found in details in appendix A, it was concluded that it is very important that the stator does not deform at the first step of wire bonding. At the beginning, the substrate is heated up to 80 °C and the application of the force on the Au pad to make wire connection causes stress on the substrate and the physical coordinates of the winding starting point change. Also, during micro-coil winding, the stress of the wire on the flexible posts deforms their shape, and the winding stability fails. For these reasons, it is decided for the next step to try harder materials such as thermoplastics which are more rigid having Young's modulus (E_m) in the order of 740 MPa and are temperature-resistant [88].

4.3 Thermo-plastic Prototype

A 3D printed thermoplastic stator and platform of the updated design (section 3.3) are shown in figure 4.4. As it can be seen, one of the important problems

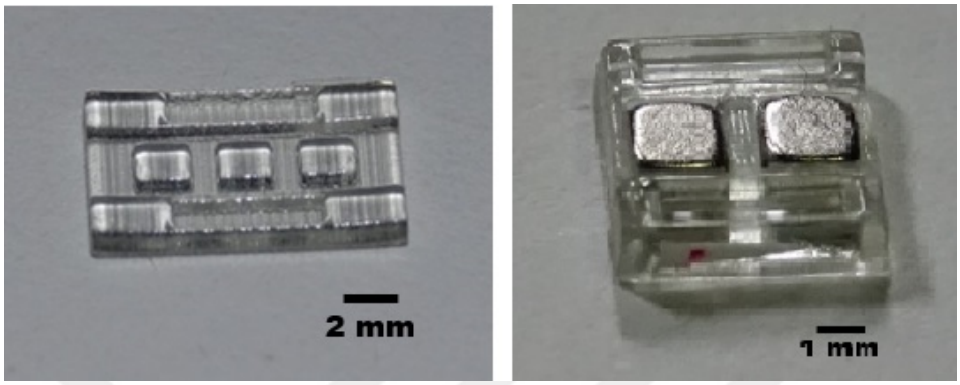

Figure 4.4: A prototype of thermoplastic 3D printed stator (left), and platform with magnets embedded (right).

of the stator is a slight obliqueness, this is not observed in the platform because it is relatively short and bulk. This inclination is a major obstacle to the movement of the platform. In addition, an experimental setup is implemented as shown in figure 4.5 to analyze the device motion, the device is fixed to the OS-3000 open-air shaker, the platform and lower stator are labeled for position tracking and the motion is captured with high frame rate (HFR) camera at 960 fps, the data than is processed in Kinovea, a software for kinematics analysis (figure 4.6), subsequently, data analysis is repeated for several shaker frequencies ranging from 1.67 Hz up to 4.67 Hz without observing any platform relative motion as expected from theory, after that, the trenches are inspected under the microscope and a roughness on the material surface is observed, this roughness is responsible for high friction that prevents the plastic micro-balls from rolling.

In the first design, the purpose of selecting a flexible material is to allow the device to flex with the tissue when implanted in the body in order not to damage the tissue. However, when we look at other bio-implants currently in use, it is seen that most of them are made of hard materials with few hundreds GPa Young's modulus [18] as titanium (Ti), titanium nitride (TiN), nickel titanium (NiTi), epoxy ($C_{21}H_{25}ClO_5$), ceramics...etc., and the package shape is

designed with round sharp-less edges to prevent damaging the surrounding tissues. More details about these commercial devices are presented in appendix B.

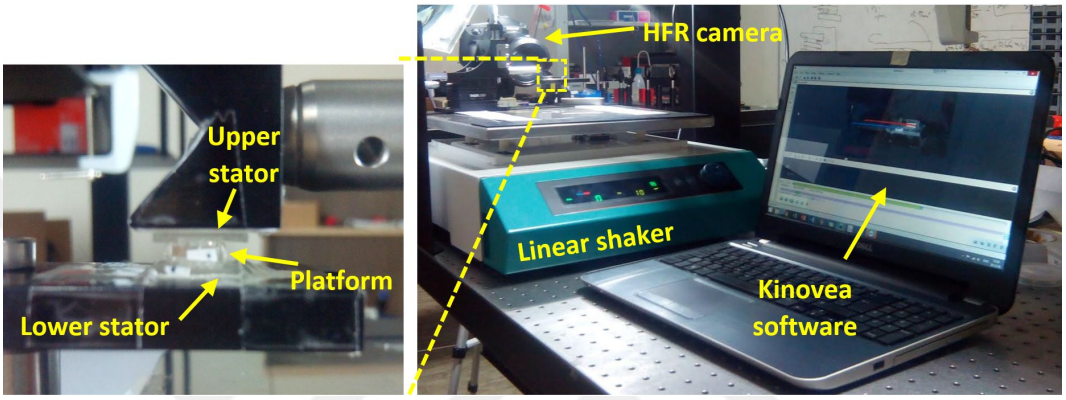

Figure 4.5: Thermoplastic device kinetics experimental setup (right) and a close-up view of the device (left).

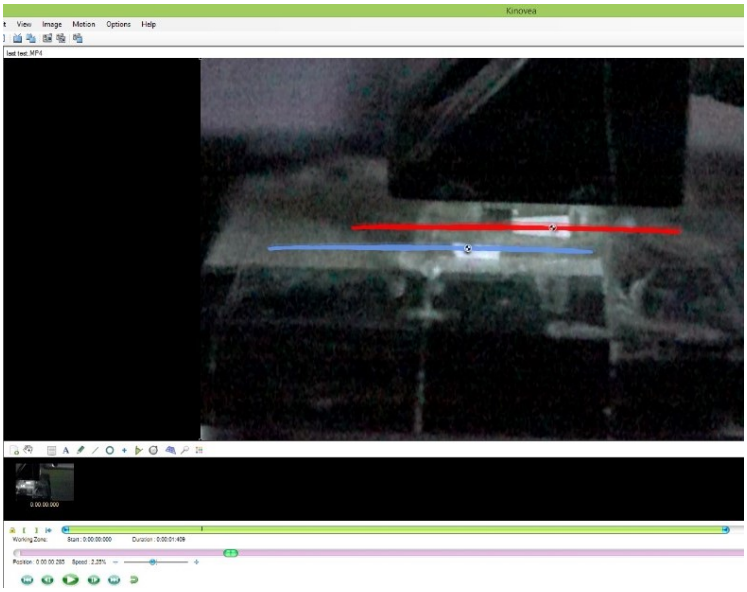

Figure 4.6: Kinovea displacement analysis of the stator (blue) and platform (red).

4.4 Stator Micro-fabrication with DRIEed Si

After the thermoplastic stator problems, it was decided to be micro-machined with Si substrate that is relatively harder with E_m above 160 GPa [89]. Because the 2 mm thickness of the platform is relatively big, it is not suitable to be produced by micro-fabrication. For this reason, it is made using Computer Numerical Control (CNC) machine with 500 µm tolerance and the material chosen for this is aluminum with $E_m = 69\,\text{GPa}$ (figure 4.7). It is obvious that the mechanical parts in contact should have stiffness nearly in the same range, so the plastic micro-balls are replaced by silicon nitride ones (Si_3N_4) that are relatively stiffer ($E_m = 310\,\text{GPa}$) [90].

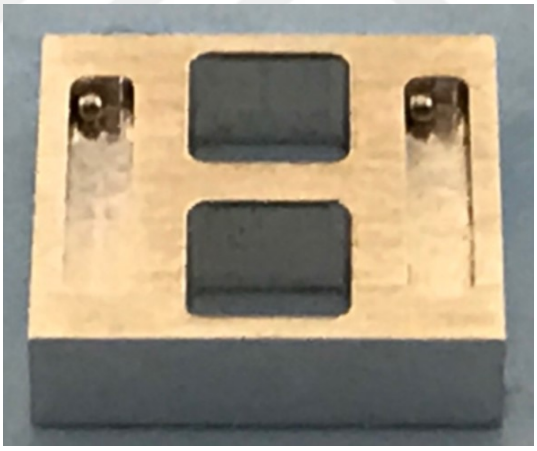

Figure 4.7: CNC machined aluminium platform

This change of materials necessitates a change in stator production techniques. The developed fabrication flow is shown in figure 4.8 (the detailed recipe is revealed in section C.1). First of all, 1.4 mm thick silicon wafer with 2 µm oxide coated with photoresist is treated with photo-lithography to determine the patterns of side trenches and coil columns (figure 4.8a). Next, oxide wet etching and DRIE are performed to etch the trenches and coil columns to

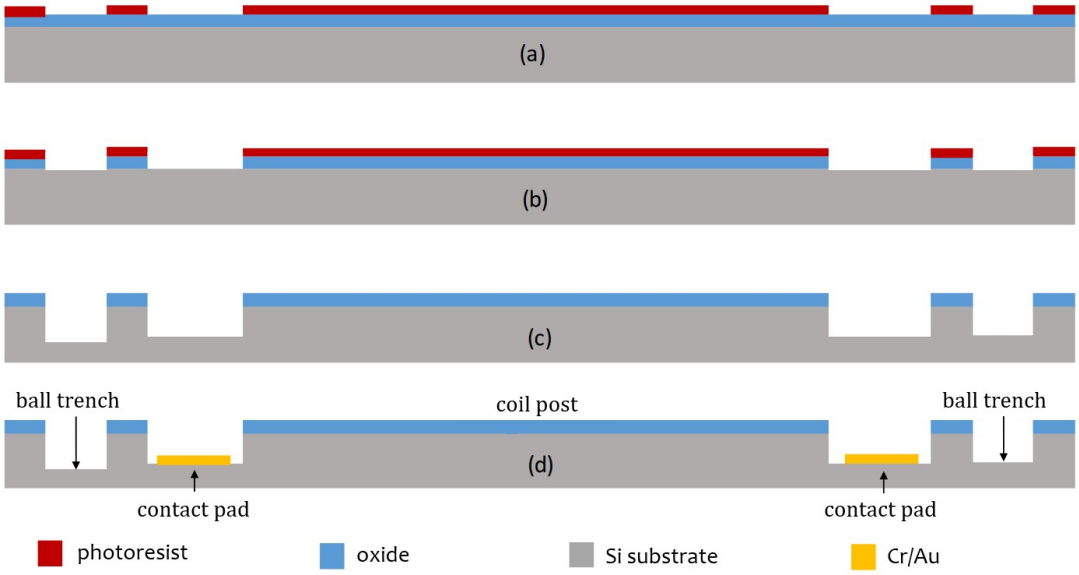

Figure 4.8: Stator fabrication flow using DRIE technique on Si substrate

a depth of 475 µm (figure 4.8b-c). The whole chip is coated again with oxide by thermal evaporation technique and 50 nm chromium and 150 nm gold layers are formed with sputtering technique respectively. Lastly, lithography and wet etching processes are used to determine the Cr/Au contact pads and the production of the stator is completed (figure 4.8d). The wafer was produced in UNAM-Bilkent University, it contains 28 stator prototypes as shown in figure 4.9a.

The wafer was partially diced (75%) prior to wire bonding trials and cleaned, so it will be easy for separating the stators ships after winding phase by gently pressing the wafer to be cracked straight thanks to silicon crystal structure. After winding the coils, dicing is not doable because it is a coarse and dusty process and could easily damage the coils wires. A single stator after dicing before winding is shown in the zoomed view (b). It is observed that some gold traces on the posts and inside the trenches are not etched away. This is due to the uncleanable photoresist from these points that forms a protective film layer during the wet etching process. The winding wire is insulated and the pads

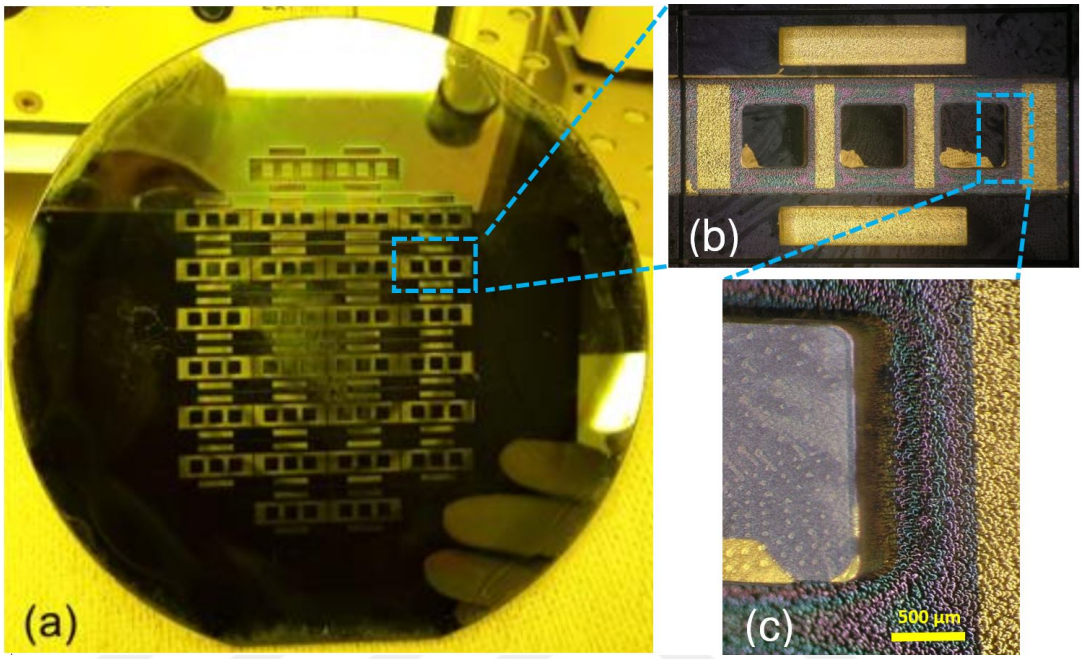

Figure 4.9: (a) micro-fabricated stators on 4" Si substrate, (b) a zoomed view of a single stator and (c) a zoom on the stator bottom showing pad roughness.

are checked by electrical conductivity test showing that they are not shorted, so these traces are not causing a problem for power generation. Finally, the coil winding process was started.

As a result of several trials, it was observed that the coil was braking immediately after the capillary contacts the pad for wire bonding (figure A.2c). In order to find the cause of this condition, the pads were inspected under the microscope and a rough surface is clearly observed as shown in the close-up view in figure 4.9c. For further investigation, the pads were scanned under the optical profilometer and the pads roughness is measured one of the samples is displayed in figure 4.10 measuring a roughness of 13.52 µm. This roughness is the result of DRIE process and it has been understood that the 150 nm gold layer above this roughness was comparatively too thin to perform ball bonding step. After discussions with Dr. Badilita and the graduate students working in IMT cleanroom, it was concluded that the available wire bonder with its

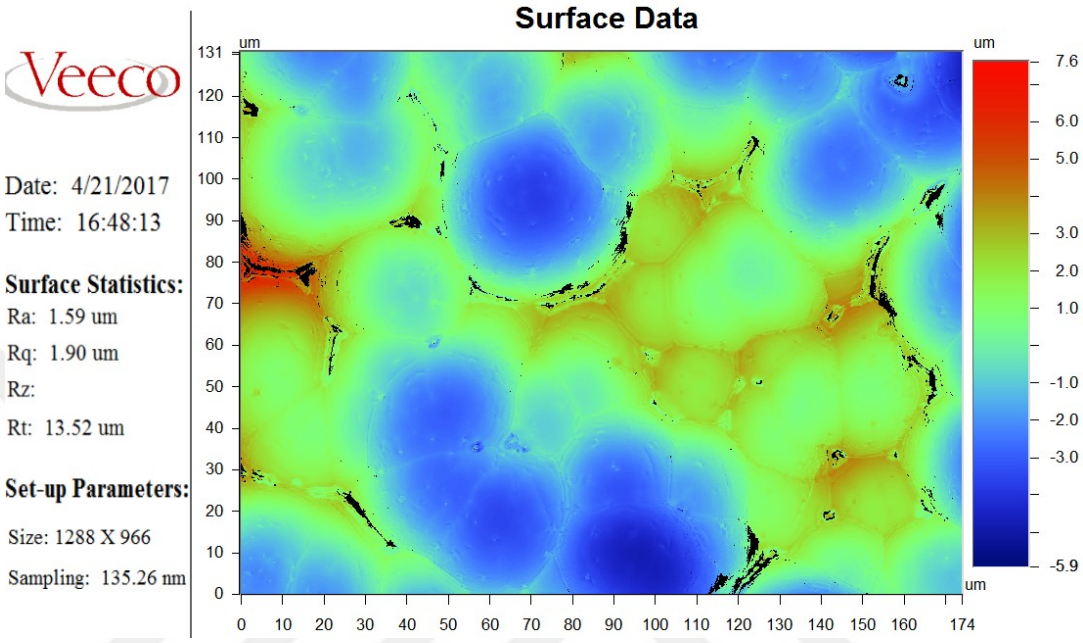

Figure 4.10: Surface roughness measurements of Au contact pads by optical profilometer.

50 µm wire requires pads to be much thicker for a successful and strong wire bonding, and this can be done with Au electroplating instead of thermal evaporation.

Electroplating on the same wafer at that moment was difficult given that the pads are deep in the wafer which makes the process challenging, on the other hand, starting over the same plan is not possible for the time limitation to access facilities. Alternately, it was decided to start the fabrication with the SU-8 structure on the Pyrex chip, which Dr. Badilita and his group used frequently before.

4.5 Stator on Pyrex Glass Substrate

The alternative fabrication flow followed is summarized in figure 4.11 (for more details, refer to the recipe in section C.2). The fabrication was started on 4”

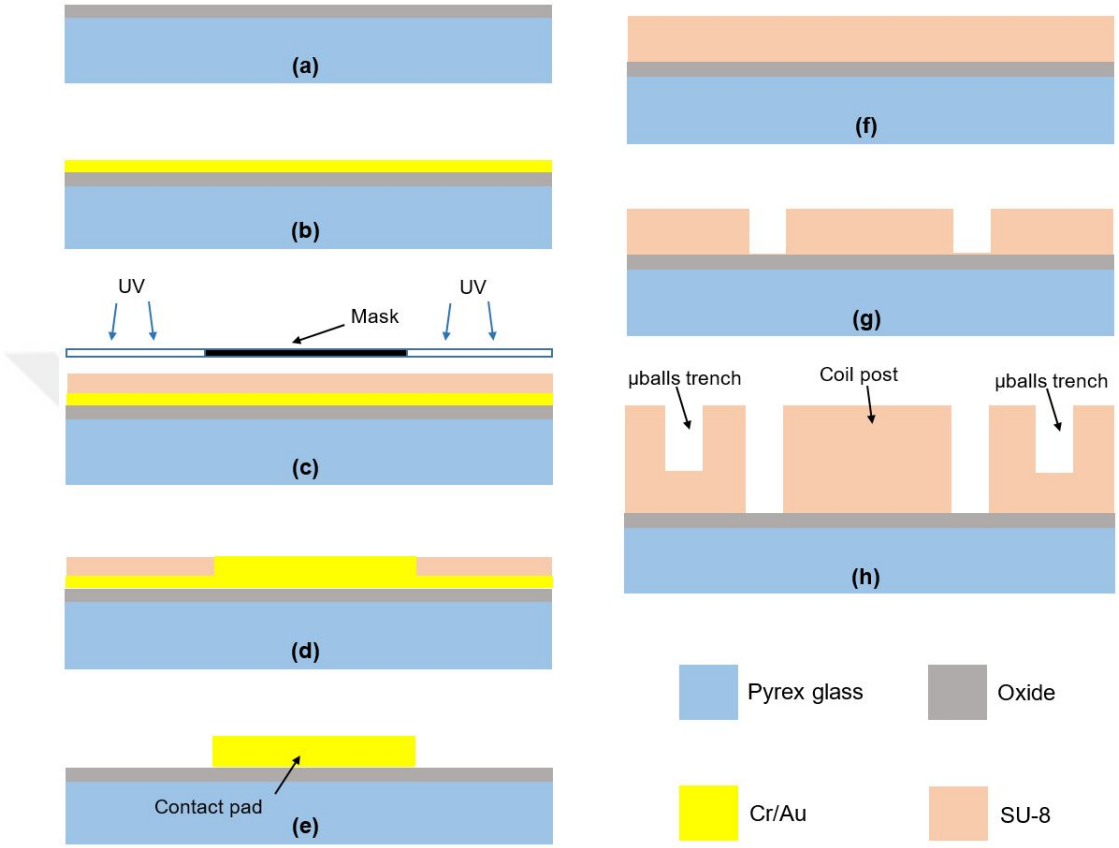

Figure 4.11: Stator fabrication flow based on Pyrex glass substrate.

Pyrex glass substrate of 500 µm thickness with 1 µm oxide layer to enhance bonding (figure 4.11a). A layer of 10 nm Cr and 50 nm Au were sputtered to form the seed layer for electroplating (figure 4.11b). Next, the wafer was coated with 25 µm thick SU-8 photo-resist, pre-baked and exposed to UV through the mask than developed to form the Au pads openings (figure 4.11c). Gold then was electroplated and photo-resist was stripped and the seed layer was etched (figure 4.11d-e). The electroplated contact pads have 5 µm thickness, which is enough for strong wire bonding. A 350 µm layer of SU-8 is applied (figure 4.11f), and exposed to UV light then developed to form the first layer of the stator (figure 4.11g). The same process is repeated with 400 µm photo-resist to form the trenches and the second layer of coil post (figure 4.11h), using

SU-8 instead of DRIE was advantageous to set the trench depth and the coils height independently. Figure 4.12a presents a zoomed view of the produced wafer showing four stators after partial dicing. The first successful winding

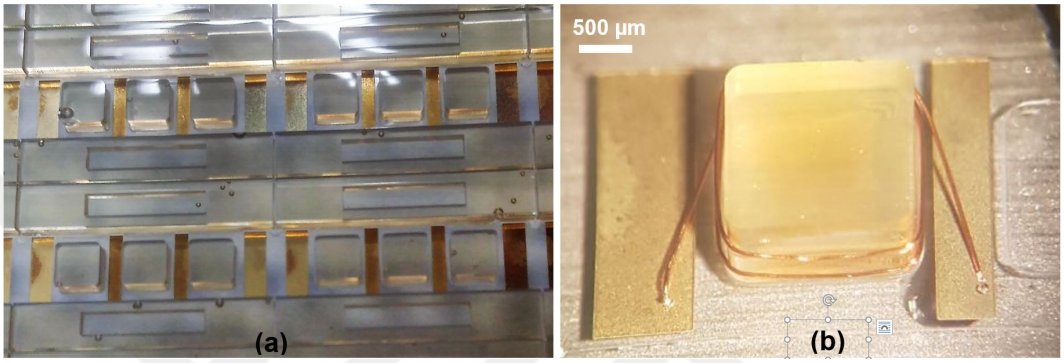

Figure 4.12: A zoomed view of the stators produced on Pyrex substrate (a), and a successful two turns coil made on square post (b).

experiment on a single post completed a coil with two turns as shown in figure 4.12b. However, during coil winding, it was observed that the corners of square columns cause wire breakage very often, or column deformity when the capillary is moving. In fact, it disrupts the reproducibility of the coils for more successful prototypes. For this reason, the stator design was updated to the geometry mentioned in section 3.4 where the coil post is cylindrical with a diameter of 2 mm. After this change, the same fabrication flow with updated photo-masks was performed and the coils could be produced without any problems. An example of a stator with 14 turns per coil is shown in figure 4.13.

The target number of turns in the initial stage of the project was set at 100. It was foreseen that the same column could be achieved by winding the wire up and down more than once, experiments results showed that the number of windings is limited by the number of coordinates. In order for each winding to be mechanically risk-free, at least 3 coordinates must be entered (figure A.3), and this yields 300 coordinates for 100 turns. This number has been seen to exceed the capacity of the wire bonding device. Using more points to produce fine cylinder shape has limited the number of turns for our column geometry

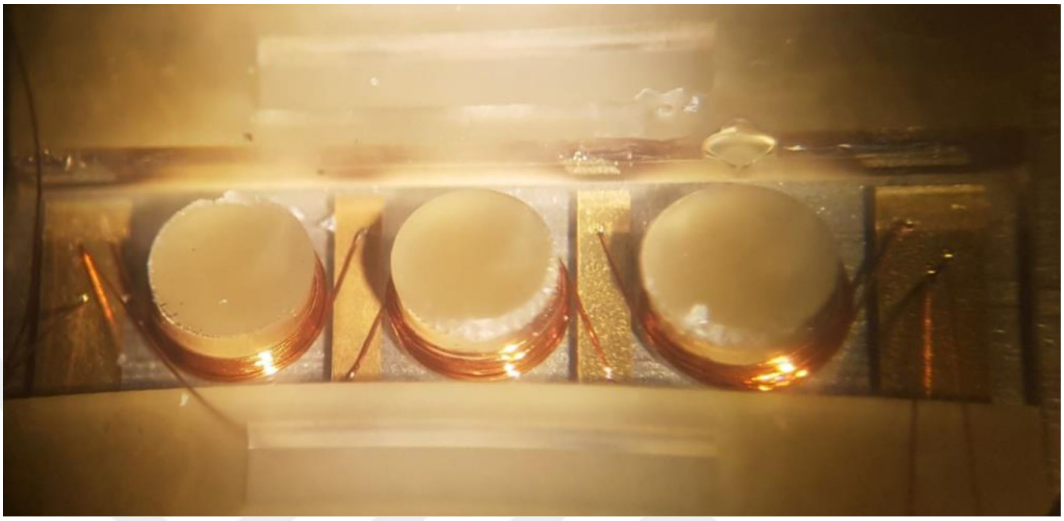

Figure 4.13: A sample of stator with 14 turns per coil on cylindrical posts.

to a maximum of 14 for 50 µm wire thickness, taking into account the warnings of the device's risk of deterioration. Prospective solutions for increasing the number of windings are described for future work in chapter 6. Coils production from copper was a necessity because the same institution used copper wire instead of gold during the project. Since copper resistivity is lower than gold, this change has been seen advantageous in the context of device performance.

After finishing winding, some of SU-8 layers detach from the Pyrex substrate after it cools down. It is understood that the reason for this is the great difference between the temperature extension coefficients of the Pyrex substrate and the SU-8 polymer, and that this difference leads to weak adhesion between the two materials, some unbroken stators that pass to voltage tests, do not withstand repetitive vibrations sometimes that causes the coil columns to break off from the substrate. For this reason, it is finally decided to use a silicon substrate which has reported to have stronger adhesion with SU-8 compared to Pyrex [83].

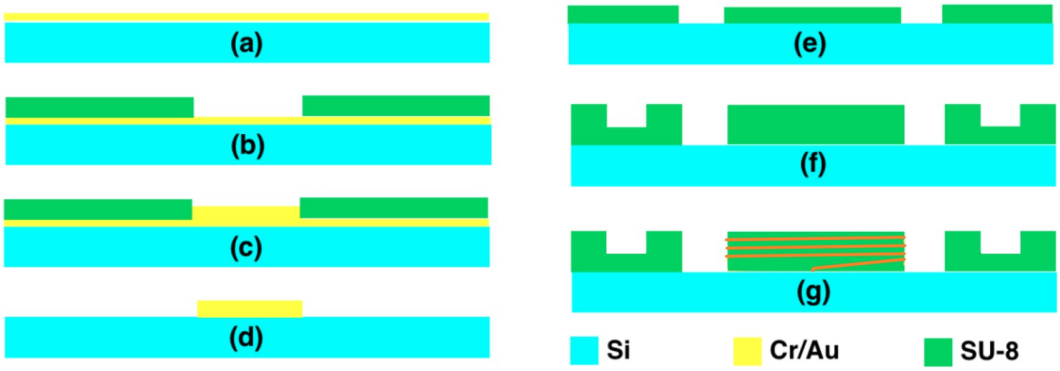

Figure 4.14: Fabrication flow of the stators using Si substrate: coating with Cr/Au seed layer(a) and pads pattern creation and electroplating (b-c), then, development and seed layer etching (d). The SU-8 layers patterning to form columns and trenches (e-f) and coil winding with copper (g).

4.6 Stators on Silicon Substrate

The fabrication flow to produce the final prototypes is illustrated in figure 4.14, a detailed recipe is presented in section C.3. Starting with 4" silicon wafer with 500 µm thickness, it was coated with a seed layer of 20 nm chromium and 60 nm gold respectively (figure 4.14a). The surface was coated with 25 µm SU-8, patterned with UV exposure and developed to form the pads openings (figure 4.14b). In the next step, the gold was electroplated (figure 4.14c) and the seed layer was etched away resulting 5 µm thick contact pads (figure 4.14d). In order to increase the adhesion of columns and trenches to the substrate, a 25 µm adhesion layer of SU-8 was added to the wafer and exposed to UV light (figure 4.14e), then, an additional 450 µm thick layer is patterned to form the trenches and columns layers (figure 4.14f). Finally, the wafer was partially diced and underwent the winding process using 25 µm copper wire, polyurethane droplets were added to fix the windings and to prevent the wire from leaving the post when the stator experiences vibration during tests (figure 4.14g).

It was not possible to use 50 µm wire in this stage and was changed with

conformity to the wire bonder regulations, changing the wire type requires several modifications in the machine settings for about seven days of wire bonding tests before it starts working properly, and this affects other projects that were using the machine at that time. A package of Poly-Lactic Acid (PLA), a biocompatible material [91] was fabricated using 3D printer to tighten the device parts for the tests. The package is made with side openings in this stage to observe the platform motion in the tests. A view of the packaged device is shown in figure 4.16.

4.7 Stator Initial Characterization

The purpose of these measurements is to determine the resistance R_s, capacitance C_s and inductance L_s values of the stator coils as shown in figure 4.17. For a stator made with 14 turns of 50 µm copper, L_s, R_s and C_s of the three coils is measured to be in the range 378-423 nH, 2.6 Ω and 10.4 pF, respectively. for the silicon stators where the coils are of 25 µm copper wire with 13 turns the total device resistance was measured 20 Ω. As assumed in the theoretical calculations, the measured inductance value is negligible, and the measured resistances are near to the theoretical values in section 3.4.

The schematic circuit shown in figure 4.18 was implemented to show the

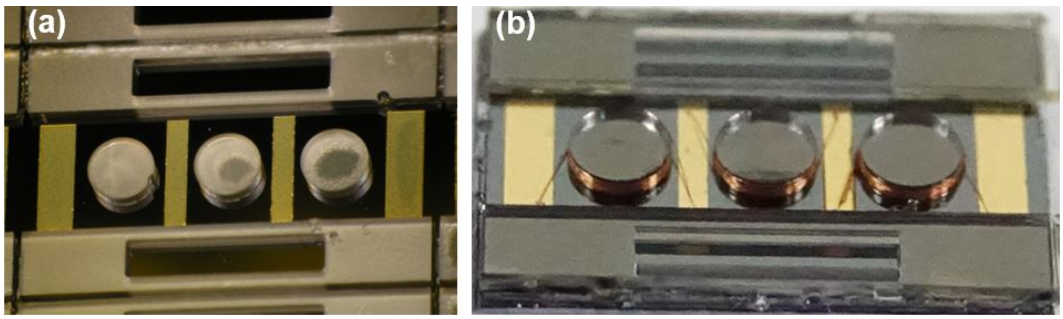

Figure 4.15: A zoomed view on the Si wafer showing a stator after partial dicing (a), and a single stator wound with 13 turns per coil (b).

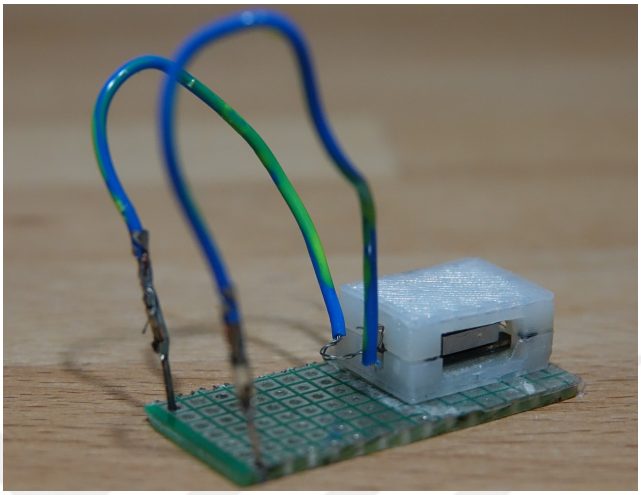

Figure 4.16: The whole harvester packaged in PLA, an opening from the side to observe the platform in tests, and from the front for connection wires.

response of the stator at high frequencies, the resistance $R1$ has the same resistance as the stator was connected in series and an AC signal was applied with different frequencies, the oscilloscope was connected to display the stator and $R1$ voltages.

Two examples of applied signals at frequencies 1 KHz and 250 MHz are shown in figure 4.19, comparing the voltage of $R1$ (in blue) and the stator voltage (yellow) showed that the two voltages are in phase at 1 KHz (top), as the excitation frequency was increased to 40 MHz, the phase difference becomes observable (bottom), which is far above the voltage generated by the harvester from daily human being activities.

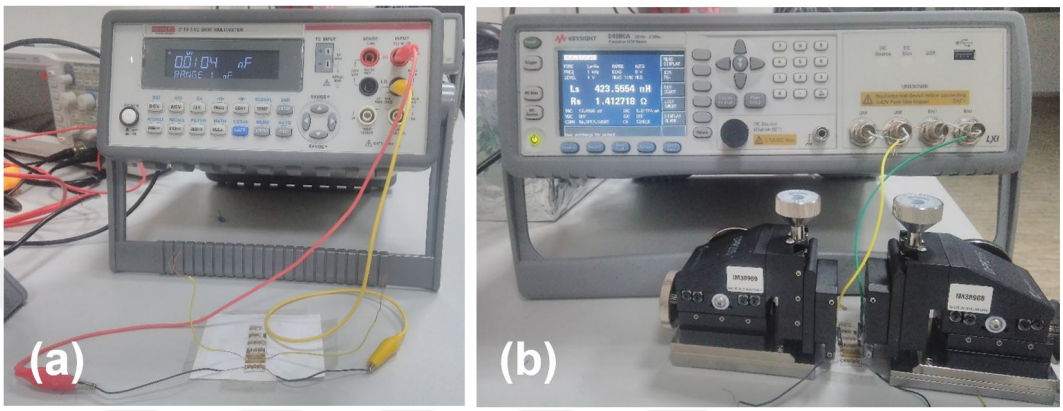

Figure 4.17: Stator characterization setup: (a) capacitance measurement, and (b) inductance and resistance measurement (values shown here are for 7 turns sample).

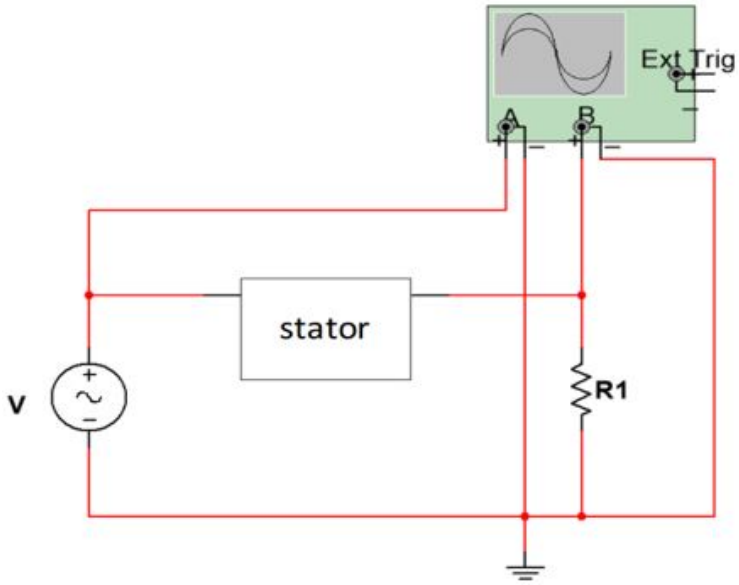

Figure 4.18: Stator high frequency response circuit.

Figure 4.19: Stator voltage in yellow and $R1$ voltage in blue on the oscilloscope when applying a source signal at 1 KHz (top) and 40 MHz (bottom).

Chapter 5

Harvester Testing, Results & Discussion

This chapter is about kinetic tests of the platform to determine friction force, and voltage and power delivery tests of the generator. The device was tested on a linear shaker for different frequencies than tested on a wristband for some daily activities. Performance results are detailed and discussed here.

5.1 Device Motion tests

This test, was performed to determine the platform relative displacement and to extract its velocity than acceleration and friction force calculation. Test setup used for this was the same as shown in figure 4.5. Here, a single stator was fixed on the shaker, then, micro-balls and platform were placed in order. When the shaker moves forward and backward, together with the stator, the platform stays relatively constant in reference to the ground, creating a relative

motion between the platform and the stator. The peak-to-peak amplitude of vibration is limited by the shaker to 2 cm, while the frequency is adjustable. The platform response was observed at 2.67 Hz (160 rpm). This motion has been recorded with the HFR camera, and analyzed using Kinovea (figure 4.6).

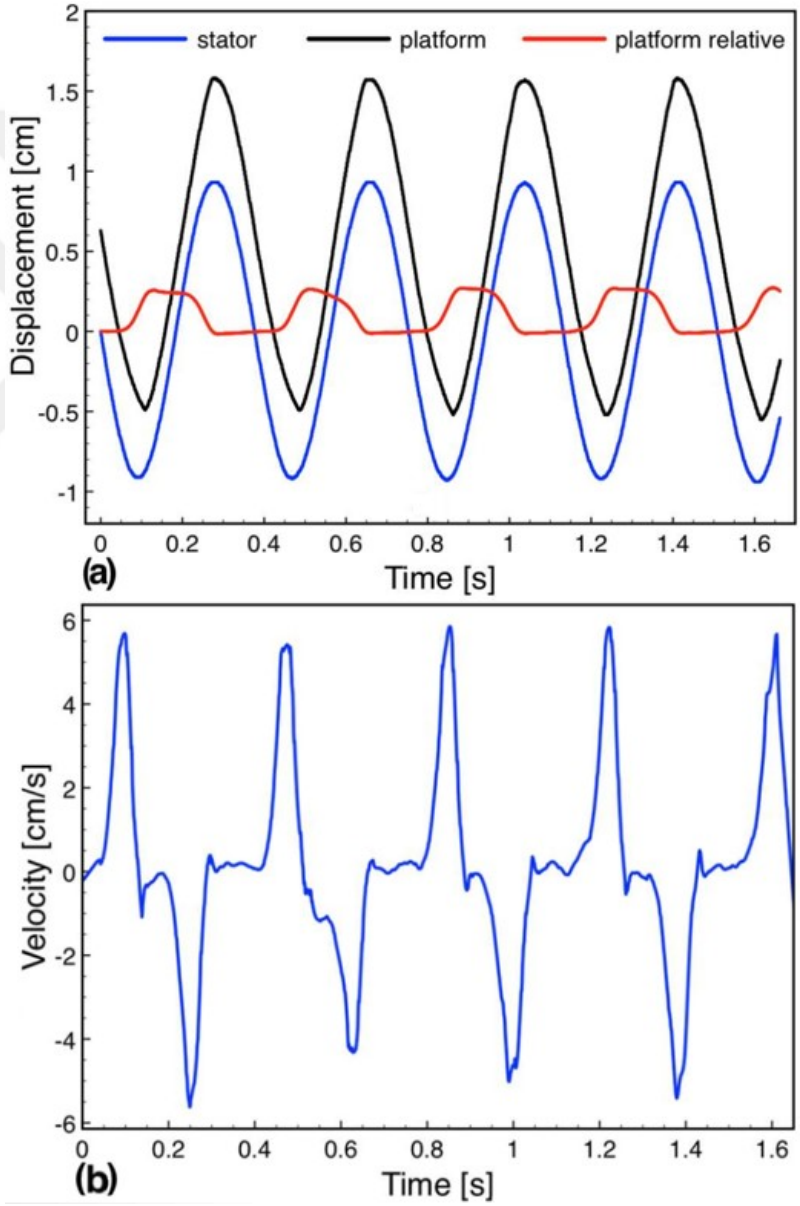

Figure 5.1: Kinetic tests for a single stator: (a) displacement of stator, platform and relative displacement vs. time, and (b) platform relative speed vs. time.

The graph in figure 5.1a shows the displacement of the stator in blue and for the platform in black, both have a total displacement of 2 cm. The difference of the two components gives the relative platform displacement sketched in red It is clear that the total relative displacement is about 2.5 mm, that is exactly the same as the value from theory mentioned in section 3.1.

The platform movement happened at the ends of motion i.e when motion direction of the stator was changed. The platform remains almost in stationary in the middle, this due to the fact that the 2 cm shaker fixed amplitude was large and could not be decreased. The same remark can be seen in the platform relative velocity numerically derived from displacement shown in figure 5.1b, where the velocity picks happened in the edges. The maximum platform relative velocity was found to be 5.8 cm/s.

Deceleration of the platform a_p is caused by the friction force f_f. For platform mass M_p, the friction is $f_f = M_p.a_p$. From the velocity graph (figure 5.1b), $a_p = 1.7\text{m/s}^2$ and M_p is measured on precision scale 0.35 g, hence friction of the platform with one stator is 0.595×10^{-3}N, that is approximately 1.2 mN for two stators. This can be understood as the minimum force to be applied to the device in order for the platform to move and voltage generation occurs.

5.2 Voltage & Power Generation Test Setup

In this tests as shown in figure 5.2, the HFR camera was used, as before, to observe the platform displacement. On the shaker, the device was placed and its terminals were wired to analog inputs of DAQ data acquisition card from National Instruments™. The DAQ card was connected to LabVIEW software with data sampling rate set to 400 KHz to analyze, display and save -in real time- the acquired voltage signal and its spectrum (top right and left graphs

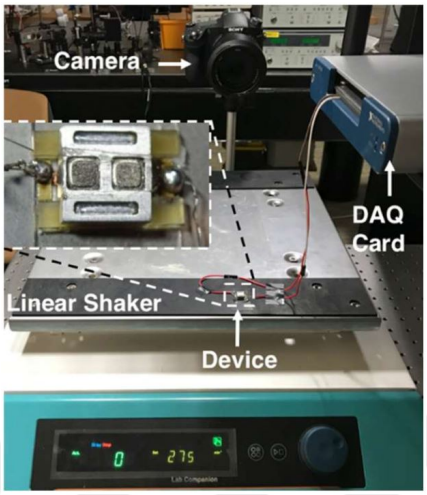

Figure 5.2: Stator characterization setup: (a) capacitance measurements, and (b) inductance and resistance measurements (values shown here are for 7 turns sample).

respectively shown in figure 5.3). The DAQ card was tested with a signal generator beforehand and showed high sensitivity and accuracy which is good to measure small voltages down to few mVs as shown in the figure. That is why it is chosen for micro-generator testing.

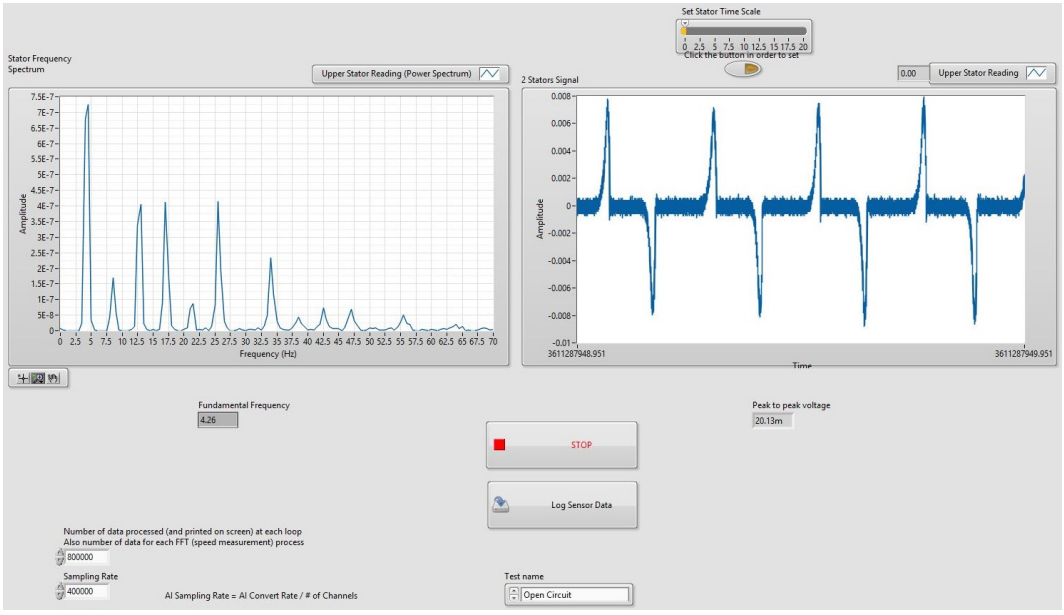

Figure 5.3: Test setup used for collecting harvester voltage and power data.

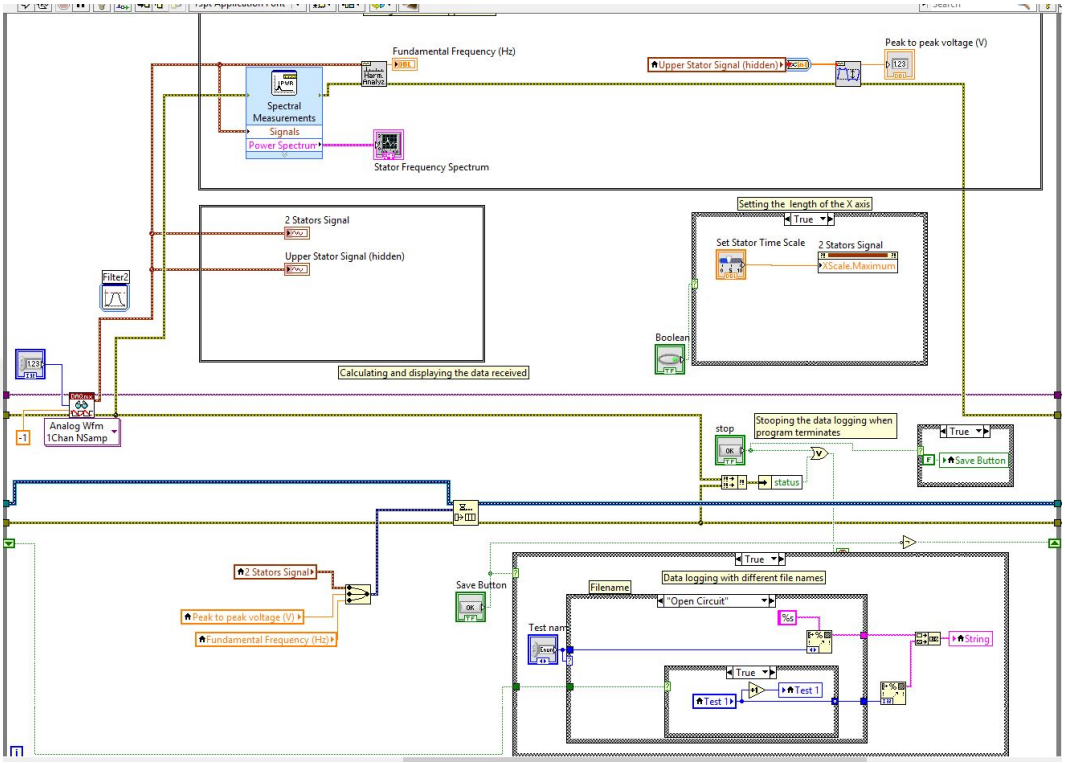

Figure 5.4: Part of the developed block diagram of LabVIEW showing the consumer loop for voltage and spectrum analysis.

The developed LabVIEW program with block diagrams contains mainly two consumer loops. The first one includes a part for voltage signal acquisition and display and another part to calculate fast Fourier transform (FFT) and display the frequency spectrum as shown in figure 5.4. The other consumer loop is for data logging (not shown in the figure) which is responsible for saving collected numerical data into files.

5.3 Open Circuit Voltage Tests

The shaker frequency was gradually increased from zero and reached 160 rpm (2.67 Hz). At this frequency, the first open circuit voltage signal (V_{oc}) was

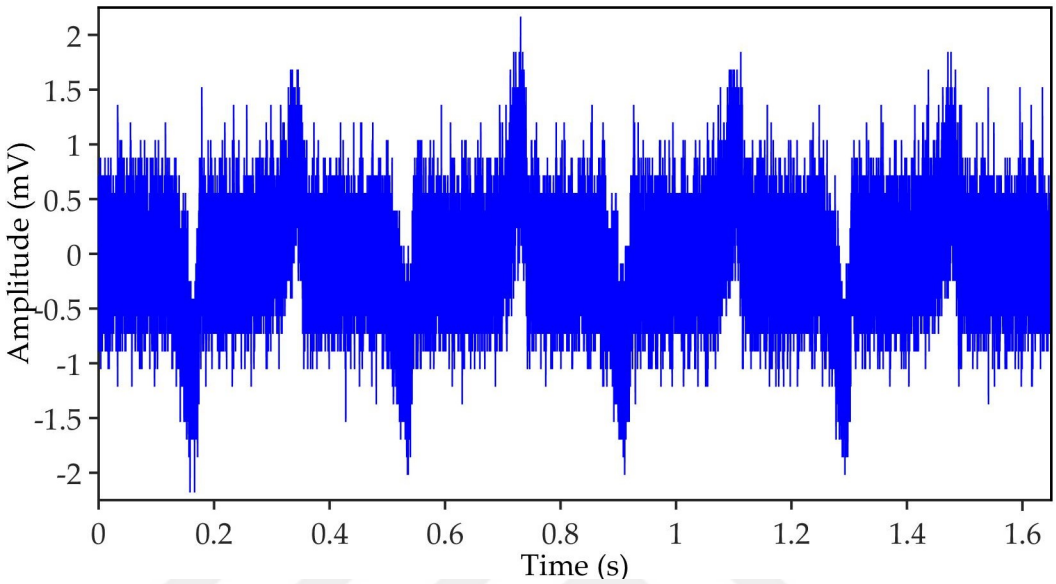

Figure 5.5: The first V_{oc} signal recorded by LabVIEW at 2.67 Hz frequency.

obtained from a single stator. V_{oc} waveform recorded by LabVIEW from is shown in figure 5.5. It is clear that the signal has ripples of noise and this is caused by surrounding higher frequency signals that interfere with the stator signal as seen in top graph in figure 5.6. Since the generator voltage is in low frequency range with first harmonic at 2.67 Hz, the recorded signal data was entered to MATLAB for filtering and all frequencies above 50 Hz (main power line frequency) were eliminated. The filtered voltage signal is shown in the bottom graph in figure 5.6. The results show that the peak open circuit voltage induced by a single stator of 12 turns per coil is 1.05 mV (2.1 mV for two stators) at 2.67 Hz frequency. The voltage waveform behaves like short pulses rather than sinusoidal. This agrees with velocity results discussed in section 5.1 since voltage generation happens when velocity changes at the edges of device motion. This voltage is around 43% of 4.84 mV, the value calculated using equation 3.17. These initial results were published in [67].

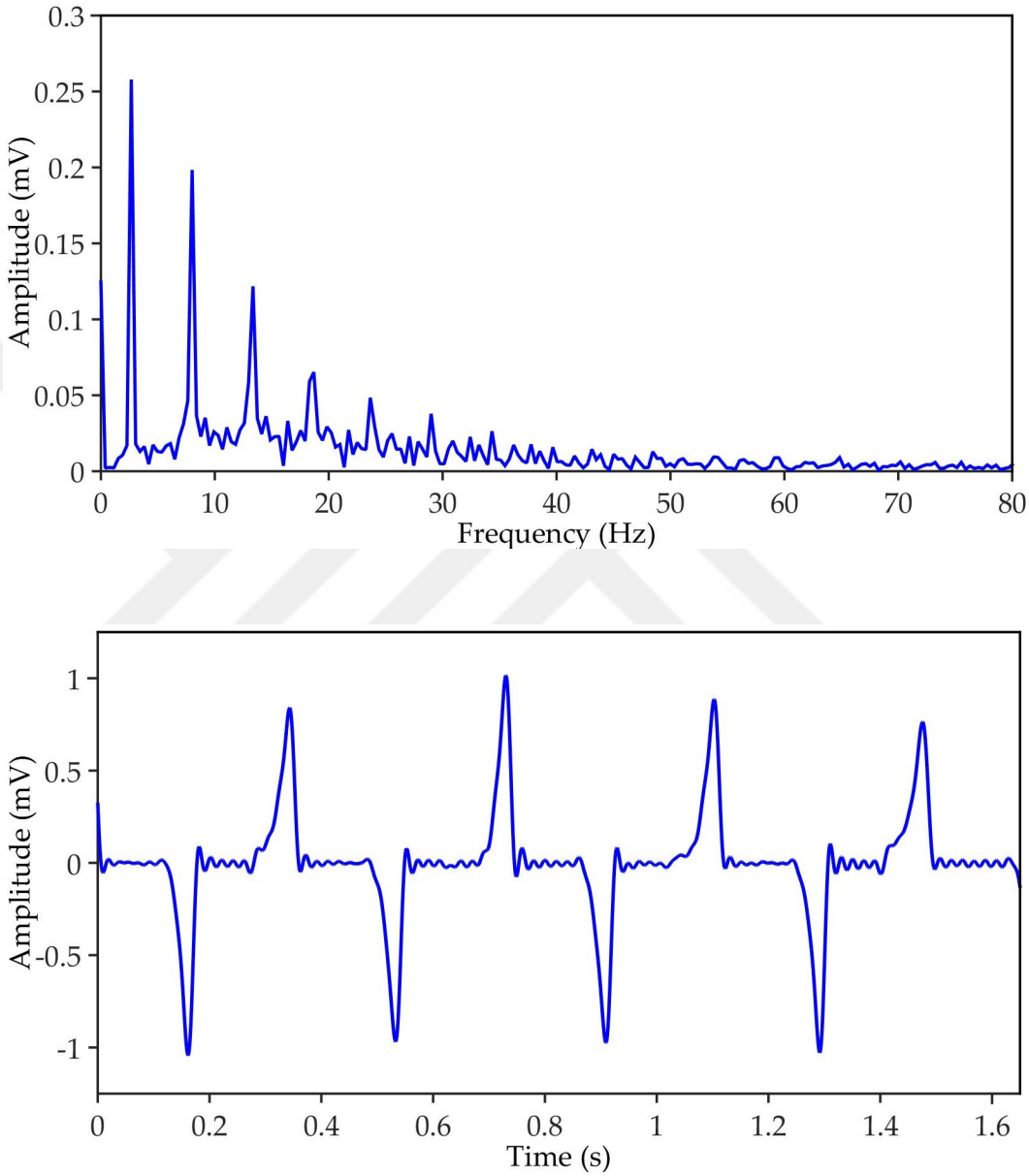

Figure 5.6: OC voltage spectrum with a 2.67 Hz fundamental frequency (top) and the OC voltage after filtering out noise above 50 Hz.

There are couple of reasons for such difference. The wire bonder starts winding at 100 µm height above the column base, also the last turns height was kept below the column height for the sake of mechanical stability (clearly seen in

figure 4.13). This makes the effective coil height less than the column, hence, the flux density through the micro-coil volume is less. In addition, this micro-coils height makes the actual distance to platform surface d_{PS} bigger than the 50 µm determined in device design stage. This measured to be about 200 µm, this implies that magnetic flux density on coils surface is less. Another reason for such discrepancy would be the magnets magnetization that decreases near the magnets edges leading to a weak magnetization in the boundaries. As a result, the average magnetic flux density through the coils decreases.

The above results were obtained from the Pyrex glass sample, that did not withstand shaking tests due to the structure adhesion issues mentioned in section 4.5. The only successful test was for a single frequency, also, cleaving the wafer to separate stators was not easy due to glass crystal structure and the cracks dispersed roughly destroying structures. This is the reason why these voltage results are for a single device. In addition to strong adhesion fulfilled after moving to silicon substrate plan, the crystal structure of silicon was advantageous for separating stators. Two stators were connected in series and a full device was assembled with PLA package as shown in figure 4.16. This stable structure offered a wide range of voltage and power tests with more frequencies. In figure 5.7, an example of the packaged device open circuit voltage with the shaker actuation frequency set to 5.67 Hz. At this frequency, the generator was able to induce 12.55 mV peak-to-peak voltage. In order to observe the voltage generation with respect to the actuation frequency, the shaker frequency was increased gradually, and voltage data was collected at each step. The produced peak voltage at each frequency is shown in figure 5.8. Here, it is observed that the peak voltage and actuation frequency relationship is linear using a fitted regression line with R^2=0.9941. The maximum open circuit voltage amplitude obtained on shaker test is 6.25 mV when the device is moving at 5.83 Hz. Experiments were not performed at frequencies higher than 5.83 Hz, as it was observed that the device was not fully stationary when

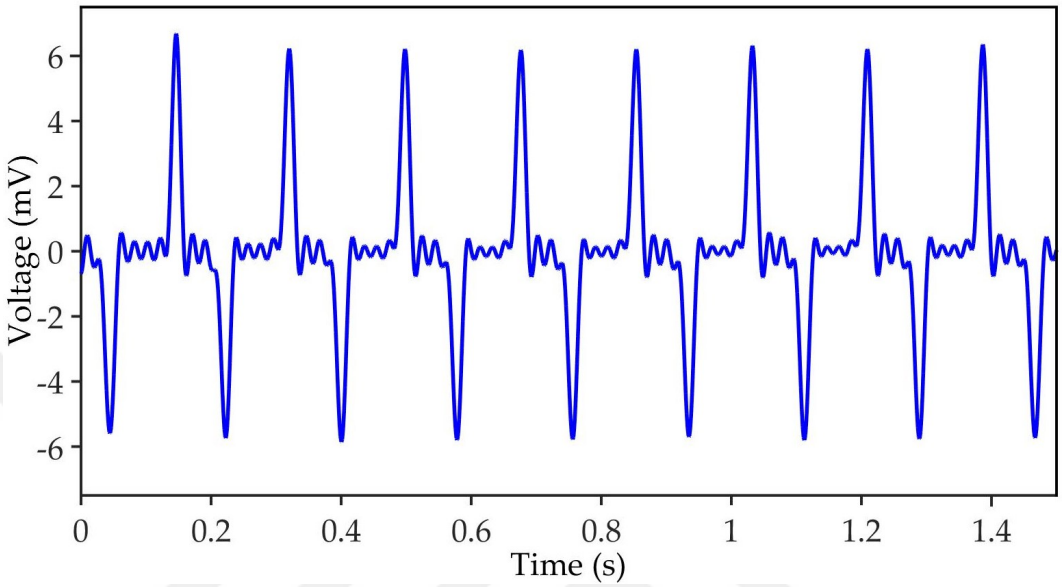

Figure 5.7: V_{oc} signal of the packaged device at 5.67 Hz shaker frequency.

the shaker frequency was increased further. At this point, a prediction has been made about how much voltage the device will produce at 1 m/s. For inducing half cycle of voltage (one peak), the platform moves a total distance $d = 2.5\,\text{mm}$ from edge to edge in time t, the average speed will be $v = d/t$. In figure 5.7, t is found from the graph $0.029\,\text{s}$, hence $v = 0.086\,\text{m/s}$, at frequency of $5.67\,\text{Hz}$. Considering the linear relationship between speed and frequency, it can be said that a speed of 1 m/s can be reached at a frequency of about 65.93 Hz. Plugging this result in the regression line equation of figure 5.8, the peak open circuit voltage induced by the generator is 0.1 V at platform speed of $1\,\text{m/s}$.

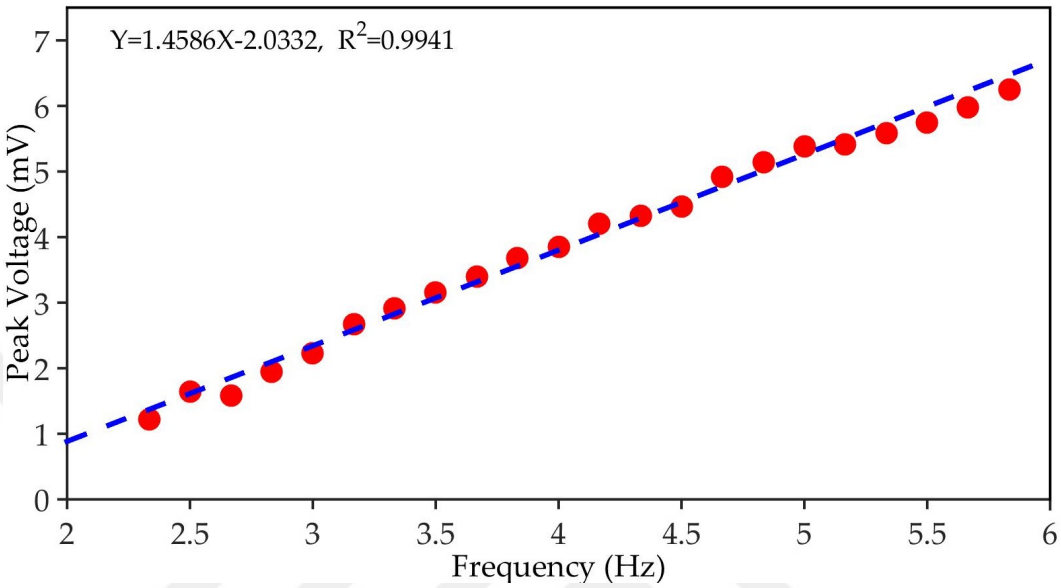

Figure 5.8: V_{oc} signal of the packaged device for a range of shaker frequencies.

5.4 Power Generation Tests

In these tests, a variable resistor was connected as a load to the harvester in parallel. The shaker frequency was set to 4 Hz (40 rpm), and the resistor was changed and the voltage was obtained at each step. The voltage data was recorded than RMS power P_{rms} was extracted from the equation $P_{rms} = \frac{V_R^2}{2R}$, where V_R and R are the load recorded peak voltage and the load resistance, respectively. Figure 5.9 shows the RMS power that corresponds to each load resistance value. The power value is increasing to a maximum value of 0.1 µW at 20 Ω load resistance then decreases for higher resistances. As expected from maximum power transfer theorem (equation 3.4), the maximum power was delivered when the load matches the stator resistance, that is measured 20 Ω (section 4.7).

After determining the value of the resistance at which maximum power was obtained, the change of the transmitted power with respect to the frequency was examined. During this test, the connected load was fixed to the matching

20 Ω, and the voltage on the load was measured at different frequencies. In figure 5.10, an example of a voltage signal recorded at the matching load when the shaker frequency was set to 7.17 Hz (430 rpm). The peak load voltage recorded was 3.71 mV.

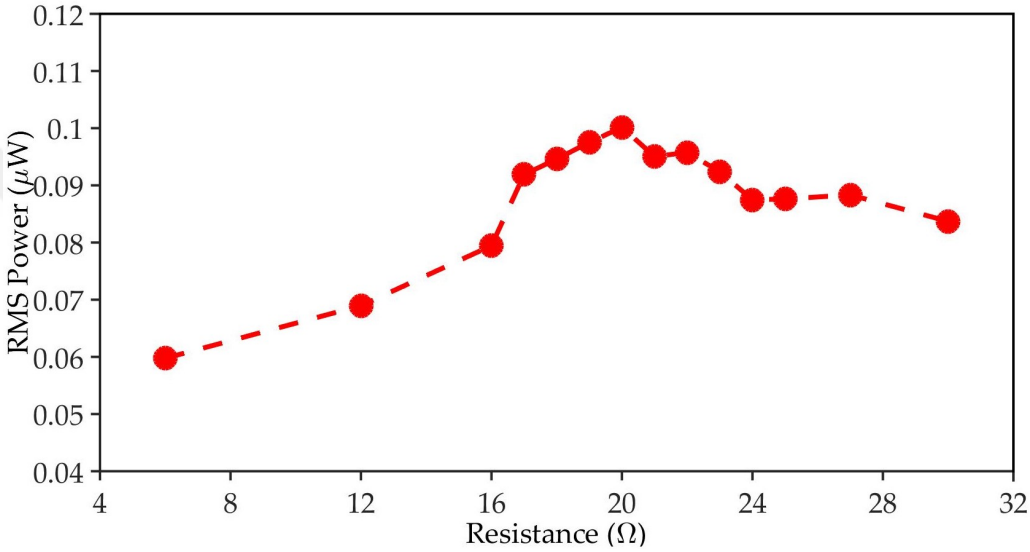

Figure 5.9: RMS power delivered by the generator to a variable load at 4 Hz.

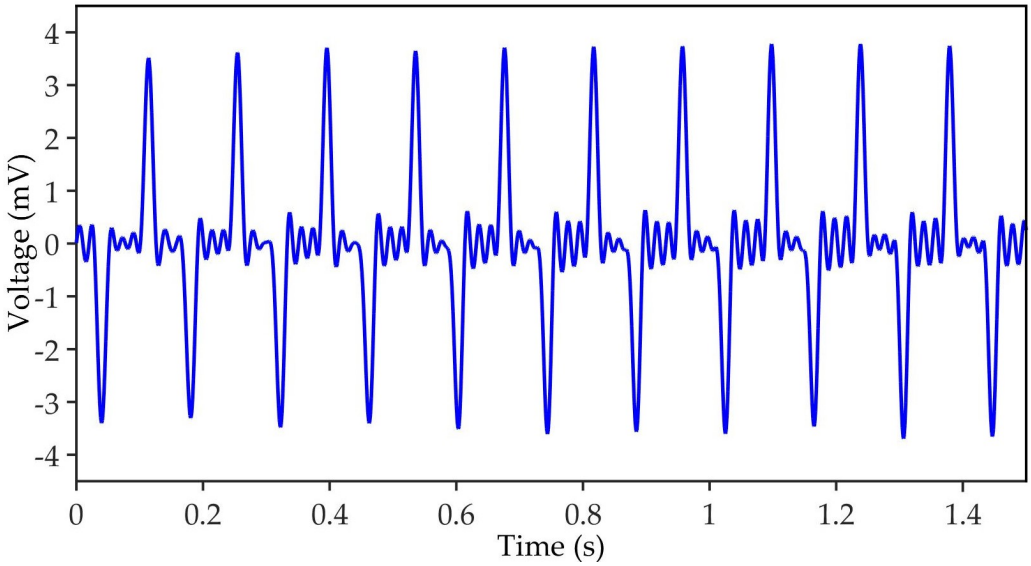

Figure 5.10: Voltage delivered by the device at 20 Ω matching load at 7.17 Hz shaker frequency.

The transmitted RMS power was calculated from voltage data, the results obtained are shown in Figure 5.11. The voltage is linearly related to the frequency, and power is related to voltage squared, hence, power to frequency data can be fitted using polynomial regression. The blue dashed line expresses the polynomial regression with coefficient $R^2 = 0.9862$. The black dashed line expresses the best polynomial regression fit with $R^2 = 0.9977$, Although it contains a linear term, it was used to predict power at 1m/s. The maximum frequency reached in this test was 7.17 Hz. At this frequency, the delivered power was found to be 0.33 µW. The average speed of the platform from the graph in Figure 5.10 was calculated as before and it was found to be 0.1 m/s. Assuming the linear relationship between frequency and speed, 1 m/s corresponds to 71.7 Hz frequency. This value was plugged in the polynomial equation and the power delivered by the generator to the matching load at this speed was found to be 11 µW.

Taking the frequency 5.83 Hz as example which corresponds to platform speed of 0.081 m/s, plugging this velocity in equation 3.17 with $N = 13$ coil turns of the tested device, the resulting voltage is **7.32 mV**, from the graph in figure 5.8, the voltage is **6.25 mV** with 14% error. Substituting 7.32 mV in equation 3.4 ($Z = 20\ \Omega$), the RMS power theoretically is **0.33 µW**. The generator at frequency 5.83 Hz in figure 5.10 delivered an RMS power of **0.23 µW** with 30% error. In addition to stator-to-platform gap distance and coils height effect on the results as mentioned previously, the difference in power is due to the power loss in connection wires resistance.

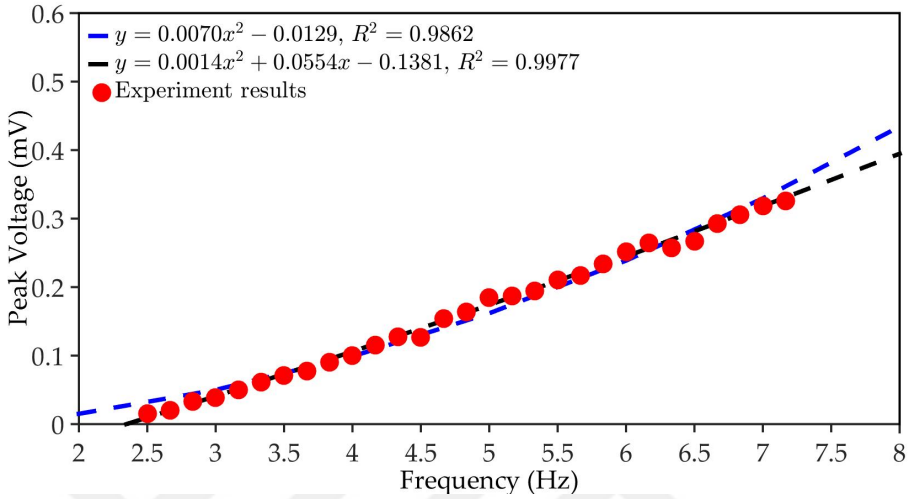

Figure 5.11: RMS delivered power to 20 Ω matching load for a range of shaker frequencies.

5.5 Device on Wristband Testing

The packaged micro-harvester was embedded in a wristband, as shown in figure 5.12, in order to investigate generation performance from some daily body activities. The device was connected to DAQ card with long wires, and the volunteer has worn the wristband during walking and running. The arm movements were driving the generator and voltage data was recorded. The test was done for open voltage and power generation acquisition.

Figure 5.12: The packaged device attached to a wristband worn for testing.

As shown in figure 5.13, the maximum open circuit voltage measured during walking was measured as **4.4 mV**. In addition, the peak power transferred to the resistor using the data in figure 5.14 is calculated as **0.14 µW**. During walking, the arm and wrist move forward and backward in 50 cm peak to peak amplitude at about 1 Hz, and in the middle of this harmonic movement, the wrist reaches a speed of about 0.9 m/s when passing through the waist line. However, as already mentioned, the platform was moving suddenly and impulsively on both ends of the movement only because the movement amplitude is high. On the other hand, the platform moves at a relatively low speed when the arm is in 45° position with respect to the body. The duration of one peak voltage is 0.0383 s, generated for the platform displacement of 2.5 mm, yields to 0.065 m/s speed, considering speed-frequency linear relation, this speed corresponds to 4.3 Hz. At this frequency, the generated voltage is **4.24 mV** and power is **0.13 µW** using regression line equation of open circuit voltage and polynomial regression equation power, respectively, hence, the speed, voltage and power values obtained during walking are within expectations.

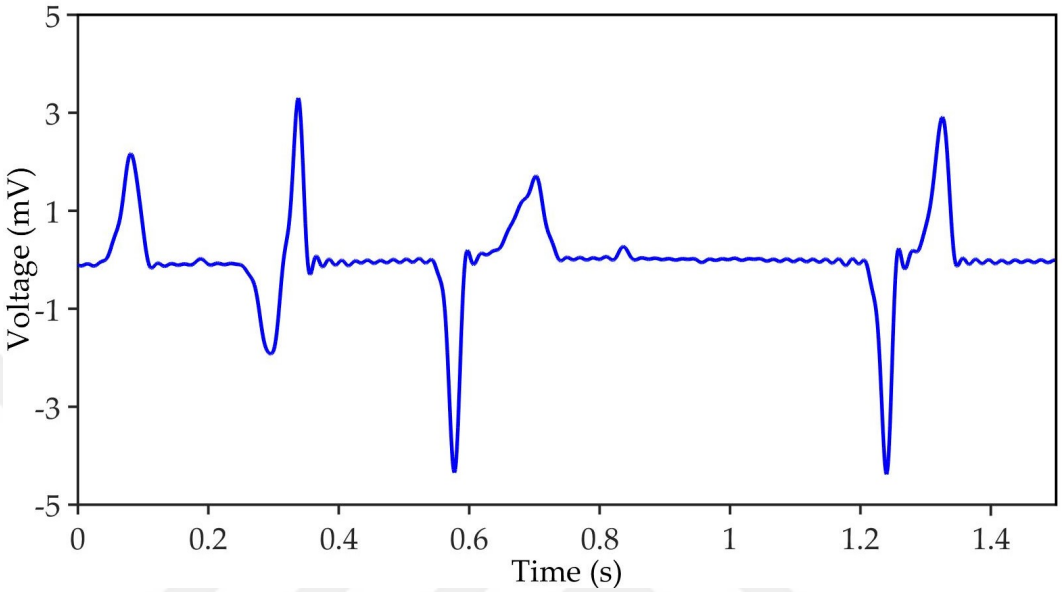

Figure 5.13: Open circuit Voltage induced by the generator on wristband during walking activity.

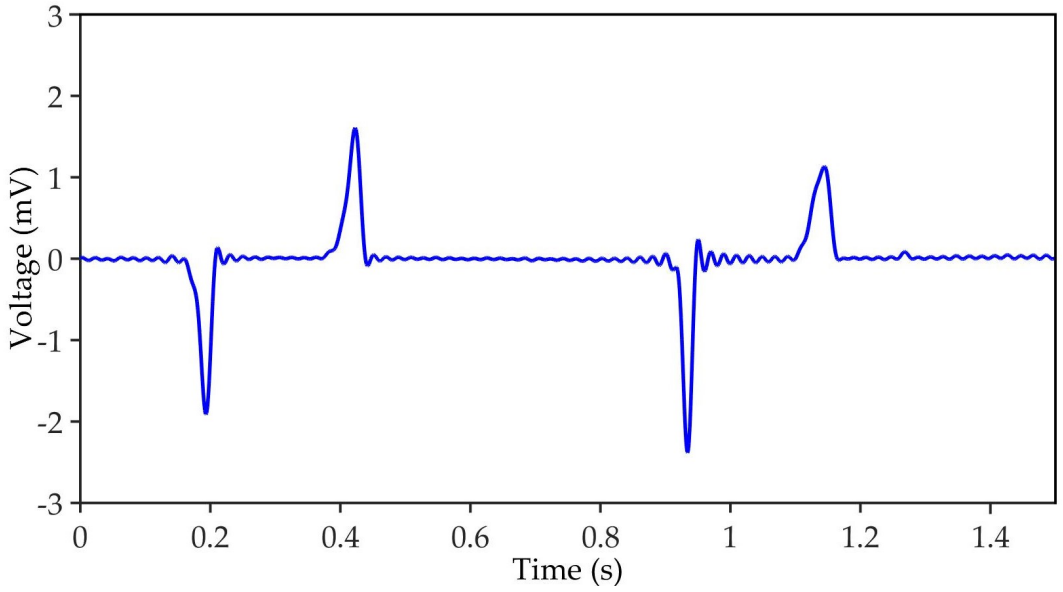

Figure 5.14: Voltage signal at 20 Ω load during walking activity.

In the activity of running tests, as expected, higher values were obtained compared to walking. The maximum open circuit voltage recorded was **6.85**

mV as shown in figure 5.15, and the power transferred to 20 Ω resistor was calculated as **0.2 µW** from voltage data displayed in figure 5.16.

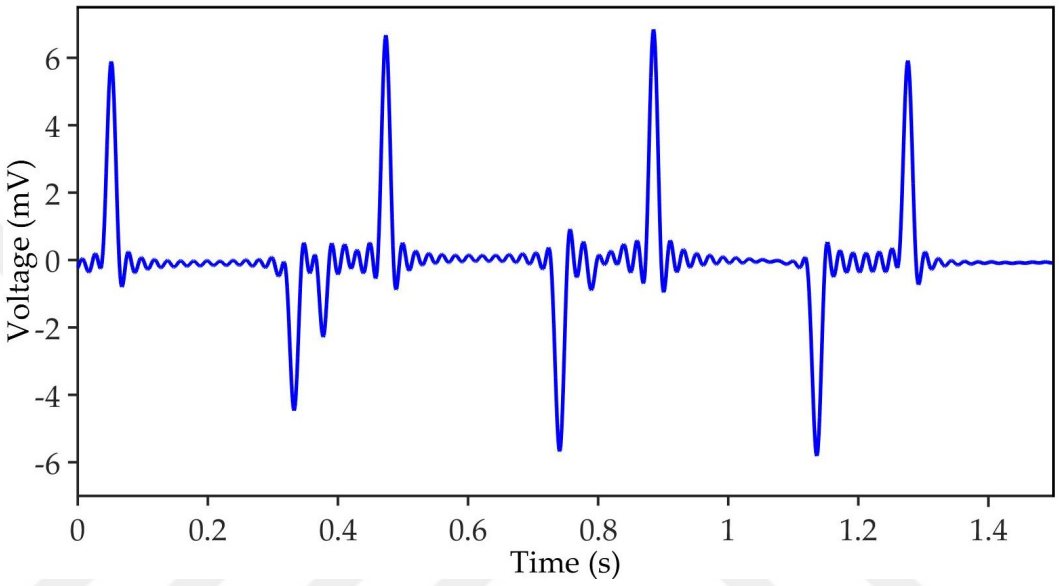

Figure 5.15: Open circuit voltage provided by the device during running activity.

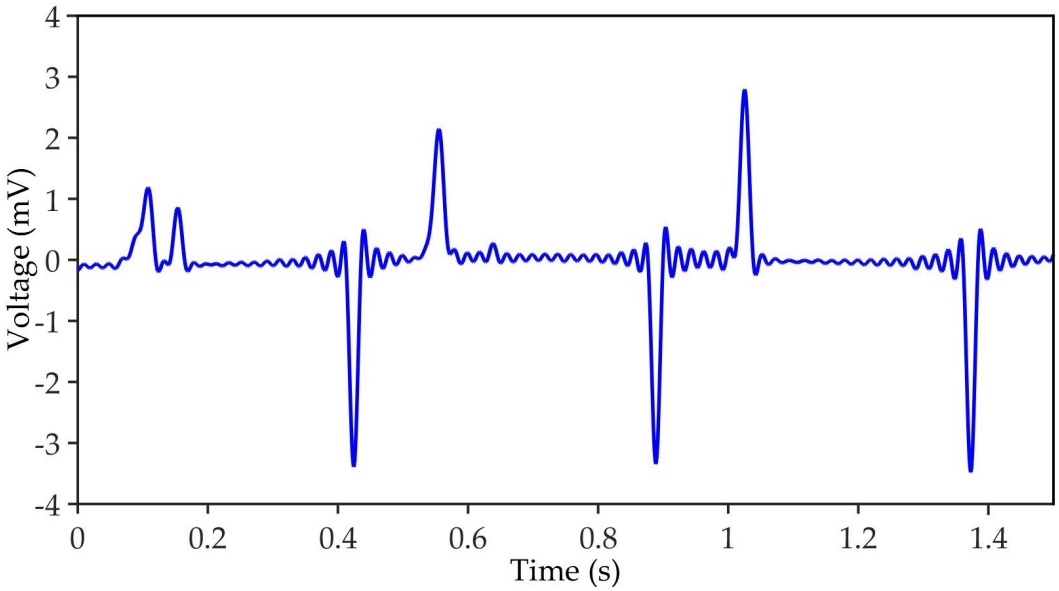

Figure 5.16: Voltage signal at 20 Ω load during running activity.

The average speed of the platform is calculated to be 0.1 m/s, which corresponds to 7 Hz. From regression equations, the voltage is **8.7 mV** and the delivered power is **0.32 µW**. By comparison, these values once again are agreeably in the range of the test results. Another activity that involves the wrist movement is the activity of erasing with a rubber, to name but a few. It was taken as an example to actuate the device in the bracelet for generation, the rubber was being moved by the the volunteer in about 4 cm amplitude. In figure 5.17, the maximum open circuit voltage recorded was **5.73 mV** with 0.093 m/s average speed, and a delivered power of **0.17 µW** to the matching load was calculated from the graph in figure 5.17. The corresponding frequency for such speed is 6.13 Hz and the voltage and power found from regression equations are **6.9 mV** and **0.27 µW**, respectively.

It was planned at the beginning of the project to test the micro-harvester for battery charging. However, these performance values were limited by the shaker speed bellow 1 m/s and coils number of turns, both reasons were out of control. These results at this stage are bellow the requirements to operate the rectifier or the charge pump circuit for battery charging, nevertheless, a technique is suggested as future work to increase the coil number turns with a CMOS AC-DC charging interface in chapter 6.

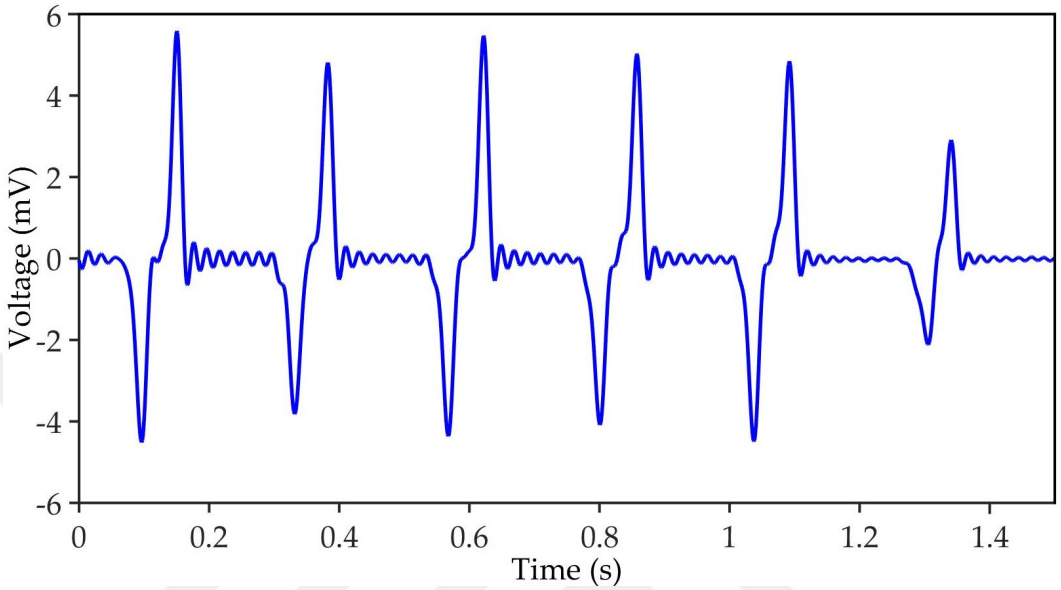

Figure 5.17: Open circuit voltage provided by the device during the activity of using a rubber.

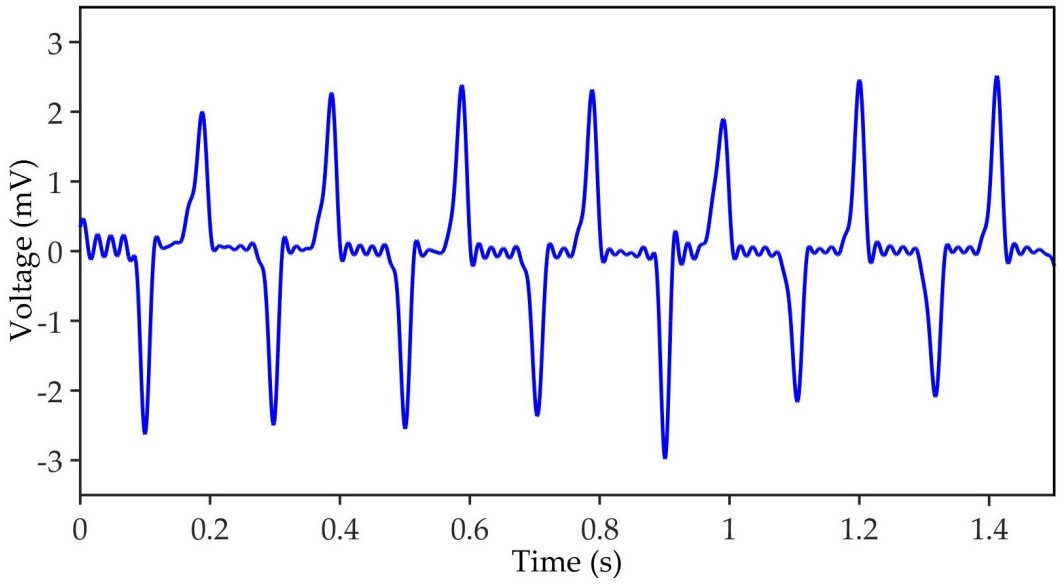

Figure 5.18: Voltage recorded at 20 Ω load during the activity of using a rubber.

Chapter 6

Conclusion and Future Work

The micro-energy harvester developed within the scope of the project was successfully developed and tested. Tests applied by fixing the device to the linear shaker produced 6.25 mV open circuit voltage and 0.33 µW power. Furthermore, in the analyzes made using the obtained data, it was calculated that these values would reach 0.1 V and 11 µW when the platform reaches 1 m/s speed. All these results were found to be consistent with the analysis and simulations on the performance of the device. By integrating the generator into a wristband, electricity is produced during walking and running. During walking, open circuit voltage of 4.4 mV and 0.14 µW of power were reached, while open circuit voltage of 6.85 mV and power of 0.2 µW were reached during running. Prior to these performance results, several modifications in the device design were made in parallel with tests to reach the desired structure, also the materials used to fabricate the device prototypes were improved to reach a successful winding on the micro-coils and to insure device stability as well. Accordingly, the related fabrication techniques were updated at each phase.

Although the device has been proven to work as intended and can produce power in the microwatt range, it is possible to improve device performance with some modifications to the design and test. Two important factors were found to be effective in achieving higher voltage and power values after experiments, namely high number of turns and high platform speeds. At the beginning of the project, the number of windings targeted could not be reached due to the limitations caused by the wire bonding machine and coils stability issues as mentioned earlier. At this point an alternative option has been developed. In this work, the micro-coils were wrapped only once (single layer of turns) for each micro-coil.

Another alternative is proposed as a future work in figure 6.1, for simplicity, only two columns of a stator are represented. The single contact pad is divided into four small pads A, B, C and D. The capillary makes the first coil winding starting from pad A and follows a counter clockwise trajectory around the left column, then ends with a wedge on the pad B. In the same way, the second coil is wound from pad B to pad C, identically, pads C and D will be terminals for a third coil, finally a fourth coil starts from pad D and finishes at pad E. Similarly, other four coils are made around the middle column starting from pad E but in the clockwise direction. On this count, the columns overall coils are connected in series. In this way the maximum number of turns per column

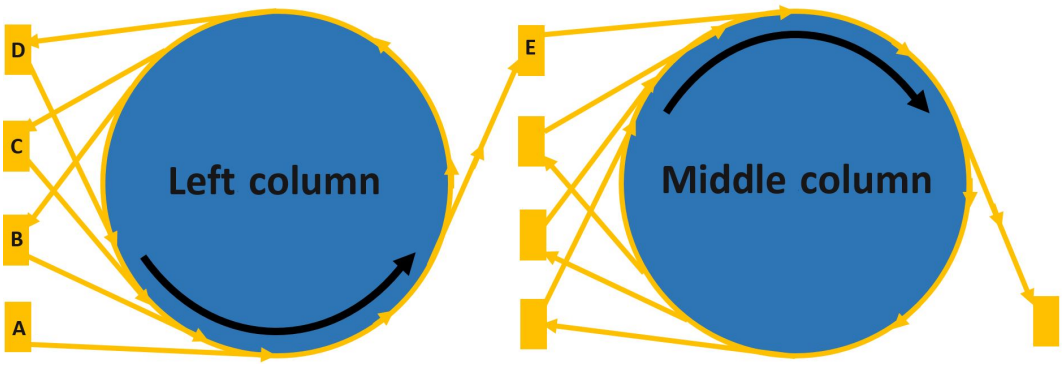

Figure 6.1: Suggested column multi-winding to increase the voltage by four folds.

could be increased to 56, therefore, the total obtained voltage and delivered power will be increased by four folds. Our work with the group in Germany continues in this direction.

The second factor limiting the production of voltage and power is the relative low speed between the platform and the stator. It is predicted that the speeds of 1 m/s can be reached in the estimations made before the experiments. However, the maximum was 0.1 m/s in running tests in conditions similar to actual operating conditions. Hence, about 10 times lower speed levels have been observed. The use of a linear shaker device that can be reduced to 2.5 mm in amplitude on the test setup and the frequency can be increased to 100 Hz can be tested to see how the device behaves at such speed. In addition, this much speed can be obtained at different parts of the body moving in an impulsive manner with small amplitudes.

Following the implementation of these suggestions, the device will be ready for battery charging tests. An interface to regulate the voltage can be used then, such as the 0.25 mm^2 AC-DC converter circuit based on CMOS technology reported by Herbawe *et al.* which is capable of converting sub-1V amplitude voltage signal with low frequency as 5 Hz at 94% efficiency [92]. By doing so and fully packaging the device in vacuum, it will be ready for implantation to a test animal for performing *in vivo* tests to power an implanted pacemaker.

Bibliography

[1] A. Harb, "Energy harvesting: State-of-the-art," *Renewable Energy*, vol. 36, no. 10, pp. 2641–2654, 2011.

[2] G. W. Taylor, *Piezoelectricity*. Gordon and Breach Science Publishers, 1985.

[3] R. Riemer and A. Shapiro, "Biomechanical energy harvesting from human motion: theory, state of the art, design guidelines, and future directions." *Journal of neuroengineering and rehabilitation*, vol. 8, p. 22, 2011.

[4] J. A. Paradiso and T. Starner, "Energy scavenging for mobile and wireless electronics," *IEEE Pervasive Computing*, vol. 4, no. 1, pp. 18–27, 2005.

[5] P. D. Mitcheson, E. M. Yeatman, G. K. Rao, A. S. Holmes, and T. C. Green, "Energy harvesting from human and machine motion for wireless electronic devices," *Proceedings of the IEEE*, vol. 96, no. 9, pp. 1457–1486, 2008.

[6] a. Khaligh, P. Zeng, and C. Zheng, "Kinetic Energy Harvesting Using Piezoelectric and Electromagnetic TechnologiesState of the Art," *Industrial Electronics, IEEE Transactions on*, vol. 57, no. 3, pp. 850–860, 2010.

[7] J. Olivo, S. Carrara, G. De Micheli, and G. D. Micheli, "Energy Harvesting and Remote Powering for Implantable Biosensors," *IEEE Sensors Journal*, vol. 11, no. 7, pp. 1573–1586, 2011.

[8] R. A. Bullen, T. C. Arnot, J. B. Lakeman, and F. C. Walsh, "Biofuel cells and their development," *Biosensors and Bioelectronics*, vol. 21, no. 11, pp. 2015–2045, 2006.

[9] A. Roy, A. Klinefelter, F. B. Yahya, X. Chen, L. P. Gonzalez-Guerrero, C. J. Lukas, D. A. Kamakshi, J. Boley, K. Craig, M. Faisal, S. Oh, N. E. Roberts, Y. Shakhsheer, A. Shrivastava, D. P. Vasudevan, D. D. Wentzloff, and B. H. Calhoun, "A 6.45 μ W Self-Powered SoC with Integrated Energy-Harvesting Power Management and ULP Asymmetric Radios for Portable Biomedical Systems," in *IEEE Transactions on Biomedical Circuits and Systems*, vol. 9, no. 6, 2015, pp. 862–874.

[10] P. Kamalinejad, C. Mahapatra, Z. Sheng, S. Mirabbasi, V. C. Victor, and Y. L. Guan, "Wireless energy harvesting for the Internet of Things," *IEEE Communications Magazine*, vol. 53, no. 6, pp. 102–108, jun 2015.

[11] J. M. Donelan, Q. Li, V. Naing, J. a. Hoffer, D. J. Weber, and a. D. Kuo, "Biomechanical energy harvesting: generating electricity during walking with minimal user effort." *Science (New York, N.Y.)*, vol. 319, no. 5864, pp. 807–810, 2008.

[12] "Pavegen - The Next Step." [Online]. Available: http://www.pavegen.com/

[13] S. K. Islam and M. R. Haider, "Sensors and low power signal processing," in *Sensors and Low Power Signal Processing*. Springer US, 2010, ch. 2, pp. 1–118.

[14] A. Singh Gaur and J. Budakoti, "Energy Efficient Advanced Low Power CMOS Design to reduce power consumption in Deep Submicron

Technologies in CMOS Circuit for VLSI Design," *International Journal of Advanced Research in Computer and Communication Engineering*, vol. 3, no. 6, pp. 2278–1021, 2014.

[15] W. Greatbatch and C. F. Holmes, "History of implantable devices," *IEEE Engineering in Medicine and Biology Magazine*, vol. 10, no. 3, pp. 38–41+49, sep 1991.

[16] D. Chen, C. Wang, W. Chen, Y. Chen, and J. X. J. Zhang, "PVDF-Nafion nanomembranes coated microneedles for in vivo transcutaneous implantable glucose sensing," *Biosensors and Bioelectronics*, vol. 74, pp. 1047–1052, 2015.

[17] Markets&Markets, "Bio-Implants Market Research Report, Forecast to 2017," Tech. Rep., 2012. [Online]. Available: http://www.marketsandmarkets.com/Market-Reports/bio-implants-market-728.html

[18] W. Khan, E. Muntimadugu, M. Jaffe, and A. J. Domb, "Implantable Medical Devices," 2014, pp. 33–59.

[19] A. Sanni, "A Threetier bio-implantable sensor monitoring and communications platform," Ph.D. dissertation, 2013. [Online]. Available: https://spiral.imperial.ac.uk/handle/10044/1/14633

[20] J. Martinez-Quijada and S. Chowdhury, "Body-motion driven MEMS generator for implantable biomedical devices," *Canadian Conference on Electrical and Computer Engineering*, pp. 164–167, 2007.

[21] K. Dong, B. Jia, C. Yu, W. Dong, F. Du, and H. Liu, "Microbial fuel cell as power supply for implantable medical devices: A novel configuration design for simulating colonic environment," *Biosensors and Bioelectronics*, vol. 41, no. 1, pp. 916–919, 2013.

[22] H. Jabbar, Y. S. Song, and T. T. Jeong, "RF energy harvesting system and circuits for charging of mobile devices," *IEEE Transactions on Consumer Electronics*, vol. 56, no. 1, pp. 247–253, feb 2010.

[23] A. Yakovlev, S. Kim, and A. Poon, "Implantable biomedical devices: Wireless powering and communication," *IEEE Communications Magazine*, vol. 50, no. 4, pp. 152–159, 2012.

[24] O. Brand, G. Fedder, C. Hierold, J. Korvink, and O. Tabata, *Micro energy harvesting*, 2015.

[25] J. S. Ho, A. J. Yeh, S. Kim, and A. S. Y. Poon, "Wireless powering for miniature implantable systems," *Neural Computation, Neural Devices, and Neural Prosthesis*, vol. 101, no. 6, pp. 313–334, 2014.

[26] M. Catrysse, B. Hermans, and R. Puers, "An inductive power system with integrated bi-directional data-transmission," *Sensors and Actuators, A: Physical*, vol. 115, no. 2-3 SPEC. ISS., pp. 221–229, 2004.

[27] B. Smith, Z. Tang, M. W. Johnson, S. Pourmehdi, M. M. Gazdik, J. R. Buckett, and P. Hunter Peckham, "An externally powered, multichannel, implantable stimulator-telemeter for control of paralyzed muscle," *IEEE Transactions on Biomedical Engineering*, vol. 45, no. 4, pp. 463–475, 1998.

[28] J. H. Cheong, S. S. Y. Ng, X. Liu, R. F. Xue, H. J. Lim, P. B. Khannur, K. L. Chan, A. A. Lee, K. Kang, L. S. Lim, C. He, P. Singh, W. T. Park, and M. Je, "An inductively powered implantable blood flow sensor microsystem for vascular grafts," *IEEE Transactions on Biomedical Engineering*, vol. 59, no. 9, pp. 2466–2475, 2012.

[29] B. Lenaerts and R. Puers, "An inductive power link for a wireless endoscope," *Biosensors and Bioelectronics*, vol. 22, no. 7, pp. 1390–1395, 2007.

[30] Y. Y. Ko, S. L. Ho, W. N. Fu, and X. Zhang, "A novel hybrid resonator for wireless power delivery in bio-implantable devices," *IEEE Transactions on Magnetics*, vol. 48, no. 11, pp. 4518–4521, 2012.

[31] K. Agarwal, R. Jegadeesan, Y. X. Guo, and N. V. Thakor, "Wireless Power Transfer Strategies for Implantable Bioelectronics," pp. 136–161, 2017.

[32] J. Lueke and W. A. Moussa, "MEMS-based power generation techniques for implantable biosensing applications," *Sensors*, vol. 11, no. 2, pp. 1433–1460, 2011.

[33] F. Karim and S. Zeadally, "Energy harvesting in wireless sensor networks : A comprehensive review," *Renewable and Sustainable Energy Reviews*, vol. 55, no. January, pp. 1041–1054, 2016.

[34] L. Francioso, C. De Pascali, I. Farella, C. Martucci, P. Cretì, P. Siciliano, and A. Perrone, "Flexible Thermoelectric Generator for Wearable Biometric Sensors," pp. 747–750, 2010.

[35] J. P. Carmo, L. M. Goncalves, and J. H. Correia, "Thermoelectric microconverter for energy harvesting systems," *IEEE Transactions on Industrial Electronics*, vol. 57, no. 3, pp. 861–867, mar 2010.

[36] V. Lenov, P. Fiorini, S. Sedky, T. Torfs, and C. Van Hoof, "Thermo electric MEMS generators as a power supply for a body area network," *Solid-State Sensors, Actuators and Microsystem*, vol. 1, pp. 291–294, 2005.

[37] Z. Wang, V. Leonov, P. Fiorini, and C. Van Hoof, "Realization of a wearable miniaturized thermoelectric generator for human body applications," *Sensors and Actuators, A: Physical*, vol. 156, no. 1, pp. 95–102, 2009.

[38] M.-K. Kim, M.-S. Kim, S. Lee, C. Kim, and Y.-J. Kim, "Flexible thermoelectric generator for human body heat energy harvesting," *Smart Materials and Structures*, vol. 23, no. 10, p. 105002, 2014.

[39] Y. Yang, G. Dong Xu, and J. Liu, "A Prototype of an Implantable Thermoelectric Generator for Permanent Power Supply to Body Inside a Medical Device," *Journal of Medical Devices*, vol. 8, no. 1, p. 014507, dec 2013.

[40] S. Kumari, S. S. Sahu, and B. Gupta, "A low voltage pre start up circuit for thermal energy harvesting applications," in *Proceedings of the 2017 International Conference on Wireless Communications, Signal Processing and Networking, WiSPNET 2017*, vol. 2018-Janua. IEEE, mar 2018, pp. 1970–1973.

[41] Y. Yang, X.-J. Wei, and J. Liu, "Suitability of a thermoelectric power generator for implantable medical electronic devices," *Journal of Physics D: Applied Physics*, vol. 40, no. 18, pp. 5790–5800, 2007.

[42] V. Oncescu and D. Erickson, "A microfabricated low cost enzyme-free glucose fuel cell for powering low-power implantable devices," *Journal of Power Sources*, vol. 196, no. 22, pp. 9169–9175, 2011.

[43] S. Inoue, E. A. Parra, A. Higa, and L. Lin, "Cell-to-electrode contact structures for power density enhancements in microbial fuel cells," in *Proceedings of the IEEE International Conference on Micro Electro Mechanical Systems (MEMS)*. IEEE, jan 2011, pp. 1297–1300.

[44] C. P. B. Siu and M. Chiao, "A microfabricated PDMS microbial fuel cell," *Journal of Microelectromechanical Systems*, vol. 17, no. 6, pp. 1329–1341, dec 2008.

[45] S. K. Chaudhuri and D. R. Lovley, "Electricity generation by direct oxidation of glucose in mediatorless microbial fuel cells," *Nature Biotechnology*, vol. 21, no. 10, pp. 1229–1232, 2003.

[46] Y. Han, C. Yu, and H. Liu, "A microbial fuel cell as power supply for implantable medical devices," *Biosensors and Bioelectronics*, vol. 25, no. 9, pp. 2156–2160, 2010.

[47] N. Mano, F. Mao, and A. Heller, "Characteristics of a miniature compartment-less glucose-O2 biofuel cell and its operation in a living plant," *Journal of the American Chemical Society*, vol. 125, no. 21, pp. 6588–6594, 2003.

[48] X. Wei and J. Liu, "Power sources and electrical recharging strategies for implantable medical devices," *Frontiers of Energy and Power Engineering in China*, vol. 2, no. 1, pp. 1–13, 2008.

[49] S. Kerzenmacher, J. Ducrée, R. Zengerle, and F. von Stetten, "Energy harvesting by implantable abiotically catalyzed glucose fuel cells," pp. 1–17, jul 2008.

[50] H. Ren, C. Jiang, and J. Chae, "Effect of temperature on a miniaturized microbial fuel cell (MFC)," *Micro and Nano Systems Letters*, vol. 5, no. 1, p. 13, 2017.

[51] B. Min, Ó. B. Román, and I. Angelidaki, "Importance of temperature and anodic medium composition on microbial fuel cell (MFC) performance," *Biotechnology Letters*, vol. 30, no. 7, pp. 1213–1218, 2008.

[52] M. Southcott, K. MacVittie, J. Halámek, L. Halámková, W. D. Jemison, R. Lobel, and E. Katz, "A pacemaker powered by an implantable biofuel cell operating under conditions mimicking the human blood circulatory system–battery not included." *Physical chemistry chemical physics : PCCP*, vol. 15, no. 17, pp. 6278–83, 2013.

[53] R. F. Drake, B. K. Kusserow, S. Messinger, and S. Matsuda, "A Tissue Implantable Fuel Cell Power Supply," pp. 199–205, 1970.

[54] P. D. Mitcheson, T. Sterken, C. He, M. Kiziroglou, E. M. Yeatman, and R. Puers, "Electrostatic microgenerators," *Measurement and Control*, vol. 41, no. 4, pp. 114–119, 2008.

[55] R. TASHIRO, N. KABEI, H. KOTERA, K. KATAYAMA, Y. ISHIZUKA, F. TSUBOI, and K. TSUCHIYA, "Development of an Electrostatic Generator that Harnesses the Motion of a Living Body. Generation Using Heartbeat." *Transactions of the Japan Society of Mechanical Engineers Series C*, vol. 67, no. 659, pp. 2307–2313, dec 2001.

[56] P. Miao, P. D. Mitcheson, A. S. Holmes, E. M. Yeatman, T. C. Green, and B. H. Stark, "Mems inertial power generators for biomedical applications," in *Microsystem Technologies*, vol. 12, no. 10-11, 2006, pp. 1079–1083.

[57] Q. Fu and Y. Suzuki, "MEMS vibration electret energy harvester with combined electrodes," in *Proceedings of the IEEE International Conference on Micro Electro Mechanical Systems (MEMS)*. IEEE, jan 2014, pp. 409–412.

[58] S. Priya, H.-C. Song, Y. Zhou, R. Varghese, A. Chopra, S.-G. Kim, I. Kanno, L. Wu, D. S. Ha, J. Ryu, and R. G. Polcawich, "A Review on Piezoelectric Energy Harvesting: Materials, Methods, and Circuits," *Energy Harvesting and Systems*, vol. 4, no. 1, 2017.

[59] J. Sirohi and I. Chopra, "Fundamental understanding of piezoelectric strain sensors," *Journal of Intelligent Material Systems and Structures*, vol. 11, no. 4, pp. 246–257, 2000.

[60] F. Lu, H. P. Lee, and S. P. Lim, "Modeling and analysis of micro piezoelectric power generators for micro-electromechanical-systems applications," *Smart Materials and Structures*, vol. 13, no. 1, pp. 57–63, 2004.

[61] N. S. Shenck and J. A. Paradiso, "Energy scavenging with shoe-mounted piezoelectrics," *IEEE Micro*, vol. 21, no. 3, pp. 30–42, 2001.

[62] L. Moro and D. Benasciutti, "Harvested power and sensitivity analysis of vibrating shoe-mounted piezoelectric cantilevers," *Smart Materials and Structures*, vol. 19, no. 11, p. 115011, 2010.

[63] R. Yang, Y. Qin, C. Li, G. Zhu, and Z. L. Wang, "Converting biomechanical energy into electricity by a muscle-movement- driven nanogenerator," *Nano Letters*, vol. 9, no. 3, pp. 1201–1205, 2009.

[64] B. E. Lewandowski, K. L. Kilgore, and K. J. Gustafson, "In vivo demonstration of a self-sustaining, implantable, stimulated-muscle-powered piezoelectric generator prototype," *Annals of Biomedical Engineering*, vol. 37, no. 11, pp. 2390–2401, 2009.

[65] C. Dagdeviren, B. D. Yang, Y. Su, P. L. Tran, P. Joe, E. Anderson, J. Xia, V. Doraiswamy, B. Dehdashti, X. Feng, B. Lu, R. Poston, Z. Khalpey, R. Ghaffari, Y. Huang, M. J. Slepian, and J. A. Rogers, "Conformal piezoelectric energy harvesting and storage from motions of the heart, lung, and diaphragm," *Proceedings of the National Academy of Sciences*, vol. 111, no. 5, pp. 1927–1932, feb 2014.

[66] W. Chin Chye, Z. Dahari, O. Sidek, and M. Azman Miskam, "Electromagnetic Micro Power Generator -A Comprehensive Survey."

[67] M. Beyaz, H. Baelhadj, S. Habibiabad, S. Adhikari, H. Davoodi, and V. Badilita, "A non-resonant kinetic energy harvester for bioimplantable applications," *Micromachines*, vol. 9, no. 5, 2018.

[68] M. I. Beyaz, B. M. Hanrahan, J. Feldman, and R. Ghodssi, "An integrated permanent-magnet microturbogenerator supported on microball bearings," *Journal of Microelectromechanical Systems*, vol. 22, no. 3, pp. 794–803, 2013.

[69] P. Niu and P. Chapman, "Design and performance of linear biomechanical energy conversion devices," *PESC Record - IEEE Annual Power Electronics Specialists Conference*, 2006.

[70] D. Carroll and M. Duffy, "Modelling, design, and testing of an electromagnetic power generator optimized for integration into shoes," *Proceedings of the Institution of Mechanical Engineers, Part I: Journal of Systems and Control Engineering*, 2012.

[71] T. von Büren and G. Tröster, "Design and optimization of a linear vibration-driven electromagnetic micro-power generator," *Sensors and Actuators, A: Physical*, vol. 135, no. 2, pp. 765–775, 2007.

[72] H. Kulah and K. Najafi, "Energy Scavenging From Low-Frequency Vibrations by Using Frequency Up-Conversion for Wireless Sensor Applications," *Sensors Journal, IEEE*, vol. 8, no. 3, pp. 261–268, 2008.

[73] N. N. H. Ching, H. Y. Wong, W. J. Li, P. H. W. Leong, and Z. Wen, ""A Laser-micromachined Vibrational to Electrical Power Transducer for Wireless Sensing Systems"," *Inter.Conf. on Solid-state sensors and Actuators*, vol. 98, no. June, pp. 1–4, 2001.

[74] A. S. Holmes, G. Hong, K. R. Pullen, and k. R. Buffard, "AXIAL-FLOW MICROTURBINE WITH ELECTROMAGNETIC GENERATOR: DESIGN, CFD SIMULATION, AND PROTOTYPE DEMONSTRATION," *IEE Proceedings - MEMS*, pp. 568–571, 2004.

[75] S. N. Suzuki, T. Katane, H. Saotome, and O. Saito, "Electric power-generating system using magnetic coupling for deeply implanted medical electronic devices," *IEEE Transactions on Magnetics*, vol. 38, no. 5 I, pp. 3006–3008, 2002.

[76] Y. Wang, Q. Zhang, L. Zhao, and E. S. Kim, "NON-RESONANT , BROAD-BAND VIBRATION-ENERGY HARVESTER BASED ON

SELF-ASSEMBLED LIQUID BEARING Yufeng Wang *, Qian Zhang , Lurui Zhao , and Eun Sok Kim Department of Electrical Engineering-Electrophysics University of Southern California Los Angeles , CA 900," pp. 614–617, 2015.

[77] D. G. H. R. Florentino, R. C. S. Freire, A. V. S. Sá, C. Florentino, "Electrostatic vibration energy harvester with piezoelectric start-up generator," in *Proceedings - IEEE International Symposium on Circuits and Systems*. IEEE, may 2011, pp. 1343–1346.

[78] J. Davis, "Overview of Biomaterials," *Material for medical devices*, p. 315, 2003.

[79] S. H. Kim, J. H. Moon, J. H. Kim, S. M. Jeong, and S. H. Lee, "Flexible, stretchable and implantable PDMS encapsulated cable for implantable medical device," *Biomedical Engineering Letters*, vol. 1, no. 3, pp. 199–203, 2011.

[80] O. G. Gruschke, N. Baxan, L. Clad, K. Kratt, D. von Elverfeldt, A. Peter, J. Hennig, V. Badilita, U. Wallrabe, and J. G. Korvink, "Lab on a chip phased-array MR multi-platform analysis system." *Lab on a chip*, vol. 12, no. 3, pp. 495–502, 2012.

[81] K. Kratt, M. Seidel, M. Emmenegger, U. Wallrabe, and J. G. Korvink, "Solenoidal micro coils manufactured with a wire bonder," in *Proceedings of the IEEE International Conference on Micro Electro Mechanical Systems (MEMS)*. IEEE, jan 2008, pp. 996–999.

[82] K. Kratt, V. Badilita, T. Burger, J. Mohr, M. B??rner, J. G. Korvink, and U. Wallrabe, "High aspect ratio PMMA posts and characterization method for micro coils manufactured with an automatic wire bonder," *Sensors and Actuators, A: Physical*, vol. 156, no. 2, pp. 328–333, 2009.

[83] K. Kratt, V. Badilita, T. Burger, J. G. Korvink, and U. Wallrabe, "A fully MEMS-compatible process for 3D high aspect ratio micro coils obtained with an automatic wire bonder," *Journal of Micromechanics and Microengineering*, vol. 20, no. 1, p. 015021, 2010.

[84] M. T. Thompson and M. T. Thompson, "Inductance Calculation Techniques — Part II: Approximations and Handbook Methods," *Control*, no. December, pp. 1–11, 1999.

[85] "IBS Magnet Info." [Online]. Available: https://www.ibsmagnet.com/knowledge/flussdichte.php

[86] K. Khanafer, A. Duprey, M. Schlicht, and R. Berguer, "Effects of strain rate, mixing ratio, and stress-strain definition on the mechanical behavior of the polydimethylsiloxane (PDMS) material as related to its biological applications," *Biomedical Microdevices*, vol. 11, no. 2, pp. 503–508, 2009.

[87] T. Ishisaka and H. Sato, "Bio-Actuated Power Generator Using Heart Muscle Cells on a Pdms Membrane," *Solid-State Sensors, Actuators and Microsystems Conference, TRANSDUCERS . International. IEEE*, pp. 903–906, 2007.

[88] L. Averous, L. Moro, P. Dole, and C. Fringant, "Properties of thermoplastic blends: Starch-polycaprolactone," *Polymer*, vol. 41, no. 11, pp. 4157–4167, 2000.

[89] M. A. Hopcroft, W. D. Nix, and T. W. Kenny, "What is the Young's modulus of silicon?" *Journal of Microelectromechanical Systems*, vol. 19, no. 2, pp. 229–238, 2010.

[90] Cambridge University Engineering Department, "Materials data book," *Materials Courses*, pp. 1–41, 2003. [Online]. Available: http://www-mdp.eng.cam.ac.uk/web/library/enginfo/cueddatabooks/materials.pdf

[91] Y. Ramot, M. Haim-Zada, A. J. Domb, and A. Nyska, "Biocompatibility and safety of PLA and its copolymers," pp. 153–162, 2016.

[92] A. S. Herbawi, O. Paul, and T. Galchev, "An ultra-low-power active AC-DC CMOS converter for sub-1V integrated energy harvesting applications," in *Proceedings of IEEE Sensors*. IEEE, nov 2013, pp. 1–4.

Appendix A

3D Coils Winding Process

At the beginning, data base of all measurements are entered into Matlab code including pad size, posts dimensions, inter-distances...etc. and the program outputs the coordinates data, which are fed into the wire bonder software. The wafer is initially installed on the perforated pad, that holds the wafer by vacuum and pre-heats the substrate before bonding process. A picture of a wafer under wire-bonding process is shown in figure A.1. The steps to perform a complete coil winding are:

1- **Ball bonding:**

- A ball bond tool implements a thermo-compression bond by pressing heated gold/copper balls onto metallized pads.
- The thermosonic ball bond process begins with an electric discharge to melt the wire and produce a ball at the exposed wire end (see figure A.2a-b).
- The capillary descends onto the pad, pressing the gold ball into bonding with the bond pad, ultrasonic energy is simultaneously applied (c).

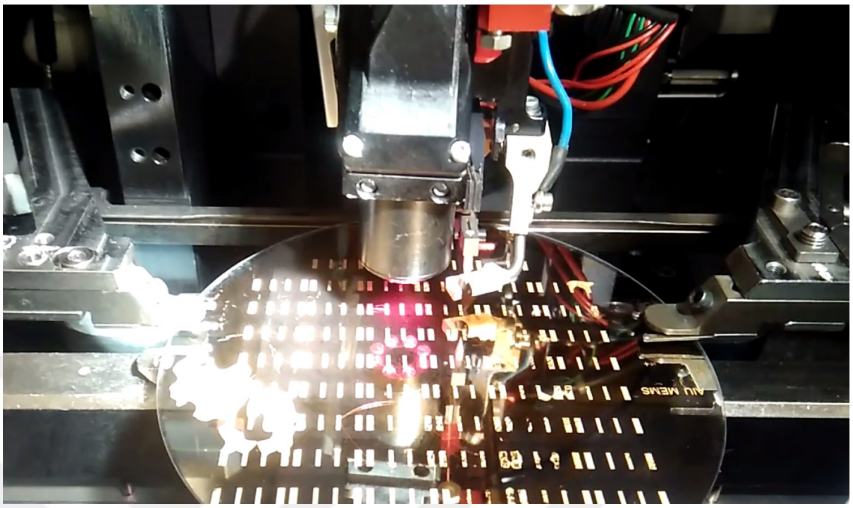

Figure A.1: A wafer under the wire bonder during process.

2- **Coil winding:**

- The capillary then rises and the wire is fed out by opening the clamp as shown in (d).
- The capillary moves by following the coil trajectory x, y and z coordinates provided to the bonding machine software.

3- **Wedge bonding:**

- The capillary is lowered again, deforming the wire against the final pad to shape a wedge (e).
- As the capillary rises, the clamp closes onto the wire, causing it to break immediately above the stitch bond (f).

As shown in figure A.3, the coil can be formed with a minimum of 3 points for a single winding, using more coordinates will result in a fine cylindrical shape but limits the maximum number of turns.

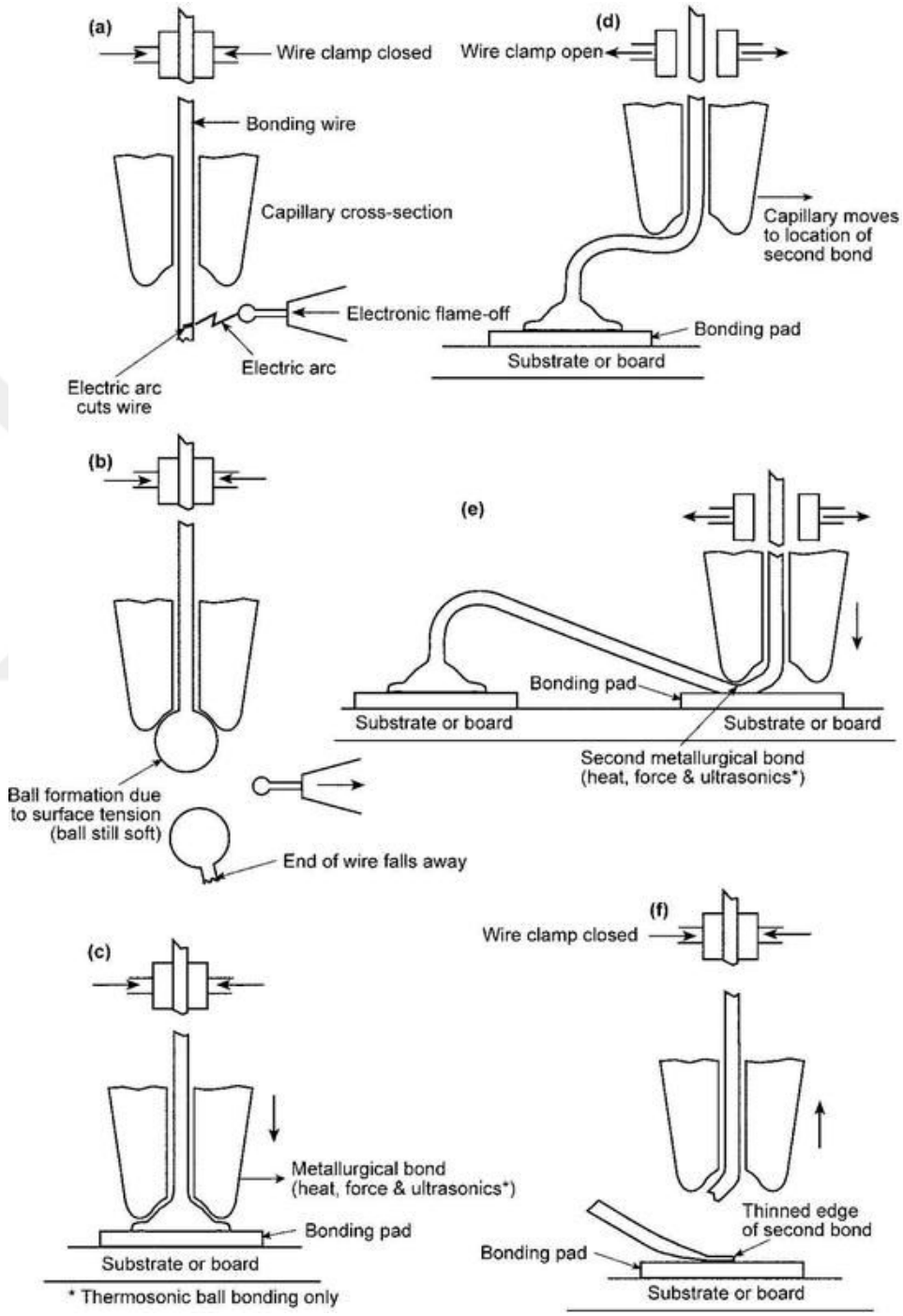

Figure A.2: Wire bonding process illustrating the three phases starting from ball bonding (a-c) then coil winding (d) and finishing with wedge bonding on the final pad (e-f).

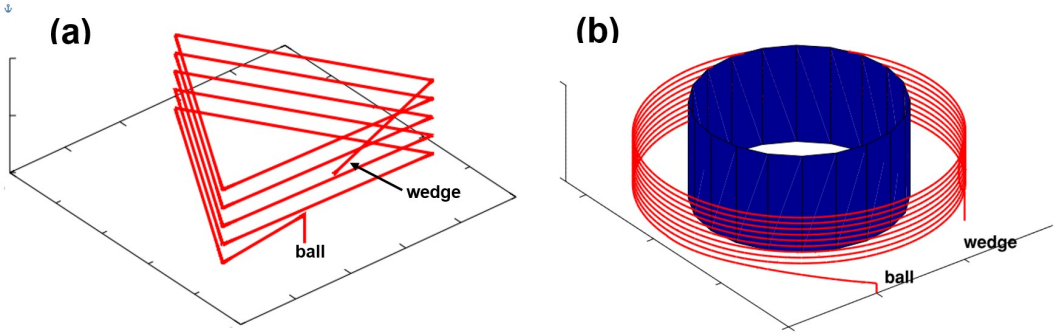

Figure A.3: Winding wire trajectory: (a) the resulting coil using minimum number of 3 points per turn and (b) a complete cylindrical coil generated using more points per turn.

Appendix B

Commercial Bio-implants and materials

B.1 Spinal Cord Stimulator

Spinal cord stimulation is a therapy that prevents pain signals from reaching the brain, it is implanted in the body to deliver electrical pulses to the spinal cord. It helps patients better manage their chronic pain symptoms and decrease the daily usage of medications.

Figure B.1: Spinal cord stimulation system specifications (from https://www.bostonscientific.com/content/dam/Manuals/us/current-rev-en/91057051-01RevA_Precision_Spectra_IPG_DFU_en-US_S.pdf).

B.2 Ventricular Assist Device

A ventricular assist device (VAD), also known as a mechanical circulatory support, they are mechanical pumps implanted to help circulating blood from the lower heart chambers (the ventricles) to the body, it is used in people who have weakened hearts or heart failure.

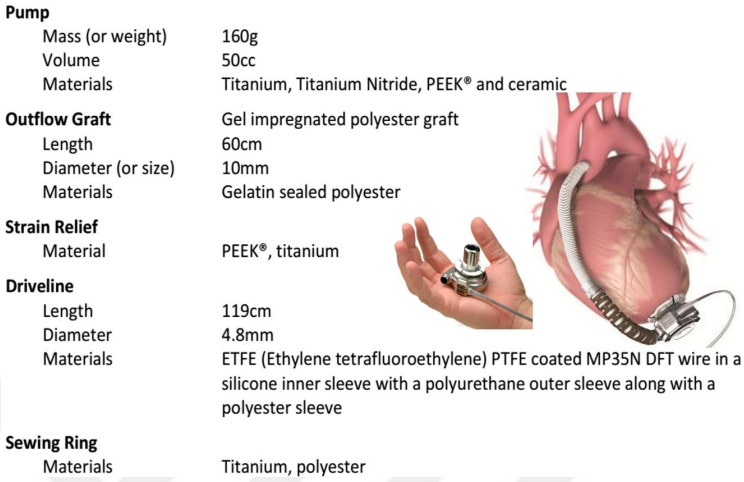

Figure B.2: HVAD® ventricular assist pump specifications

B.3 Pacemakers

A pacemaker is a small device that is placed in the chest or abdomen to help control abnormal heart rhythms. It uses electrical pulses to prompt the heart to beat at a normal rate. Pacemakers are used to treat arrhythmias, they are problems with the rate or rhythm of the heartbeat during which, the heart can beat too fast, too slow, or with an irregular rhythm.

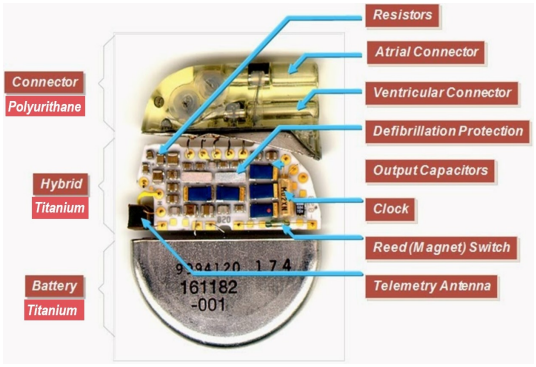

Figure B.3: Overview of pacemaker components, the packaging bio-material of each part is indicated on the left.

APEX Model DDD4000+:
-Dimensions: 47 X 55 X 8.5 mm
-Mass: 42 g
-Battery: Lithium-Iodine WG 8077
-Service life: 6 years and 10 months

TEROS SERIES / Model SSI R 603:
-Dimensions: 53 x 40.5 x 7.5 mm
-Mass:. 25.1 gr
-Battery: Lithium Iodine WG 8711
-Service life: 6.1 years

LD PACE II:
-Dimensions: 47 x 64 x 11.5 mm
-Mass: 53 g
-Battery: Lithium-Carbone Monofluoride WG9086
-Service life: 8 to 10 years

Figure B.4: Different pacemakers models with specifications (from http://www.ccc.com.uy/pacemaker/products.htm).

Appendix C

Micro-fabrication Recipes

C.1 Stator of DRIEed Si Substrate

This micro-fabrication was started by using 4" silicon wafer with 1.4 mm thickness covered with SiO_2.

1- **SiO_2 etching:**

- Lithography: AZ9260, wet etching using BOE (70-80 min)

2- **Si etching:**

- AZ9260 photoresist 15 µm
- Cleaning: Acetone 10 min, Isopropanol 5 min
- Spin coating: HMDS: 40 sec 4000 rpm 2000 rpm/sec, AZ9260: 3 sec 300 rpm 1000 rpm/sec, 80 sec 900 rpm 1500 rpm/sec
- Soft bake: 110 °C 8 min
- UV exposure: 1500 mJ/cm^2

- Developer: AZ400K Deionized water 1:4 8 min
- DRIE cycle: gases: SF_6 125 sccm, O_2 13 sccm, power: coil 600W, platen 20W, cycle time 10 sec
- Passivation cycle: gases: C_4F_8 80 sccm, power: Coil 600W, Platen 20W

3- **Gold deposition:**

- Thermal evaporation deposition: chromium 50 nm, gold 150 nm
- Gold etching: AZ5214 lithography, wet etching in diluted aqua regia ($3\,HCl$:$1\,HNO_3$:$2\,H_2O$) 20 sec
- Photolithography with IR5214 (1.4 m)
- Cleaning: Acetone 10 min Isopropanol 5 min
- Spin coating: AZ5214 40 sec 4000 rpm 2000 rpm/sec
- Soft bake: 110 °C 75 sec
- UV exposure: $30\,mJ/cm^2$
- Reversal bake: 120 °C 75 sec
- Flood exposure: $250\,mJ/cm^2$
- Developer: AZ726 MIF 40 sec

C.2 Stators on Pyrex Wafer

In this fabrication, the wafer was Pyrex glass with 500 µm thickness, coated with 10 nm and 50 nm layers of chromium and gold, respectively.

1- **Gold contact pads:**

- RIE: 10 min 400 mTorr 200 W
- Dehydration bake: 200°C 1 min, cool down

- Spin coat: SU-8 3025, Spin-Parameter: [s rpm/s rpm] 15 100 500 and 40 300 3000
- Soft bake: 13 min 95°C
- UV Exposure: Mask aligner Mask: Hacene: 370mJ/cm^2
- Post-exposure bake: @95°C for 3 minutes
- Development: 1. Old PGMEA 30min 2. New PGMEA 60 min 3. Isopropanol 30 min
- RIE Program: Standard descum 5 min. Oxygen plasma
- Electroplating: Area 6.2 cm, Thickness 5 m
- Stripping: duration 25 min, temperature 22 °C, power 1200 W
- Au etching
- Cr etching

2- **Columns and trenches structures:**

- Dehydration bake: 200°C 1 min
- Spin coating: 4 ml SU8, thickness 350m,
- Exposure
- Post bake exposure
- Coating 4.5 ml SU8, thickness 400µm, exposure, PEB and development

3- **Micro-coils wirebonding:**

- Partial dicing: 75%
- Wire type: Cu, thickness: 50µm
- Performed stators: [N:stators] 14:7 13:1 12:1 11:1 10:1

C.3 Stators on Silicon Wafer

In this fabrication, the wafer was made of silicon with 500 µm thickness, coated with 20 nm and 60 nm layers of chromium and gold, respectively.

1- **Gold contact pads:**

- RIE 10 min 400 mTorr 200 W
- Dehydration bake 200 °C 1 min Cool down
- BAR-Li II baking 1 min @ 200 °C, spin parameter [s rpm/s rpm] 10 100 500 and 30 300 3000
- Spin coat with SU-8 3025 [s rpm/s rpm] 15 100 500 and 40 300 3000
- Soft bake: 13 min @ 95 °C
- UV Exposure am Mask: Hacene: 400 mJ/cm^2
- Post exposure bake: 4 min @ 95 °C
- Development: Old PGMEA 30min, New PGMEA 60min, Isopropanol 30min
- RIE: 5 min
- Program: standard descum 5 min Oxygen plasma
- Electroplating: Area 6.2 cm, Thickness 5µm
- Stripping: duration 25 min, temperature 22 °C, power 1200 W
- Acetone+ ISO+ DI water cleaning
- Au etching
- Cr etching

2- **Columns and trenches structures:**

- Dehydration bake: 200 °C 1 min

- sacrificial layer (protection of pads) spin coat: AZ 4533 [s rpm/s rpm] 15 100 500 and 60 300 4000
- Softbake: 5 min @ 95 °C
- UV exposure mask: Hacenepads: 120 mJ/cm^2
- Development: AZ 726 MIF 60 s
- Dehydration bake: 120 °C 1min
- Spin coat: SU-8 3025 (Adhesion layer), [s rpm/s rpm] 15 100 500 and 40 300 3000
- Soft bake: 13 min @ 95 °C
- UV Exposure: mask Hacene pads, 400mJ/cm^2
- Post exposure bake: @ 95 °C 4 min
- Spin coat: 3.5 ml SU-8
- Soft bake 95 °C, Hotplate (2.5 h). Cool down to room temperature 4 h
- UV exposure: 800 mJ/cm^2 using 10 s gap between multiple exposures
- Post exposure bake: hotplate using special PEB cycle
- Spin coat: 4.5 ml SU-8
- Soft bake: 95°C, hotplate 3 h, cool down to room temperature in 4 h
- UV exposure 1500 mJcm^2 using 10 s gap between multiple exposures
- Post exposure bake: hotplate using special PEB cycle (over 8 h)
- Development of resist: PGMEA (fresh) 1h, rinse again in fresh PGMEA 15 min
- AZ resist removal: acetone 5 min
- Sentech oxygen plasma cleaning: 30 min

3- **Micro-coils wire bonding:**

- Partial dicing: 75%
- Wire type: Cu, thickness: 25 µm

- Performed stators: [N:stators] 13:20
- Coil protection layer: polyurethane